Pacific Northwest
NATIONAL LABORATORY

PNNL-34220

CO_2-Responsive Fracturing Fluids for Enhanced Geothermal Systems

June 2023

Guoqing Jian, Ramesh S. Sarathi, Jeff Burghardt, Susan Petty, Geoffrey Garrison, Varun Gupta, Tim Johnson, Lianjie Huang, Jian Liu, Trenton Cladouhos, Delphine Appriou, Paul Martin, Mark White, Leonard Pease, Chao Zeng, Zihao Li, and Carlos A. Fernandez

U.S. DEPARTMENT of ENERGY

Prepared for the U.S. Department of Energy
under Contract DE-AC05-76RL01830

DISCLAIMER

PACIFIC NORTHWEST NATIONAL LABORATORY
operated by
BATTELLE
for the
UNITED STATES DEPARTMENT OF ENERGY
under Contract DE-AC05-76RL01830

Printed in the United States of America

Available to DOE and DOE contractors from
the Office of Scientific and Technical Information,
P.O. Box 62, Oak Ridge, TN 37831-0062
www.osti.gov
ph: (865) 576-8401
fox: (865) 576-5728
email: reports@osti.gov

Available to the public from the National Technical Information Service
5301 Shawnee Rd., Alexandria, VA 22312
ph: (800) 553-NTIS (6847)
or (703) 605-6000
email: info@ntis.gov
Online ordering: http://www.ntis.gov

PNNL-34220

CO_2-Responsive Fracturing Fluids for Enhanced Geothermal Systems

June 2023

Guoqing Jian, Ramesh S. Sarathi, Jeff Burghardt, Susan Petty, Geoffrey Garrison, Varun Gupta, Tim Johnson, Lianjie Huang, Jian Liu, Trenton Cladouhos, Delphine Appriou, Paul Martin, Mark White, Leonard Pease, Chao Zeng, Zihao Li, and Carlos A. Fernandez

Prepared for
the U.S. Department of Energy
under Contract DE-AC05-76RL01830

Pacific Northwest National Laboratory
Richland, Washington 99354

CO_2-Responsive Fracturing Fluids for Enhanced Geothermal Systems

Final Report

03/23/2023

Guoqing Jian, Ramesh S. Sarathi, Jeff Burghardt, Susan Petty, Geoffrey Garrison, Varun Gupta, Tim Johnson, Lianjie Huang, Jian Liu, Trenton Cladouhos, Delphine Appriou, Paul Martin, Mark White, Leonard Pease, Chao Zeng, Zihao Li, and Carlos A. Fernandez

Pacific Northwest National Laboratory

Executive Summary

With funding from the DOE's Geothermal Technology Office, our group developed StimuFrac (US Patents 9,873,828 B2 and 9,447,315 B2), a non-toxic stimuli-responsive fracturing fluid consisting of a CO_2-reactive polymer. This polymer, polyallylamine (PAA) 17,000 Dalton, reacts with acid gases, like CO_2, in the presence of heat forming a crosslinking polymer that reversibly increase its volume and viscosity. The volume and viscosity can be reverted to its original values by pressure swing. StimuFrac/CO_2 demonstrated at the lab-scale to consistently fracture rock cores (2" long x ¾" diameter) at lower net pressures and significantly enhancing permeability as compared to water in Coso geothermal rock samples and in a range of representative geothermal pressure/temperature conditions.

The goal of project titled "CO_2-Responsive Fracturing Fluids for Enhanced Geothermal Systems" was to address the following key questions/technology barriers to mature PNNL's StimuFrac technology for field deployment:

1. What will be the best injection strategy for StimuFrac (aqueous polymer + CO_2) to propagate fractures beyond the mixing zone (hundreds of meters)?

2. What percentage of water reduction can be achieved?

3. How will StimuFrac perform in terms of permeability enhancement and fracture complexity compared to water and waterless fluids (e.g., CO_2) when going from cubic inch (previously studied) to cubic foot and to an actual field test?

4. Will StimuFrac generate fractures at lower applied pressures compared to water stimulation and waterless fluids (e.g. CO_2) when going from cubic inch (previously studied) to cubic foot and to an actual field test?

To address these technical questions, the project was divided in three phases. Phase I focused on a comprehensive understanding of StimuFrac fluid properties via experimental and modeling studies where the outcome will be information on viscosity, density, compressibility, and surface tension of the fluid as a function of fluid composition, pressure, and temperature. Phase II included stimulation experiments on foot-scale rock specimens as well as

numerical modeling of the injection processes. During this phase, we would focus on evaluating four injection strategies, adjusting injection parameters by considering fluid properties' dependence on P, T, composition (from Phase 1) in a foot-scale stimulation system. The best-performing injection strategy, in terms of permeability enhancement, extent and complexity of fracture network, will be adopted for field deployment (Phase III). Phase III would involve a field deployment of StimuFrac including a technoeconomic analysis that will be adjusted based on field test results.

The first part of the project began in FY19 and during **Phase I** we studied the mechanism/s responsible for the more effective fracturing, of critical importance to optimize fracturing performance as well as strategize injection methodologies for field deployment. We found that, in principle, two main mechanisms were responsible for fracturing rock at lower net pressures with this novel fracturing fluid. The first mechanism was demonstrated to be the additional work / overpressure generated by the aqueous polymer solution during its CO_2-triggered volume expansion. The second mechanism was reported to be associated to a reduction in pore invasion pressure as a result of the lower interfacial tension of StimuFrac and supercritical CO_2. This reduction in pore invasion pressure results in a reduction in fracturing net pressure. During Phase I it was also studied the density and molar volume of StimuFrac fluid as a function of geothermal relevant temperatures, CO_2 pressures, and weight fractions of StimuFrac added. In general, the results showed that StimuFrac's density decreases as temperature and pressure increase along the phase envelope. Using these results, equations of saturated state and phase diagrams for different polymer concentrations were reported which became critical inputs for numerical simulation efforts during Phase II.

The main goal of **Phase II** was to identify the best injection strategy for field deployment (Phase III of the project). This Team proposed four injection strategies which included (1) StimuFrac/CO_2 co-injection, (2) self-diversion, and (3) Polymer solution-alternating-gas (CO_2) or PAG, and (4) combinations of StimuFrac with Electrical Impulse Wave Propagation (technology under development at PNNL). The fourth stimulation strategy was removed from scope during budget negottiations.

During Phase II we designed and successfully built the world's first ½-ft cubic rock true triaxial frame for stimulation at high temperatures. Four fracturing fluids including water, CO_2, CO_2 with water, and CO_2 with aqueous PAA (StimuFrac) were used.

For all the water "only" fracturing tests, the conductivity of the rock fractured was quite low (less than 2 μm^3 based on radial flow assumption), regardless of the constant pump displacement rate or discrete pressure increments injection approach. For all three CO_2-based fracturing fluids, granite was fractured at higher breakdown pressures, higher transient pump displacement rates, and generated higher-conductivity fractures as compared to water. When partially saturating the rock sample with 1wt% PAA aqueous solution followed by fracturing with CO_2, the volume expansion and viscosity increase triggered by CO_2-induced cross-linking PAA led to a faster pressure increase than CO_2 in water saturated or initially dry. This faster pressurization rate is caused by a decrease in relative permeability of CO_2 in the presence of the high-viscosity cross-linked fluid compared to the un-crosslinked CO_2/water. It was also found that CO_2 as a fracturing fluid can generate high fracture conductivity only when injected at very high pump displacement rates in the presence of water or in hot dry rock (HDR). However, the conductivity of CO_2 fracturing in HDR was highly variable. CO_2 injected in the presence of 1wt% aqueous PAA generates fractures with the highest conductivity independently of injection pump displacement rates and using 1/6 of the mass of CO_2 as compared to CO_2 fracturing in HDR. The results of this study demonstrated CO_2/PAA as the best performing stimulation fluid under the studied geothermal P/T conditions. It was also concluded that CO_2/PAA offers the following three additional advantages over waterless CO_2, and CO_2/water fracturing fluids: i) it requires significantly lower volumes of CO_2 due to the reduced leak off; ii) large fractures can be generated reproducibly at both low and high CO_2 injection pump displacement rate, and iii) the reversible (previously reported) viscosity increase could be beneficial to transport proppants when they become available for EGS.

Among the injection strategies evaluated for deployment of StimuFrac, PAG was identified as a very promising deployment strategy showing consistenyl generating fractures with two or more orders of magnitude than water and other non-conventional (CO_2) in HDR as well as in 1-day and 3-day water

saturated granitic rock. However, water saturation plays a significant role in the performance of fracturing fluids, including StimuFrac. Nevertheless, StimuFrac was the only stimulation fluid to create a through fracture with moderate permeability in 200C granitic rock as compared to no fracture attained by the oher fluids. Self-diversion injection approach demonstrated to be a potential alternative to PAG but further studies are required to evauate this deployment approach.

The fact that, contrary to what is reported in the open litertature for low permeability rock, water saturation plays an important role in fracturing fluid performance, with higher water saturation resulting in lower fracturing efficiency independently of the fracturing fluid used was a new and very valuable discovery for the geothermal communicty. Therefore, GTO requested to perfom stimulation experiments in new ½-ft granitic rock samples under true triaxial stresses and 200C under fully water-saturated conditions. To PNNL's knowledge there is **no polyaxial loading frame in the world** larger than a few centimeters that can do hydraulic fracturing test while maintaining the rock sample fully saturated with water at 200 C.

PNNL proposed to GTO a (less studied) different StimuFrac formulation to perform hydraulic fracturing tests at temperatures below the boiling point of water, i.e., 90C. However, GTO established that these alternative StimuFrac formulations showed too low viscosity values to make them viable proxies for their use in replacement of PAA 17,000D (high-temperature formulation) for these studies.

In view of the above, PNNL suggests that there are only two ways to demonstrate StimuFrac/CO_2 as an alternative more efficient stimulation fluid in geothermal-representative water-saturated conditions:

1. Build the world first polyaxial frame with sample enclosure to maintain full water saturation at temperatures above boiling point of water, which costs about $2M
2. Perform a field test

Neither of these options are viable for GTO and, as a result, project was terminated.

PHASE I

Insights into a Greener Stimuli-Responsive Fracturing Fluid for Geothermal Energy Recovery

ABSTRACT

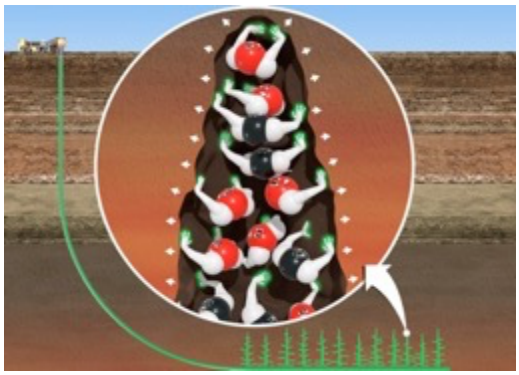

Our group has recently developed StimuFrac, a non-toxic stimuli-responsive fracturing fluid consisting of a CO_2-reactive polymer which has shown at the lab-scale to consistently fracture rock cores at significantly lower net pressures in a range of representative geothermal pressure/temperature conditions. However, until now the mechanism/s responsible for more effective fracturing, of critical importance to optimize fracturing performance as well as strategize injection methodologies for field deployment, was not understood. In this work, we report on the two main mechanisms responsible for fracturing rock at lower net pressures with this novel fracturing fluid. The first mechanism is the additional work / overpressure generated by the aqueous polymer solution during its CO_2-triggered volume expansion. The second mechanism is associated to a reduction in pore invasion pressure as a result of the lower interfacial tension of StimuFrac. This reduction in pore invasion pressure results in a reduction in fracturing net pressure as previously reported. The results presented in this work illustrate the potential of StimuFrac as a greener and less-energy intensive fracturing fluid for geothermal and fossil energy production.

INTRODUCTION

Among the other sources of renewable energy used to produce electricity, geothermal energy plays a special role with its ability to provide continuous baseload electricity. Most of the existing geothermal power plants are located in tectonic and volcanic active regions of the world where active hydrothermal fields are present. One of the primary challenges faced by EGS is to create safe and cost-effective high-permeability reservoirs in deep crystalline settings. The lack of suitable technologies to create cost-effective high-permeability reservoirs at the depths ranging from 900–4000 m and temperature in the range of 150 - 400°C is well recognized[1-3]. Recent advancements in the hydraulic fracturing techniques and horizontal drilling provide a critical driver for EGS and subsurface energy development, in general. The steady decline in the conventionally recoverable resources drove the implementation of hydraulic fracturing in over 52,000 oil and gas wells across the U.S.[2, 4, 5]. However, the fracturing fluids used in the oil and gas industry are problematic for EGS. The macro-polymers developed to modify fluid rheology in typical hydraulic fracturing are not applicable in high-temperature oil recovery (130-200 °C) and in EGS (150-400°C) due to their thermal decay.[6-8] An additional difficulty is the removal of such fluids from the formation after fracture creation[6-8]. This decreases flow rates and heat transfer. There are also significant concerns about the large volumes of water used and wastewater that requires treatment and disposal, and the potential contamination of soil and ground water.

We recently developed a new fracturing fluid that can mediate a stimulated volume expansion[9, 10]. This fracturing fluid [non-toxic poly(allylamine) aqueous solution (Molecular Weight=17,000 D), referred to as PAA hereafter] can undergo chemically–induced reactions with CO_2 to form a single-phase fluid/hydrogel with concomitant large and rapid volume expansion and viscosity increase (Figure 1)[9]. We postulated that this fracturing fluid, hereafter called StimuFrac^{TM}, can mediate a chemically-activated expansion in confined environments. This volume expansion could provide a controllable increase of hydraulic pressure to aid in fracturing processes. Indeed, high pressure/temperature laboratory-scale experiments that simulated reservoir stimulation conditions at different depths (different confining P and T) demonstrated fracture creation on actual EGS reservoir rock samples with the corresponding permeability enhancement [9, 10]. Furthermore, in most cases these fractures were generated at measured net pressure which was significantly lower than that required with conventional fracturing fluids under relevant EGS P/T conditions with the resulting potential reduction in pumping energy and cost. The volume expansion was demonstrated to be associated to a cross-linking reaction of PAA with CO_2, by means of chemical speciation studies using *in situ* High Temperature-High Pressure ^{13}C Magic Angle Spinning Nuclear Magnetic Resonance Spectroscopy (MAS-NMR)[9].

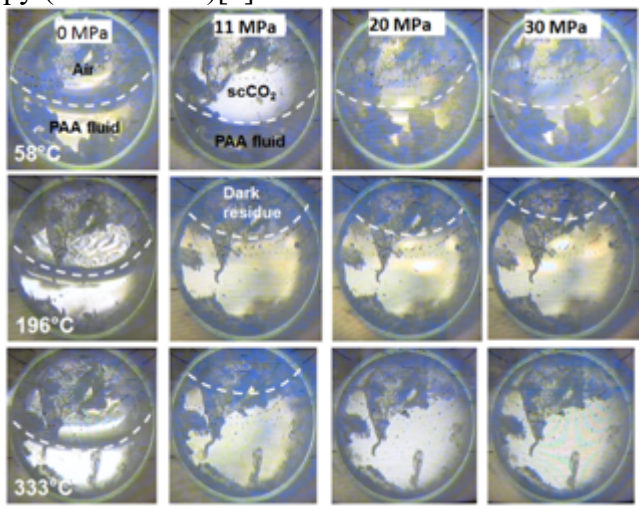

Figure 1. Volume changes of PAA solution reacted with CO_2 as a function of temperature (58–333°C) and CO_2 pressure (0–30MPa). CO_2 pressure was increased from 0 to 30MPa. The dashed lines indicate the boundary between PAA fluid and supercritical CO_2 (after CO_2 injection) or air/water vapor (before CO_2 injection). No volume expansion was observed in the same temperature range for deionized water (DIW) /CO_2 [9].

In this work, we evaluate StimuFrac's fracturing performance on highly impermeable surrogate samples and postulate a mechanism for which StimuFrac consistently generates fractures at significantly lower net pressures as compared to conventional (hydraulic) fluids and waterless fluids. Three main potential driving mechanisms are postulated as follows: 1) Reduction in specimen's fracture toughness due to low pH associated with the dissolution of CO_2 in the aqueous PAA solution forming carbonic acid; 2) overpressure associated to the volume expansion as a result of the reaction between aqueous PAA (StimuFrac) and CO_2; and 3) lower pore invasion pressure directly related to the interfacial tension of the fracturing fluid.[11, 12] A series of experiments were performed to down-select the main responsible driving mechanism/s including A) lab-scale stimulation with different fracturing fluids using fused silica, a homogeneous surrogate material with known, rock-like mechanical properties and on rock samples obtained from Coso EGS site in California, USA; B) a state-of-the art constant-volume mixing cell was designed, fabricated and used to carry out overpressure measurements due to the chemical expansion of StimuFrac in the presence of CO_2; C)

permeability measurements as a way to compare relative dynamic interfacial tension in porous media. In this manner, we provide a quantitative basis for the potential application of this greener (non-toxic) stimuli-responsive fracturing fluid for EGS-based energy exploitation.

MATERIALS AND METHODS

Chemicals and surrogate samples

PAA was obtained from Sigma Aldrich. This polymer solution was diluted with deionized water (DIW) 20 times and the diluted solution was used for hydraulic fracturing experiments as described below.

Fused silica was chosen as the surrogate material for fracturing experiments due to its homogeneity and rock-like properties. Transparent fused silica rods 16 mm diameter x 50.8 mm long with a 3.2 mm diameter x 25.4 mm deep bore on one end were obtained from Technical Glass Products, Inc. In addition, nine cylindrical Coso igneous rock samples with the same dimensions were extracted from a single core [diorite, moderately foliated, 1623 feet true vertical depth (TVD), reservoir Coso CGC 18-27]. The top and bottom of all cylinders were polished to ensure no fluid leakage and proper sealing with a mechanical O-ring (see next section).

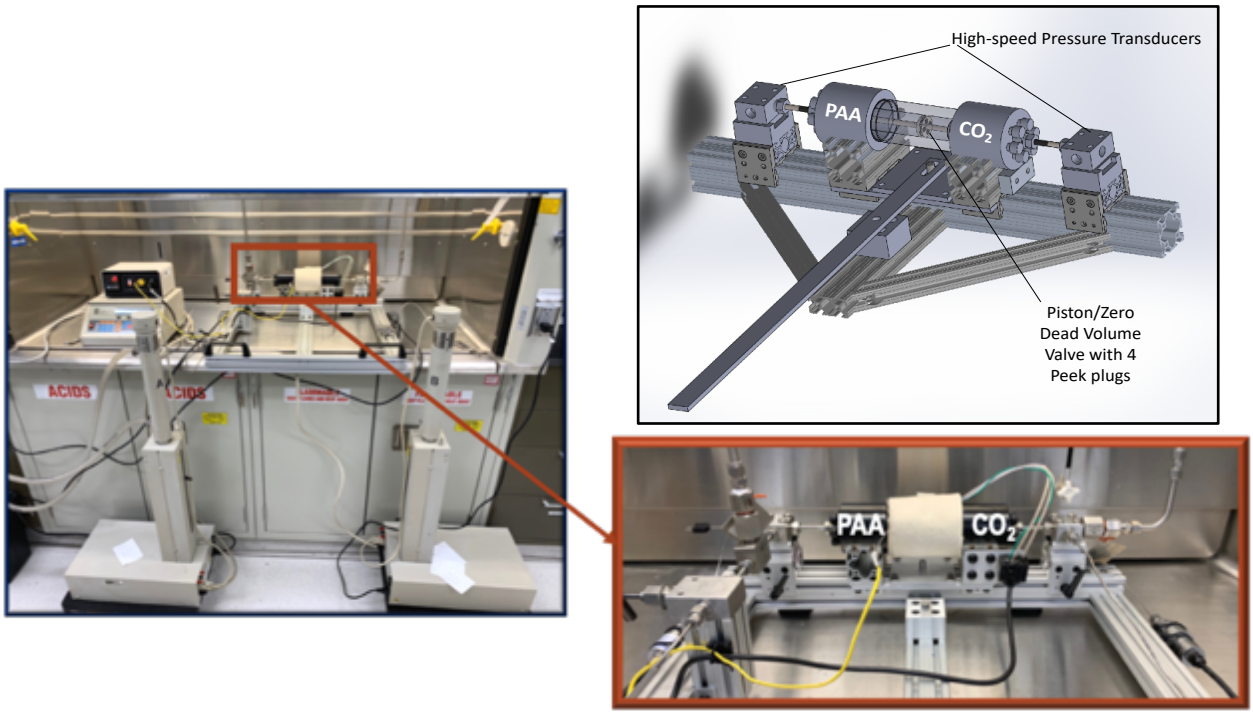

Figure 2. State-of-the-art constant volume high-pressure/high-temperature mixing vessel showing the mixer/constant volume valve consisting of four Peek plugs sitting on a piston. Movement of the piston in the direction of the more compressible fluid (CO_2) causes the plugs to fall out, allowing for a rapid mixing between the polymer solution and CO_2.

Volume expansion associated overpressure determination

Design and construction of high-pressure and high-temperature vessel with constant volume

A custom-made constant volume mixing vessel was designed and fabricated in-house. The vessel consists of a 46-mL flow reactor and a rod with dynamic sealing by bal seals® (Figure 2). The rod has a center piston with four holes covered by Peek plugs. These plugs are seated on one side of the piston and the piston separates the two sides of the reactor. In this fashion, two different fluids can be

injected on each side of the vessel and can stay completely separated from each other. The mixing rod is fixed, but the flow reactor is not. The reactor can be displaced in either direction increasing the volume on one side of the reactor and simultaneously decreasing the volume on the other side. The direction of displacement of the reactor will control the mixing. When the reactor moves in the direction opposite to the side where the Teflon plugs are sitting in the piston, the plugs will fall down, and communication followed by mixing of the two fluids will occur. Two high-speed (1 KHz) pressure transducers are located on each side of the reactor cell. The cell is heated by heating tape and the temperature is monitored using a thermocouple inside the vessel (Watlow Electric Manufacturing Company; max. temperature: 1700 °C, accuracy: ±2 °C), connected to a thermocouple controller (Parr Instrument Co., Parr 4843; operating range: 0–800 °C, accuracy: ±2 °C). Pressure and temperature data are logged using software LabView version 16.0. Pressure of each fluid (CO_2 and aqueous PAA or water) is controlled with ISCO pumps. The vessel is thermally insulated, so the experiment takes place at constant temperature as well as constant volume.

Determination of pressure associated to volume expansion

The following procedure was devised to perform the experiments. First, using an ISCO pump the vessel is filled with 39 mL of water (control experiment) or an aqueous solution of PAA on the side of the piston where the Teflon plugs are sitting on top of it. In this fashion, the highly incompressible water pushes the plugs against the piston maintaining them in place. This is followed by closing the valve communicating the pump with the vessel and heating up the vessel to the target temperature, 200 °C. The pressure of the vessel is approximately equal to the vapor pressure of water, 2.28 MPa. Then, the other side of the vessel is filled with CO_2 at 6.20 MPa using a second ISCO pump and letting the vessel pressure to equilibrate. Once pressure in the vessel is constant (~ 6.20 MPa on both sides), the mixing begins by moving the vessel along the fixed rod in the direction of the CO_2 side to cause the Teflon plugs seated on the piston to fall down. This step is followed by injection of CO_2 at a low and constant flow rate of 0.5 mL/min. Pressure on both sides is monitored with the pressure transducers located on both sides of the vessel. Temperature inside the vessel is monitored with a thermocouple. Pressure and temperature are monitored and recorded during the entire experiment until the reactor reaches the maximum operating pressure, 20.68 MPa. This procedure was followed to carry out six experiments, which included triplicate control experiments (water and CO_2) and triplicate experiments with aqueous PAA and CO_2.

Lab-scale stimulation experiments

Laboratory-scale fracturing experiments were performed using fused silica and Coso rock cylindrical samples. A schematic diagram for the hydraulic fracturing experimental setup was provided previously (Figure 3 and [9]). Each sample was placed in a state-of-the-art cradle designed to expose the entire sample to the desired confining pressure while isolating the central bore, drilled to introduce the fracturing fluid[9].

Stainless steel tubing (1.6 mm OD) was introduced 5 mm into the hole leaving an internal dead volume of ~200 µL in the rock core. A mechanical O-ring made of graphite was used on the top of the cradle to ensure sealing of the connections and avoid any communication between the external fluid (water is used to apply the desired confining pressure) and the internal dead volume in the cylinder during the course of the fracturing experiment. The internal central bore in the cylinder inside the cradle was then connected to the head of a high-pressure vessel (High Pressure Equipment Company, Erie, PA), and the cradle was introduced to the pressure vessel. A 3-way valve was used to deliver polymer solution and CO_2. The temperature of the reactor was controlled with a heating tape, a thermocouple, and a temperature controller. After the target temperature was reached, water was injected into the pressure vessel using a syringe pump to increase the confining pressure.

The confining pressure was first increased to 7 MPa, immediately followed by introduction of 200 µL of 1 wt% PAA solution and 7 MPa of CO_2 inside the core sample via the three-way valve. Thereafter, the confining pressure and pressure inside the cylinder were increased in 0.7 MPa intervals until the target confining pressure was achieved. At this point, the confining pressure was held constant and subsequently, the cylinder internal pressure was gradually increased in the intervals of 0.7 MPa by injecting the fracturing fluid. This was continued until a sudden increase in the confining pressure was observed. This pressure equilibration indicates communication between the internal (fracturing) and external (confining) fluids as a result of fracture formation. The pressure difference between the pressure reading inside the sample at the instant right before the sudden jump and the confining pressure at the same instant is defined as the *net pressure* required for fracturing the cylindrical sample. After pressure equilibration was observed, the system was cooled down to room temperature and the pressure was released followed by opening the flow reactor and retrieving the cylindrical sample.

For the fused silica samples, the following fracturing fluids were evaluated; StimuFrac/CO_2, water/CO_2 (fluid composition identical to the composition of the StimuFrac/CO_2 fluid but without PAA in the aqueous phase), water, CO_2, and hydrochloric acid 1 mM (pH=3). Due to the limited number of samples that can be generated from a single rock core, only StimuFrac/CO_2 fluid and water/CO_2 in the absence of PAA were evaluated with the Coso rock core. Besides determining the net (fracturing) pressure, the cylindrical rock samples obtained from a single rock core were subjected to permeability tests.

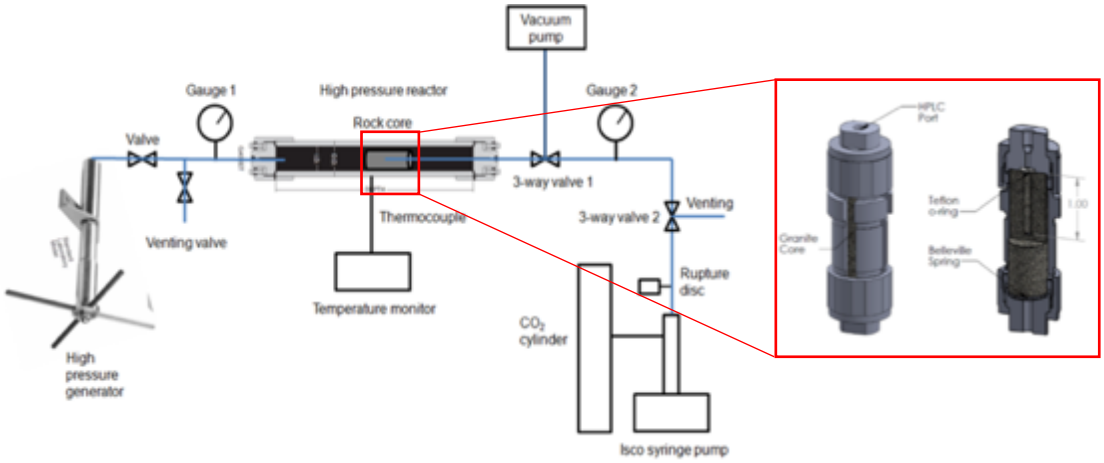

Figure 3. Schematic diagram for the lab-scale stimulation experimental setup. Cradle to hold and insulate the volume of the bore hole from the confining volume is shown on the right[10].

Fracturing pressure prediction for fused silica specimens: Computational Modeling

In order to have a predictive and quantitative understanding of the hydraulic fracture in fused silica samples, a computational model was developed using the finite element method. The geometry and dimensions of the cylindrical sample used in the model are shown in Figure 4(a). Due to the symmetry of geometrical configuration and loading conditions, a simplified 2-D axisymmetric model could be used, as illustrated in Figure 4(b). The confining pressure is denoted as P_{ext}, whereas the applied fluid pressure is assumed static and referred to as P_{int}. A uniform distribution of the two pressures is assumed in the model. Fixed displacement boundary conditions were used at the bottom face of the cylindrical model. Fused silica was treated as a homogeneous and isotropic material. A linear elastic material behavior was assumed for the fused silica with the following typical material

properties [13] at the room temperature: Young's modulus = 74 GPa, Poisson's ratio = 0.17 and Fracture toughness = 0.70 MPa $m^{1/2}$. Thermo-mechanical effects were not considered to keep the model simple.

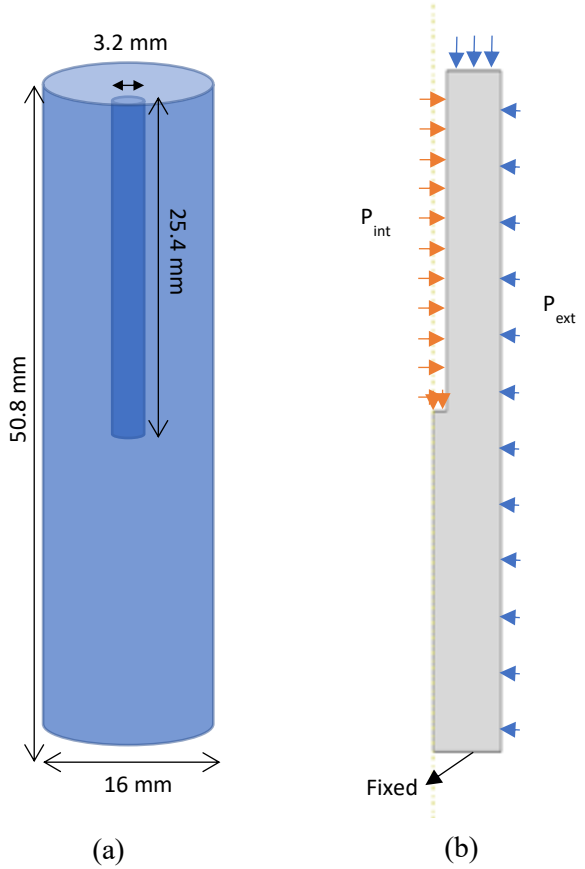

Figure 4. (a) Geometry and dimensions of the cylindrical sample. (b) Axisymmetric model and applied boundary conditions. Blue arrows represent the confining pressure, whereas the red arrows indicate the applied fluid pressure.

The end of the central bore has sharp edge, which leads to the stress concentration. Therefore, a much finer mesh is needed near that edge to accurately capture the stress singularity. A carefully constructed finite element mesh with localized refinement near the sharp corner at the end of central bore was used. (Refer to Figure S1). Quadrilateral elements were used with quadratic approximation properties for higher accuracy. Figure 5 shows the properly captured maximum in-plane stress distribution near the corner at the end of central bore.

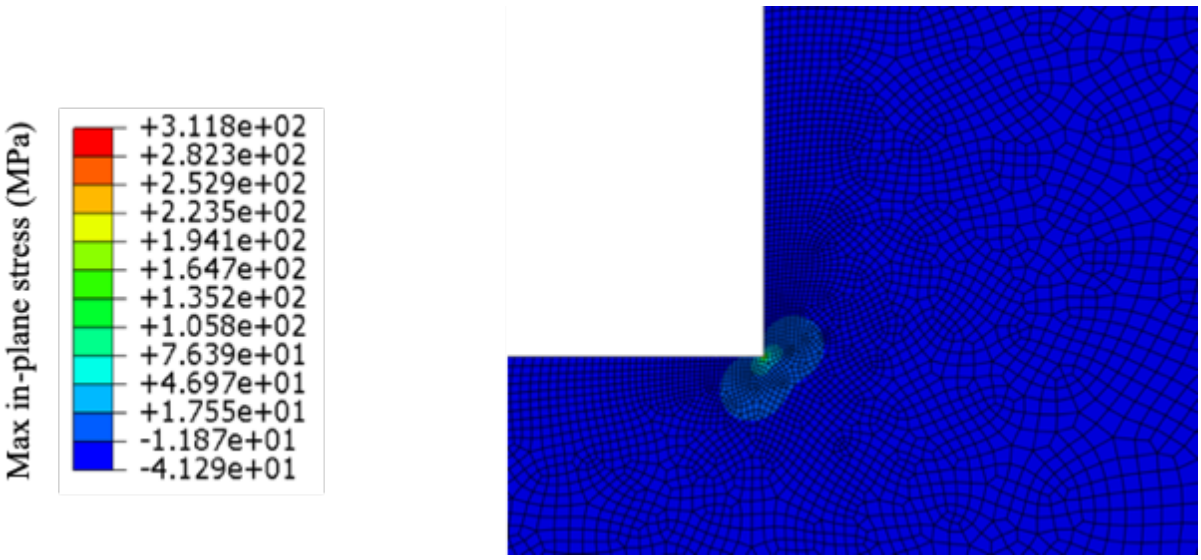

Figure 5. Horizontal cross-section showing the contour plot for maximum in-plane stress (in psi) near the sharp corner of cylindrical specimen.

Permeability measurements

Permeability tests were performed on a stainless-steel column (1/4" diameter by 15 inches length) packed with silica fume (200 Mesh). Permeability was tested using the saturated constant head method[14] where constant head pressure was maintained by keeping the reservoir (sealed column) at a constant pressure (0.07 MPa) and the discharge was measured at atmospheric pressure. Darcy's law for flow through silica fume was employed as follow:

$$Q = -\frac{kA}{\mu}\left(\frac{P_b - P_a}{L}\right) \quad (1)$$

Where:
Q = discharge ($cm^3\ s^{-1}$); k = permeability of porous medium (m^2); A = cross-sectional area to flow (m^2); μ = dynamic viscosity (Pa·s); P_b = pressure from pump (Pa); Pa = pressure from atmosphere (Pa); L = length (cm).

X-ray microtomography (XMT) analysis

XMT scanning was performed at 110 keV and 190 μA for optimum image quality and contrast. The samples were rotated continuously during the scans with momentary stops to collect each projection (shuttling mode) and minimize ring artifacts. A total of 3142 projections were collected over 360◦ with 0.5 s exposure time and 4 frames per projection. The images (obtained with voxel sizes between 25 to 30 μm) were reconstructed to obtain three-dimensional datasets using CT Pro 3D (Metris XT 2.2, Nikon Metrology, UK). For rock cores after fracturing experiment, pressurized scans were conducted using a cell containing the sample connected to a nitrogen tank regulated to 0.8 MPa (similar to pressure gradient of permeability measurements). The cell was made of polyether ether ketone (PEEK) to minimize the adsorption of X-ray.

RESULTS AND DISCUSSIONS

Computational prediction for failure of fused silica samples

The resistance to fracture in brittle materials is measured in terms of the fracture toughness. In the fused silica cylindrical sample, the sharp edge at the end of central bore causes stress concentration. Therefore, a crack will initiate and propagate if the stress intensity factor (SIF) [15] at that edge exceeds the fracture toughness. The SIF is directly proportional to the square root of another physical quantity known as the energy release rate [15]. The energy release rate for different assumed crack extension direction at the sharp edge are plotted in Figure S2. The maximum value of energy release rate is obtained at an angle $\theta = 45°$, which indicates the predicted direction of crack extension once it is initiated. For isotropic, linear elastic materials, the energy release rate is related to the stress intensity factor (SIF) as follows:

$$\Gamma = K_I^2 \left(\frac{1 - \nu^2}{E} \right) \quad (2)$$

where, Γ is the energy release rate, K_I is the Mode I stress intensity factor, E is the modulus of Elasticity and ν is the Poisson's ratio. The SIF is calculated based on Equation (2), using the maximum value of energy release rate that is obtained at an angle of $\theta = 45°$.

A confining pressure of P_{ext} = 34.45 MPa is assumed. The plot of SIF values against different magnitudes of internal pressure is provided in Figure 6. The internal pressure magnitude of 58.61 MPa, corresponding to a SIF value of 0.7 MPa $m^{0.5}$ (fracture toughness of fused silica) indicates the threshold internal fluid pressure required for fracture. Therefore, the computationally predicted *net pressure* (P_{ext} - P_{int}) was found to be 24.13 MPa. The confining pressure does not have a significant effect on the net static pressure required to create a fracture (illustrated by plot in Figure S3).

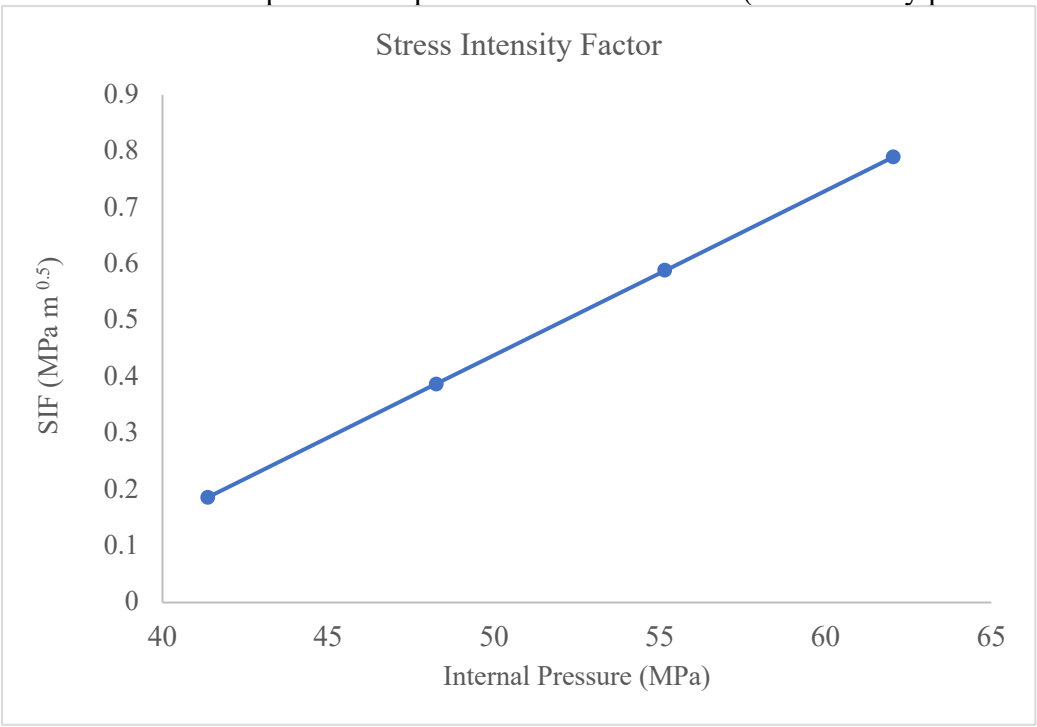

Figure 6. Stress intensity factor values for different applied fluid internal pressure.

Lab-scale stimulation results

Non-porous fused silica specimens

This section provides the results of the lab-scale stimulation experiments performed on the fused silica samples employing different fracturing fluids. These fracturing fluids were StimuFrac/CO_2 (also labeled as PAA/CO_2), water/CO_2 (fluid composition identical to the composition of the PAA/CO_2 fluid but without PAA in the aqueous phase), pure water, pure CO_2, and a solution of hydrochloric acid 1 mM (pH=3). Figure 7 illustrates a hydraulically fractured fused silica sample, which clearly shows the conical fracture plane at an angle of approximately 45°. Four to five fused silica specimens were fractured with each fracturing fluid. Figure 7 shows a typical plot of confining pressure and fracturing fluid pressure as a function of time. The plot shows that fracturing fluid pressure is increased in discrete and controlled intervals of 0.7 MPa every 20 seconds while the confining pressure is kept constant at 20.7 MPa. When the fracturing of the fused silica specimen occurs, the confining fluid pressure suddenly increases while the fracturing fluid pressures simultaneously decreases and both pressures reach a similar equilibrium value. The net pressure required to fracture the individual fused quartz specimens was calculated by the pressure difference between the pressure reading inside the specimen at the instant right before the change in pressure and the confining pressure at that same instant (Figure 7).

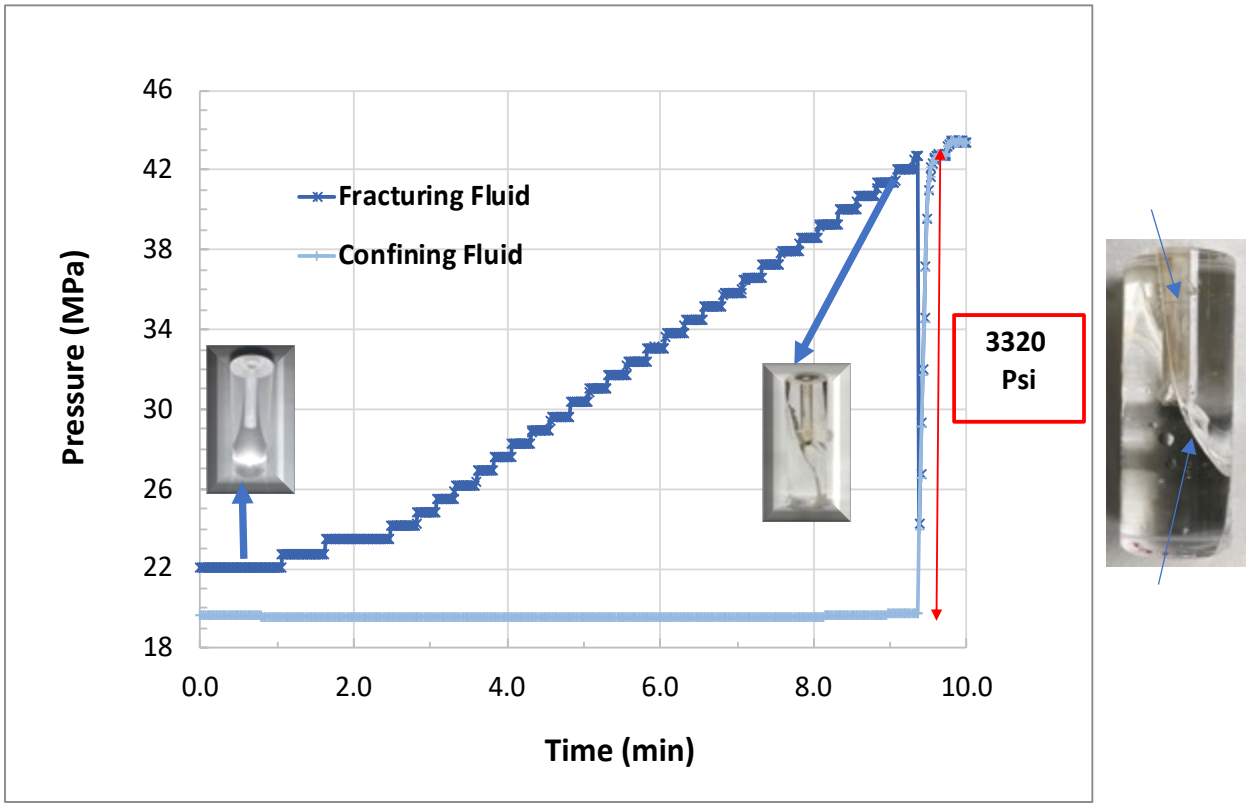

Figure 7. Left. Plot of fracturing pressure and confining pressure as a function of experiment time showing the net pressure required to fracture one of the fused silica specimens. Right. Fractured fused silica cylindrical specimen.

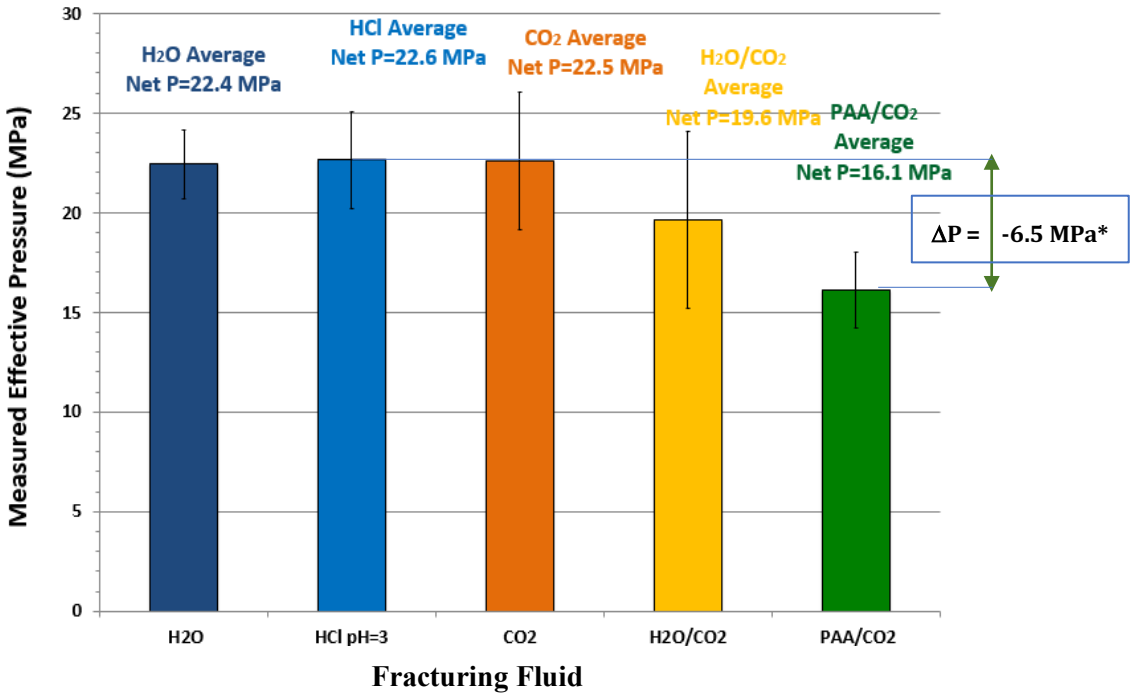

Figure 8. A. Average net pressures required for fracturing fused silica specimens employing different fracturing fluids as indicated in the chart. Minimum four specimens were fractured with each fracturing fluid. Different colored bars represent different fracturing fluids.

As the individual tests showed some variance in the measured net pressure for each fracturing fluid, their average value is obtained and plotted in Figure 8. Figure 8 shows that the net pressures required to fracture fused silica specimens with single phase fluids water (22.4 ± 1.7 MPa) and CO_2 (22.6 ± 3.5 MPa) are statistically similar and close to the predicted net pressure by computational modeling (24.1 MPa). The slight discrepancy in the values might be because of the variance in the material properties of fused silica, which were taken from the literature. When employing a binary fluid such as water/CO_2 we observed that the average net pressure required to fracture these specimens (19.6 ± 4.4 MPa) was lower, though the data variability is the largest of all the fluids evaluated. A student t-test shows that fracturing with a water/CO_2 mixture or fracturing with pure water or pure CO_2 fluids require statistically similar net pressures with 95% confidence. Nevertheless, the combination of water and CO_2 may still play a role in reducing net pressure and could also be associated to one of the mechanisms discussed in the following sections. PAA/CO_2 fracturing fluid showed fracturing net pressures for fused silica of 16.1 ± 1.9 MPa with a low sample variability. A Student's t test showed that this value is statistically different, with a 95% confidence level, to the rest of net pressure values obtained with other fracturing fluids, including water/CO_2. The average measured net pressure required for fracturing obtained with PAA/CO_2 is ~ 30 % (6.5 MPa) lower compared to water.

It can be clearly seen from these results that amongst the five fracturing fluids, PAA/CO_2 required the least measured fluid pressure for fracturing non-porous fused silica. It is to be recalled that the computationally predicted value of 24.1 MPa was obtained for the case when there is uniform and static pressure distribution at the inner surface of the central bore. This seems not to be necessarily true, especially for fluid mixture like PAA/CO_2. Therefore, based on these results, it is hypothesized that the fluid mixture PAA/CO_2 could lead to a non-uniform distribution of pressure along the length

of central bore and/or an overpressure associated to the CO_2-triggered volume expansion of aqueous PAA.

Coso rock samples from a single core

This section details the results from the hydraulic fracturing experiments performed on igneous Coso rock cylindrical specimens. These specimens were collected at a depth of 495 m in well 18-27 Northeast of the central part of the Coso geothermal field in California. Rock samples consisted of Mesozoic diorite metamorphosed to greenschist facies. Their mechanical properties have not been determined but they can be compared to those of similar rock formation obtained at two nearby wells located 4-5 km to the southwest. Well 34-9 diorite has a Poisson's ratio of 0.311 and a Young's modulus of 105.1 and well 38C-9 hornblende-biotite quartz diorite (HBQD) has an unconfined compressive strength C0 of 189 MPa[16, 17].

Coso samples surface area and average pore size was determined to be ~1.1m^2/g, and 1.8nm using nitrogen isotherms at 77K and the Barrett-Joyner-Halenda method for pore size analysis. It is important to mention that this data was obtained from mixing multiple pieces from different fragments of the single core and may not represent the actual micropore structure. Given the fact that only nine samples can be fabricated from a single core, only two fracturing fluids, both mixtures, were considered- PAA/CO_2 and H_2O/CO_2 to further compare the performance of binary fluids and if PAA does indeed aid to a reduction in fracturing net pressure. The results for net pressure required for fracturing are provided in Figure 9. The average net pressure obtained for H_2O/CO_2 is 4.0 ± 0.3 MPa from five different specimens, whereas a 25 % lower average value of 3.0 ± 1 MPa is obtained from four different specimens fractured with PAA/CO_2. Permeability values for rock samples fractured with H_2O/CO_2 fluid ranged from 4.93 x 10^{-16} m² to 1.38 x 10^{-14} (0.5 mD to 14 mD). Similarly, permeability values obtained when fracturing with PAA/CO_2 varied between 9.87 x 10^{-16} to 1.68 x 10^{-14} (1 mD and 17 mD). Note: one of the five specimens subjected to stimulation with the control fluid H_2O/CO_2 fractured at a vein location that extended across the length of the sample partially contacting the wall of the center hole. The post-fracture permeability for this particular sample was 1,060mD, which also provided the lowest measured overpressure, 3.6 MPa (first data point from left to right in Figure 9).

An interesting aspect to be noted from the results in Figure 9 is that the variance in the measured net pressures for PAA/CO_2 is now much larger compared to the H_2O/CO_2. Such net pressure data variance makes the two average net pressure statistically similar based on a student's t-test. The opposite was observed when fracturing non-porous fused silica specimens. Since the Coso rock samples are expected to be microscopically heterogeneous with the presence of unevenly spread microscopic pores, the larger variability in net pressure from sample to sample when fracturing with PAA/CO_2 seems to indicate a difference in the pore-scale pressure generation behavior of this fluid as compared to H_2O/CO_2. In other words, the large variations in net pressure for PAA/CO_2 could be directly associated to the performance response of this fluid to the microscopic heterogeneity and porosity; while H_2O/CO_2 performs in a similar fashion independently of the rock microstructure. It has been previously reported that fluids with lower pore invasion pressure fracture at lower net pressures[11, 12]. Fluid's pore invasion pressures are directly associated to interfacial tension and viscosity properties of the fluid with lower pore invasion pressures attained by fluids with lower interfacial tension and/or viscosity.[11, 12] The difference in viscosity and surface tension of the water/CO_2 and PAA/CO_2 fluids could then be responsible for their fracturing effectiveness. Evaluation and proper understanding of this behavior is discussed later.

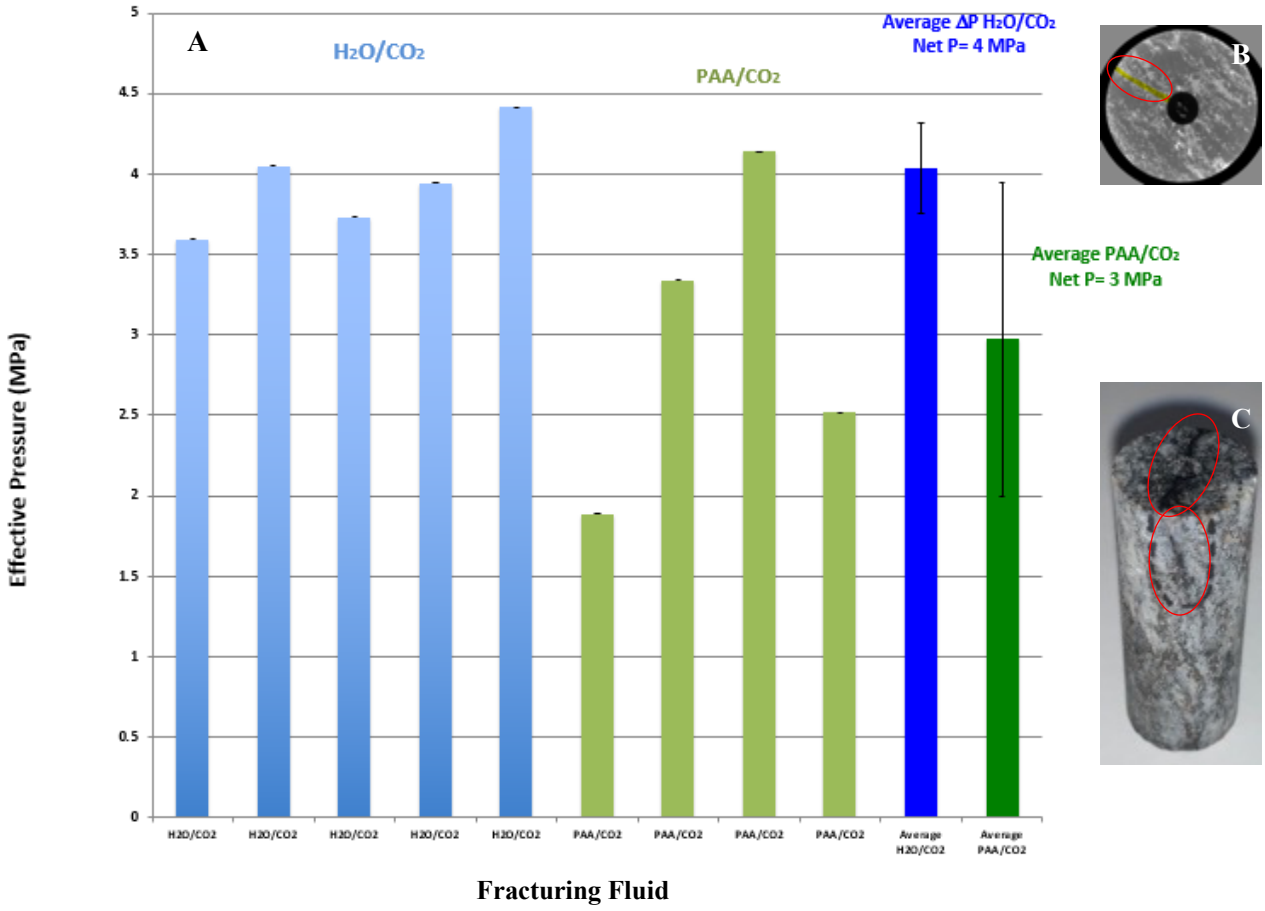

Figure 9. A. Net pressures required for fracturing measured on Coso specimens (samples obtained at 1623 feet TVD, reservoir Coso CGC 18-27). Different colored bars indicate net pressure measured in case of corresponding different fracturing fluid as indicated in the chart. **B**. Representative transversal micrograph obtained by X-ray tomography of a Coso rock sample after fracturing. **C**. Representative picture of a Coso sample after fracturing showing a typical longitudinal fracture plane nearly parallel to the wellbore direction.

As stated in the Introduction section, we propose that three main driving mechanisms could be responsible for the lower net pressures measured in the previous section. These are 1) reduction in specimen's fracture toughness due to low pH associated to the dissolution of CO_2 in the aqueous PAA solution forming carbonic acid; 2) non-uniform pressure distribution and/or overpressure associated to the volume expansion as a result of the reaction between aqueous PAA (StimuFrac) and CO_2; and 3) lower pore invasion pressure directly related to the interfacial tension and viscosity of the fracturing fluid. In the following sections we evaluate each of these proposed mechanisms.

Role of pH in net fracturing pressure

It has been reported that severe environments, such as acidic or alkaline conditions, can cause reduction in fracture toughness of materials.[18, 19] To investigate if the reduction in pH by CO_2 dissolution in aqueous PAA plays a role in reducing the fracturing net pressure as a consequence of a

reduction in fracture toughness, additional lab-scale stimulation experiments were performed on fused silica specimens. In this case, we used as fracturing fluid a mineral acid with a pH value similar to the pH of aqueous solutions of CO_2 at the pressure and temperature conditions of the experiments. This pH value was estimated to be 3.5.[20] Therefore, the fracturing fluid used for the lab-scale stimulation experiments was a pH=3 solution of hydrochloric acid. Four stimulation experiments on fused silica specimens were performed with this acid solution and the results are shown in Figure 8. The average net pressure (22.6 MPa) required to fracture fused silica with this mineral acid was statistically similar to the net pressures required to fracture similar fused silica specimens with pure water (22.4 MPa). Given the short period of time these experiments take, in one of the experiments we introduced the solution of mineral acid in the fused silica bore hole and kept at high pressure and temperature (20.7 MPa, 200 °C) for 24 hours. The net pressure value for this, significantly, longer experiment was above the average (22.6 MPa), demonstrating that, under the pressure and temperature conditions of this work, the pH does not play a role in lowering the net pressure required to fracture these samples.

Role of overpressure associated to CO_2-induced StimuFrac's volume expansion

The reaction between PAA with CO_2 responsible for the volume expansion is shown in Scheme 1. Briefly, the reaction consists of a Lewis acid-base reaction between acid gas (CO_2) and the amine functionality in the PAA forming ammonium carbamate and followed by dehydration to a urea linkage.[9] This crosslinking reaction extends in all three dimensions forming a 3D expanding fluid.

Scheme 1. Crosslinking reaction between PAA and CO_2 forming a three-dimensional fluid filled

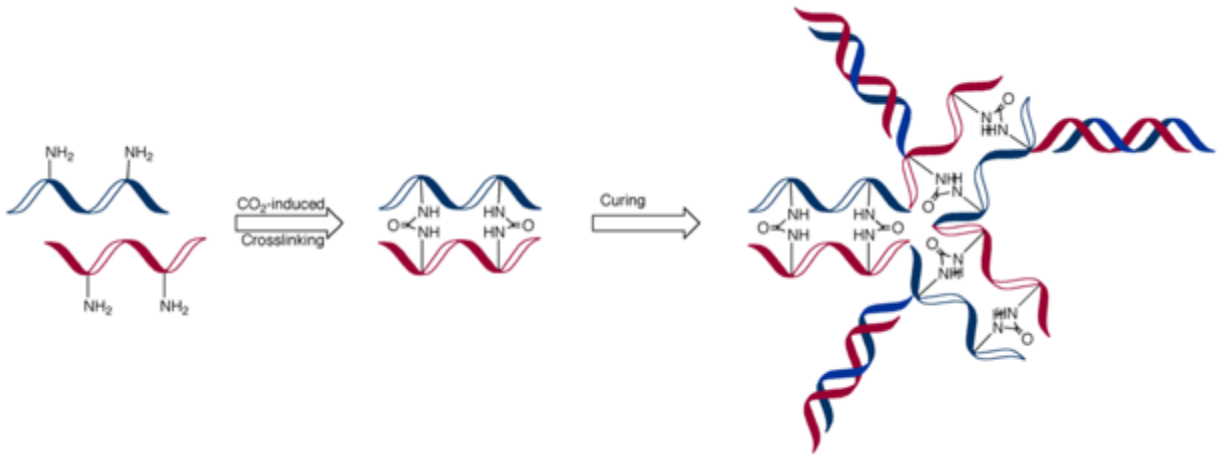

network.

As described in section 2.2 a constant volume high pressure/temperature vessel was designed and used to determine overpressures associated to the volume expansion product of the reaction of aqueous PAA with CO_2. Experiments were performed by triplicate and included control experiments were water and CO_2 in the absence of the polymer were also mixed under identical conditions. The pressure/temperature conditions previous to mixing were 200 °C/ 2.3 – 20.7 MPa for water/CO_2 and PAA/CO_2. As described earlier, CO_2 was introduced at room temperature as follow. First, CO_2 at constant pressure (6.2 MPa) was injected using a second Isco pump and letting the vessel pressure to equilibrate. Once pressure in the vessel is constant (6.2 MPa on both sides), the mixing begins by moving the vessel along the fixed rod in the direction of the CO_2 side to cause the Teflon plugs seated

on the piston to fall down. This step is followed by injection of CO_2 at a low and constant flow rate of 0.5 mL/min to minimize any temperature changes in the vessel during the experiment. Temperature was 200 ± 1 °C through the entire experiment. Pressure and temperature before, during, and after mixing the fluids were monitored and recorded and the results are shown in Figure 10. As it can be seen, the pressure is similar for both water and the PAA aqueous solution from the beginning of the experiment (water vapor pressure) until the first milliliter of CO_2 injected. Then, as the volume of CO_2 increases the PAA solution shows a higher rate of increase in pressure per unit of volume as compared to pure water. Furthermore, this pressure difference increases non-monotonically with the volume added of CO_2 reaching values over 6.9 MPa after 10 mL of CO_2 is added. CO_2 reacts with PAA crosslinking the polymer via forming an ammonium carbamate which can be followed by dehydration to a urea linkage.[9] The stoichiometry for this reaction is CO_2 : PAA 1:2. Since a mole of PAA has an average of 298 equivalents of NH_2, in 39 mL there are 6.8 milliequivalents of NH_2. Therefore, the calculated mass of CO_2 required to stoichiometrically react with 39 mL of 1 wt% PAA (MW= 17,000 g/mol) is 0.15 g or 0.00342 mol of CO_2. This is equal to 0.71 mL (CO_2 density at 25 °C and 6.2 MPa is 0.21 g/mL). Therefore, we hypothesize that the first milliliter of CO_2 injected reacts and crosslinks with PAA when at temperature while the additional volume of CO_2 added, together with the water present, are responsible for the swelling of the crosslinked polymer, and the resulting overpressure observed in Figure 10. The overpressure is directly associated to this volume expansion and a function of CO_2 volume/pressure as well as temperature as it was reported in our first publication (Figure 1).[9] This CO_2-triggered overpressure is one of the responsible mechanisms for fracturing rock samples and fused silica samples at lower net pressures (Figures 8 and 9).

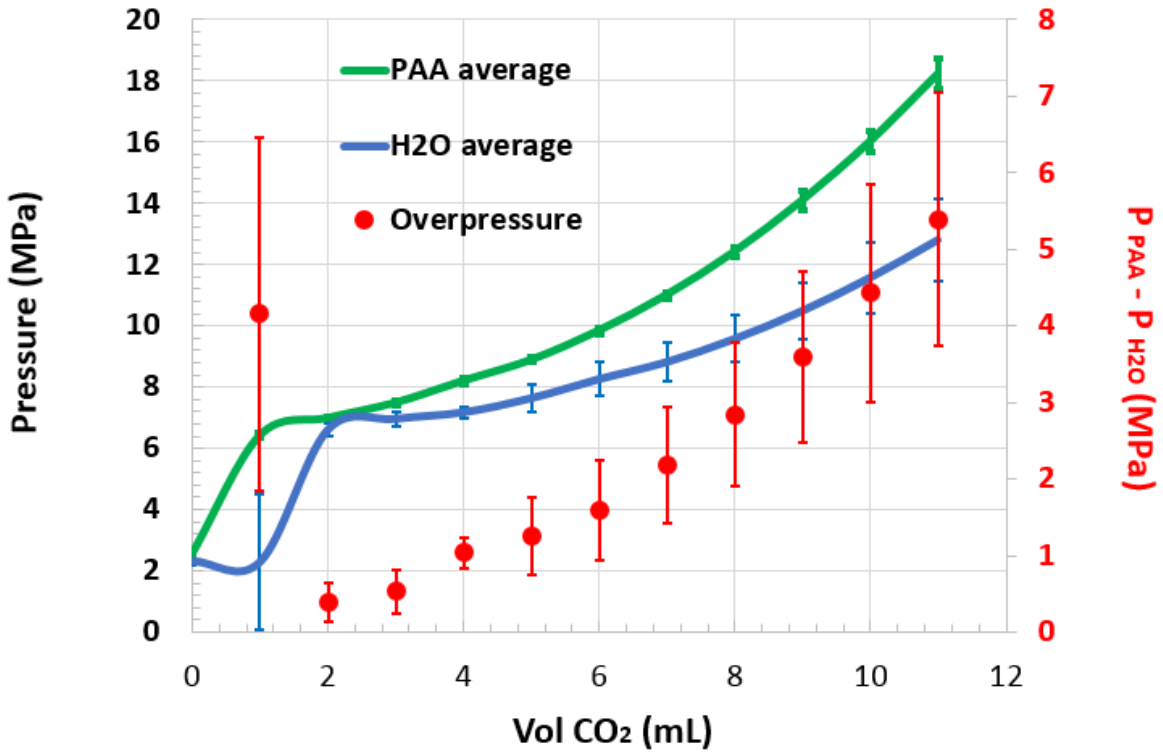

Figure 10. Pressure of a 1 wt% aqueous solution of PAA (green plot) and deionized water (blue plot) as a function of volume of CO_2 injected. The pressure difference between the two plots is also charted (in red) and corresponds to the overpressure triggered by the volume expansion as a result of the reaction of the polymer aqueous solution with CO_2 (Figure 1 and [9]).

Pore invasion pressure

It has been previously reported that interfacial tension between the fluid and the porous solid governs fluid invasion to the matrix of a porous material and, as a result, the breakdown process. Lower interfacial tension for the fracturing fluid-porous solid results in lower pore invasion pressure and breakdown pressure[11]. For example, the negligible interfacial tension in supercritical fluids allow easy invasion into the matrix, while the subcritical fluid with larger interfacial tension requires a higher pressure to invade and cause subsequent breakdown of the borehole[11]. Figure 9 shows lab-scale stimulation experiments on rock specimens from Coso EGS wellbore, with two binary fluids, H_2O/CO_2 and PAA/CO_2. As described in section 3.2.2, Figure 9 shows that PAA/CO_2 fractures at lower average net pressure but, as importantly, there is significantly higher variance in the measured net pressures for PAA/CO_2 as compared to H_2O/CO_2. Since the Coso rock samples represent heterogeneous and porous materials, the larger variability in net pressure from sample to sample when fracturing with PAA/CO_2 seems to indicate a difference in the pore-invasion pressure of this fluid as compared to H_2O/CO_2.

If one of the mechanisms responsible for fracturing at lower net pressures with PAA/CO_2 as compared to H_2O/CO_2 [9, 10] is associated to the above described phenomenon, then the interfacial tension of these fluids would play a key role, with PAA/CO_2 having lower interfacial tension as compared to H_2O/CO_2. Both fluids mixtures are composed of a CO_2 phase with negligible interfacial tension and an aqueous phase with high interfacial tension. The difference lays in the fact that PAA/CO_2 has 1wt% of PAA. PAA, a polymeric surfactant, is expected to play two roles associated to lowering the interfacial tension of the aqueous phase. The first one, is an expected decrease in interfacial tension due to the reduction of water hydrogen bond interactions particularly at the interface due to the accumulation of amphiphilic PAA molecules with weaker interactions. Second, is the chemical reaction that PAA undergoes with CO_2 driving CO_2 (with its negligible interfacial tension) into the aqueous phase with a resulting volume expansion and anticipated decrease in interfacial tension of the aqueous phase particularly at high temperatures.[9, 10]

To determine the first contribution, i.e. the relative interfacial tension values of the aqueous phase of PAA and water, permeability measurements were performed at identical temperatures at which we performed the stimulation experiments (200 °C). These measurements were carried out on a 15-inch column packed with silica fume applying a constant pressure differential of 0.07 MPa between the head and bottom of the column. Both viscosity and interfacial tension contribute to the transport of fluids through porous media. Since the viscosity of aqueous PAA and water are very similar,[9] it is expected that the lower interfacial tension of the PAA solution will provide higher permeability values as compared to plain water. Indeed, the results show that the permeability value of packed silica fume for an aqueous solution of PAA is over an order of magnitude (0.84 millidarcy) higher than its permeability for water (0.053 millidarcy). This is directly associated to the lower (about 1/16) relative interfacial tension of aqueous PAA respect to plain water.

The above results demonstrate that the second responsible mechanism for the reported lower net pressures required to fracture rock cores is the anticipated lower pore invasion pressure by PAA/CO_2 fluid as compared to H_2O/CO_2 as a result of the different relative interfacial tension between the two binary fluids and the solid matrix. The reduction in interfacial tension of PAA/CO_2 is a result of both, the surfactant role by PAA in water and the reaction of aqueous PAA with CO_2 which is anticipated to drive a higher concentration of supercritical CO_2 (with negligible interfacial tension) into the aqueous solution of StimuFrac. As stated earlier, the presence of CO_2 in H_2O/CO_2 fluids may also have an effect in reducing the interfacial tension of the binary fluid and a resulting decrease in pore invasion pressure and fracturing net pressure (Figure 9). However, the effect is limited to the solubility of CO_2 in water under the studied pressure/temperature conditions.

CONCLUSIONS

This work presents a computational and experimental study to gain understanding on the fracturing potential of a novel stimuli-responsive fracturing fluid, StimuFrac™ combined with CO_2. Previous reports on lab-scale stimulation experiments showed an important reduction in net pressures required to fracture different rock specimens when employing StimuFrac™.[9, 10] In this work, we demonstrated that in addition to fracturing porous rock materials at lower net pressures, PAA/CO_2 consistently fractures a non-porous material, fused silica, at significantly (30%) lower net pressures as compared to conventional water-based fluids as well as water-less fluids, such as CO_2. This could result in lower pumping energy and cost. The mechanism responsible for the lower observed net pressures by this novel fracturing fluid were established to be related to two phenomena. First, the additional work / overpressure generated by StimuFrac during its CO_2-triggered volume expansion. We measured for the first time, employing a state-of-the-art constant volume mixing vessel, the overpressure associated to the volume expansion of StimuFrac technology. Second, a reduction in pore invasion pressure as a result of the lower interfacial tension of StimuFrac and the anticipated further reduction of interfacial tension due to its reaction with CO_2. The results presented in this work also illustrate the potential of StimuFrac as a greener (non-toxic) and less-energy intensive fracturing fluid and provides a vehicle for further optimization of the chemical and mechanical properties of this novel fluid for permeability enhancement. For example, variables including CO_2 and PAA concentration, and polymer molecular weight are anticipated to influence interfacial tension, viscosity, density (directly associated to compressibility), and, as a result, the performance of this stimuli-responsive fracturing fluid. Work towards this end has been proposed and will be the subject of a follow-on publication.

Supporting Information.

Figures S1 through S3 described in section 2.4, Fracturing pressure prediction for fused silica specimens: Computational Modeling can be found in the Supporting Information. The Supporting Information is available free of charge on the ACS Publications website.

List of Figures

Figure S1. Finite element mesh used for the computational model of cylindrical sample. The zoomed in portion of the mesh shows localized refinement performed close to the sharp corner at the end of central bore.

Figure S2. Energy release rate obtained at different assumed crack extension directions.

Figure S3. Stress intensity factor against the net pressure (P_{ext} - P_{int}) for three different magnitudes of confining pressure.

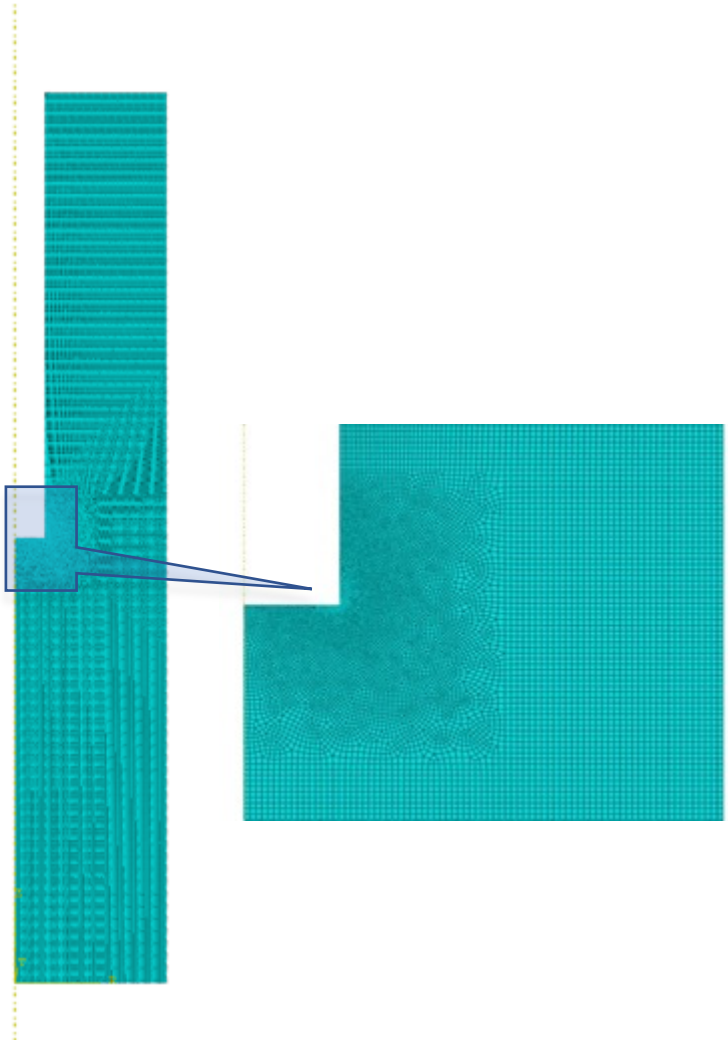

Figure S1. Finite element mesh used for the computational model of cylindrical sample. The zoomed in portion of the mesh shows localized refinement performed close to the sharp corner at the end of central bore.

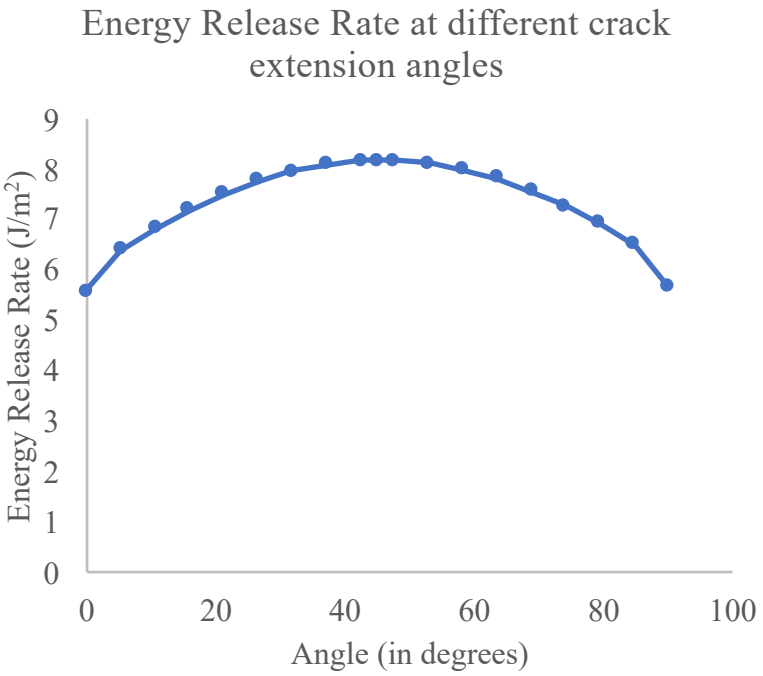

Figure S2. Energy release rate obtained at different assumed crack extension directions.

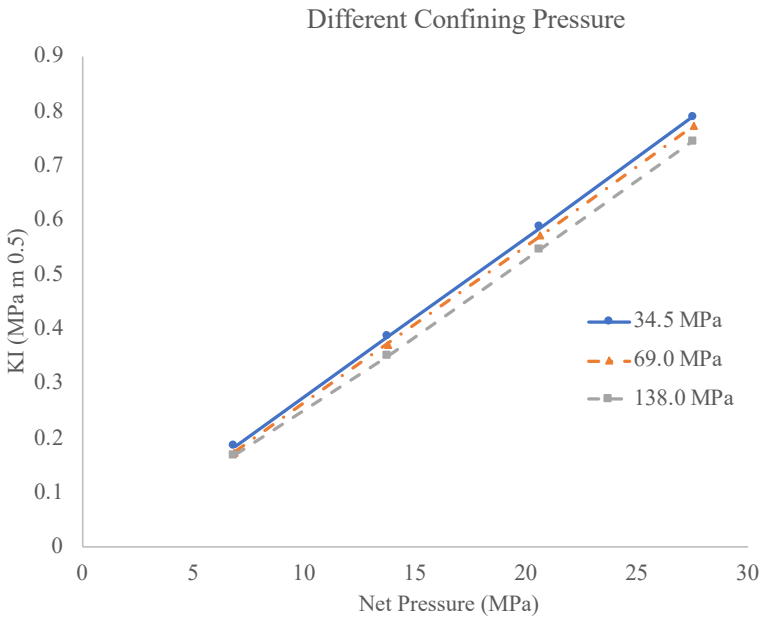

Figure S3 Stress intensity factor against the net pressure (P_{ext} - P_{int}) for three different magnitudes of confining pressure.

Funding Sources

Funding provided by the Department of Energy's Geothermal Technology Office. PNNL is operated by Battelle for the U.S. DOE under Contract DE-AC06-76RLO 1830.

ACKNOWLEDGMENTS

The authors would like to thank Mr. Michael Perkins for its illustration in the suggested cover art.

ABBREVIATIONS

PAA, poly(allylamine); EGS, Enhanced Geothermal Systems

REFERENCES

1. Duffield, W. and J. Sass, *Geothermal Energy-Clean Power From the Earth's Heat: US Geological Survey Circular 1249, 43 p*. 2004.
2. Kargbo, D.M., R.G. Wilhelm, and D.J. Campbell, *Natural Gas Plays in the Marcellus Shale: Challenges and Potential Opportunities.* Environmental Science & Technology, 2010. **44**(15): p. 5679-5684.
3. Pruess, K., *Enhanced geothermal systems (EGS) using CO2 as working fluid—A novel approach for generating renewable energy with simultaneous sequestration of carbon.* Geothermics, 2006. **35**(4): p. 351-367.
4. Kerr, R.A., *Natural Gas From Shale Bursts Onto the Scene.* Science, 2010. **328**(5986): p. 1624-1626.
5. Tester, J.W.e.a., *The Future of Geothermal Energy: Impact of enhanced geothermal systems (EGS) on the United States in the 21st century*, in *Massachusetts Institute of Technology and Department of Energy Report*. 2006: Boston.
6. Garcıa-Ochoa, F., et al., *Xanthan gum: production, recovery, and properties.* Biotechnology advances, 2000. **18**(7): p. 549-579.
7. Jang, B.N., M. Costache, and C.A. Wilkie, *The relationship between thermal degradation behavior of polymer and the fire retardancy of polymer/clay nanocomposites.* Polymer, 2005. **46**(24): p. 10678-10687.
8. Wang, M., J.M. Smith, and B.J. Mccoy, *Continuous Kinetics for Thermal-Degradation of Polymer in Solution.* Aiche Journal, 1995. **41**(6): p. 1521-1533.
9. Jung, H.B., et al., *Stimuli-responsive/rheoreversible hydraulic fracturing fluids as a greener alternative to support geothermal and fossil energy production.* Green Chemistry, 2015. **17**(5): p. 2799-2812.
10. Shao, H.B., et al., *Environmentally friendly, rheoreversible, hydraulic-fracturing fluids for enhanced geothermal systems.* Geothermics, 2015. **58**: p. 22-31.
11. Gan, Q., et al., *Breakdown pressures due to infiltration and exclusion in finite length boreholes.* Journal of Petroleum Science and Engineering, 2015. **127**: p. 329-337.
12. Li, X., et al., *Breakdown pressure and fracture surface morphology of hydraulic fracturing in shale with H2O, CO2 and N2.* Geomechanics and Geophysics for Geo-Energy and Geo-Resources, 2016. **2**: p. 14.
13. Mueller, M.G., et al., *Fracture toughness testing of nanocrystalline alumina and fused quartz using chevron-notched microbeams.* Acta Materialia, 2015. **86**: p. 385-395.
14. Klute, A. and C. Dirksen, *Hydraulic Conductivity and Diffusivity: Laboratory Methods*, in *Methods of Soil Analysis, Part 1 - Physical and Mineralogical Methods*, A. Klute, Editor. 1986, American Society of Agronomy, Inc, Soil Science Society of America, Inc,: Madison, WI. p. 687-734.
15. Anderson, T.L. and T. Anderson, *Fracture mechanics: fundamentals and applications*. third ed. 2005: CRC press, Taylor & Francis Group, Boca Raton, FL 630.
16. Davtzes, N. and S. Hickman, *Stress and Faulting in the Coso Geothermal Field: Update and Recent Results from the East Flank and Coso Wash.* Thirty-First Workshop on Geothermal Reservoir Engineering, Stanford University, Stanford, California, 2006: p. 12.
17. Morrow, C.A. and D.A. Lockner, *Physical properties of two core samples from Well 34-9RD2 at the Coso geothermal field, California.* USGS, 2006: p. 32.
18. Sanchez, J., J. Fullea, and C. Andrade, *Fracture toughness variation induced by stress corrosion cracking of prestressing steels.* Materials and Corrosion-Werkstoffe Und Korrosion, 2008. **59**(2): p. 139-143.
19. Yuan, W., X.R. Liu, and Y. Fu, *Study on Deterioration of Strength Parameters of Sandstone Under the Action of Dry-Wet Cycles in Acid and Alkaline Environment.* Arabian Journal for Science and Engineering, 2018. **43**(1): p. 335-348.
20. Peng, C., et al., *The pH of CO2-saturated water at temperatures between 308 K and 423 K at pressures up to 15 MPa.* Journal of Supercritical Fluids, 2013. **82**: p. 129-137.

Insights into the Physical-Chemical Properties of a CO_2-Responsive Fracturing Fluid

ABSTRACT

Here we determine the phase behavior of StimuFrac, a CO_2 responsive fracturing fluid, under geothermal wellbore conditions. StimuFrac is an aqueous poly(allylamine) fluid that crosslinks in the presence of CO_2. StimuFrac significantly reduces the net pressure required to induce fractures, relative to other fracture fluids, and has potential to reduce water use. However, the phase behavior and equations of state to describe StimuFrac's phase behavior remain unavailable. Here we determine the density and molar volume of the fluid as a function of geothermal relevant temperatures, pressures, and weight fractions of StimuFrac added. In general, experiments find that StimuFrac's density decreases as temperature and pressure increase along the phase envelope. Using these results, equations of saturated state and phase diagrams for different polymer concentrations are reported. These results are critical inputs for planned numerical simulation efforts.

1. INTRODUCTION

Currently, stimulation methods for enhanced geothermal systems (EGS) use very large volumes of water (500,000 – 2,000,000 bbl) to create and propagate fractures and enhance reservoir permeability. Methods typically used in oil and gas development are not appropriate for EGS. For example, Slickwater polymer systems, crosslinked synthetic polymers, and surfactants are not stable at higher temperatures (150-400°C) and can cause irreversible formation damage (Waxman, et al., 2011; Tollefson, 2013; Dunham, 2012; Burden, et al., 2015).

StimuFrac is a stimulation fluid technology that consists of an aqueous polymer solution that undergoes CO_2-promoted volumetric expansions triggered by temperature. StimuFrac is distinct from conventional polymer systems used in hydraulic fracturing operations, because it is the only technology with (a) uniquely controlled CO_2-triggered volume expansion (Jung, et al., 2015), (b) reversible rheology (Jung, et al., 2015), (c) reduced water requirements (Dunham, 2012; Burden, et al., 2015; Jung, et al., 2015; Shao, et al., 2015, 2018), (d) negligible toxicity, (e) high thermal stability (up to 400°C) (Dunham, 2012; Burden, et al., 2015; Jung, et al., 2015; Shao, et al., 2015, 2018), and (f) reversible volume expansion. At the lab-scale (cubic-inch rock samples), the stress associated with this expansion in volume has been shown to consistently create fracture networks through highly impermeable rock under EGS conditions. The significantly lower effective pressure measured when applying StimuFrac compared to the pressures required for alternative fracturing fluids (water, CO_2, and their combination), together with the notable enhancement in permeability, suggests the potential of StimuFrac for cost-effective geothermal energy production with reduced impact to the environment. Despite StimuFrac's potential, key questions remain that can only be answered with quantitative evaluation of physical StimuFrac's physical properties.

Therefore, the objective of this paper is to determine the phase diagrams at representative reservoir temperatures (100-200°C) and pressures (up to 5650 psi or 39.0 MPa) with equations of state for the phase boundaries to permit numerical interpolation. In the remainder of this manuscript, the experimental system and data collected are first described. Then the equation-of-state approach is presented. Finally, the phase diagrams are presented along with experimental data versus temperature,

pressure, and added polymer weight fraction. These results are essential to designing and evaluating deployment strategies with numerical modeling.

2. METHODS

2.1 Experimental Determination of Density and Molar Volume

To numerically determine StimuFrac's phase states at a range of geothermally relevant conditions, a battery of experimental measurements was performed across a range of pressures, temperatures, and added polymer concentrations. The StimuFrac fluid used in this work was prepared by diluting with water a 20 wt% aqueous solution of poly(allylamine) (PAA) (weight average MW ~17 000 g/mol; Sigma Aldrich) to obtain 0.5, 1.0, and 2.0 wt% solutions of PAA. The solution consisted of only PAA polymer and distilled deionized water without any additives. Prior to addition, the PAA had not been reacted to induce crosslinking and remained in its neutral form in all cases.

Experiments were performed in a high pressure/high temperature transmission view cell with an internal volume of 11.2 mL (excluding stirrer and in-cell pressure transducer) and sapphire windows. The view cell was insulated with foam and heated using heating cartridges driven by a PID temperature controller based on a type J thermocouple immersed within the PAA aqueous solution. A glass syringe was used to add the polymer solution to the view cell. Carbon dioxide was introduced to the view cell using an ISCO 100DX pump through a thermally insulated line (inner diameter = 1.08 mm) heated to the same temperature as the transmission vessel. The temperature in the pump itself was measured with a type J thermocouple connected at the end of the pump head and determined to be substantially equivalent to the laboratory room temperature. The line delivering CO_2 was heated with heating tape and insulated with foam. The temperature of the CO_2 delivery line was controlled with a second PID temperature controller and maintained to the same temperature as the view cell.

In a typical experiment, 5 mL of (0.5, 1.0, or 2.0 wt%) aqueous PAA were injected into the empty view cell and heated up to the target temperature (100, 135, 170, or 200°C) while stirring. Stirring of the fluid was performed at the same speed for all the experiments. Once the temperature was constant (±1°C), CO_2 was injected first at constant pressure (8.3 MPa or 1200 psi) by opening the valve to the vessel until flow fell below 0.01 mL/min. Then, the pump was switched to constant flow and run at 0.05 mL/min as provided by the pump controller. Experiments were continuously stepped through selected pressures until the pressure in the pump achieved 39.0 MPa (5650 psi). Cell pressures were increased by pumping in CO_2 over the course of each 2-3 hour experiment. Parameters including pump pressure, CO_2 volume, flow rates, and view cell pressure and temperature were all monitored and logged using LabView Professional Development System 2016 version 16.0. Video recording of fluid behavior was performed by means of a high definition Celestron Handheld Digital Microscope PRO 5MP camera.

Video movie files of each experiment were viewed and stopped at times in the movie corresponding to cell pressures between 8.3 MPa (1200 psi) and 39.0 MPa (5650 psi) at multiples of (3.4 MPa) 500 psi (e.g., (10.3 MPa) 1500 psi, (13.8 MPa) 2000 psi, etc.). Over the temperature and pressure range explored, the fluid remained in two phases separated by a distinct meniscus: an upper CO_2-rich "gas" phase and a lower H_2O-rich "aqueous" phase. Between the two, there sometimes appeared a brown sheet-like region that was assumed to be PAA-rich. However, the appearance of brown layer with the other two phases did not follow a clear pattern. For example, this brown layer appeared within the view window in all the 100°C and 170°C runs and in all of the 200°C runs except at 1.0 wt% PAA run. It did not appear in any of the 135°C runs. Therefore, this sheet-like phase was measured as part of the aqueous phase. In reference experiments that did not employ PAA, the brown layer did not appear. At each point where the movie was stopped, a video measurement tool (markus-bader.de/MB-Ruler) was

used to determine the distance in pixels that the meniscus of the aqueous region was above the bottom of the view window. This distance was then divided by the total pixel diameter of the view window to determine a fraction $0 \leq f \leq 1$ of meniscus height compared to total view window height. This fraction f was compared to a linear calibration curve of aqueous volume versus f to determine the volume of aqueous region in the cell. The remainder of the volume of the pressure cell was attributed to the CO_2-rich 'gaseous' or vapor region of the cell.

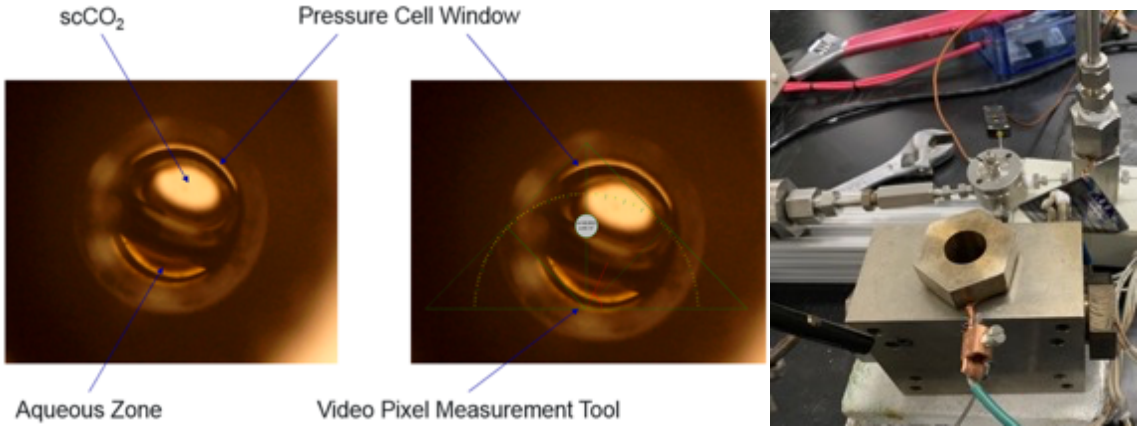

Figure 1: (left) Digital images of the view through the sapphire window of the pressure cell. (right) View of the pressure cell in the foreground with pressure cell window on top and pressurizing cylinder in the background both without superficial insulation and heating systems.

Determination of the density of the aqueous region containing PAA along with CO_2 from the vapor phase was performed as follows. A measured volume of CO_2 was driven slowly from the pump into the pressure cell, and the volume of CO_2 remaining in the pump was monitored at each pressure step. The mass of CO_2 delivered to the pressure cell was computed as being the difference between mass originally in the pump [as determined by initial volume, pressure, and temperature using the NIST webbook (webbook.nist.gov)] less remaining mass in the pump (as determined by volume and pressure in the pump at the current time) and less a small leakage mass determined as described below. The temperature of the pump was constant (~28°C) during the experiment. The pressure cell remained at the target temperature before the introduction of CO_2 heated at the same temperature measured inside the cell to permit the assumption that the gaseous portion of the cell was completely saturated with water vapor at the time of CO_2 introduction. The partial pressure of CO_2 in the gaseous region in the cell was assumed to be equal to the measured cell pressure less the known water pressure at saturation. Analysis assumed that the water vapor pressure and density both at saturation as given by NIST webbook. Also using the NIST webbook, the mass of CO_2 in the vapor portion of the cell was determined using the known temperature and partial pressure of CO_2. The difference between the total CO_2 mass delivered to the cell and the mass of CO_2 in the gaseous region was assumed to be the CO_2 mass absorbed by the aqueous region, consisting of PAA, water and CO_2. The total mass of the aqueous region was then taken to be the known initial mass of PAA and H_2O placed in cell at the beginning of the experiment less the mass of H_2O assumed to be evaporated into gaseous region plus the mass of CO_2 absorbed by the aqueous region.

To correct for any pressure cell leakage occurring over the course of the hours long experiment at high pressures, a reference experiment was performed without PAA, i.e., using only water initially in the cell with CO_2 injected at the same rate and over the same time period as the experiments with PAA. In this well characterized system, the mass of the aqueous region was calculated by assuming saturation of H_2O in the vapor region and saturation of CO_2 in the aqueous region. Specifically, by measuring

aqueous volumes as above and using insight from Efika, et al., (2016) who provide the densities of the CO_2-saturated aqueous phase, predictions of aqueous masses in the reference experiment were made. These were compared to the aqueous masses determined using the procedure described in the above paragraph. The difference between these two masses determined the leakage over the course of the reference experiment. These mass losses were added to the aqueous masses determined from the experiments with PAA.

Though the initial amount of PAA was known and recorded, the distribution of PAA polymer chain lengths was not measured so that the actual polymer composition (as opposed to the initial composition) was not determined in this analysis, even though a chemical crosslinking reaction of the PAA with CO_2 has been identified and reported. To permit use of traditional thermodynamic forms, density data were converted into a saturated liquid molar volume and a saturated vapor molar volume, assuming that the PAA completely reacted into a single polymeric molecule for all temperatures and pressures explored.

2.2 Fitting Approach

Although the videos suggest observation of three phases: a CO_2 rich vapor phase, a water rich liquid phase, and a liquid or solid PAA rich phase, numerical data obtained informed only the first two phases with the latter included in the aqueous phase. These two-phase data were fit with a cubic equation of state. Cubic equations of state were preferential for numerical simulation of StimuFrac performance due to their ability to capture intricate behavior without unnecessary mathematical complication.

As described by Smith, et al., (1996), a generalized cubic equation of state may be written as

$$P = \frac{RT}{V-b} - \frac{\theta(V-\eta)}{(V-b)\left(V^2+\delta V+\varepsilon\right)}\ , \tag{1}$$

where P is the pressure, V is the molar volume, T is the absolute temperature, R is the ideal gas constant, b represents the additional molar volume from the finite molecular size as postulated by van der Waals, and □, □, □, and □ are generalized constants that may be functions of temperature and pressure. The first term is an ideal gas term adjusted for this finite molecular size, and the second term represents the interparticle forces between molecules. Though both terms are important for both phases, the second term dominates the liquid behavior.

The data described above provide two points for every unique pressure-temperature-initial mass percent combination: one for the saturated liquid and one for the saturated vapor. This contrasts with the generalized cubic equation of state that requires information to determine five constants. Progress may be achieved by grouping the data for a given temperature together and fitting the saturated pressure and molar volumes across a given temperature. Put succinctly, the approach here differs from Eq. 1 in that

$$P_{sat} = \frac{RT}{V_{sat}-b} - \frac{\theta(V_{sat}-\eta)}{(V_{sat}-b)\left(V_{sat}{}^2+\delta V_{sat}+\varepsilon\right)}\ , \tag{2}$$

where the subscript sat indicates evaluation at saturation but the temperature has not been marked as being saturated. This is a fundamental distinction because the resulting equations of state are predictive of physicochemical properties only at saturated conditions.

Because the first term is essentially the ideal gas law, the focus of fitting moves to the second term. To determine the fitting of the second term, Eq. 2 may be rearranged as

$$f\left(V_{sat}\right) \equiv \frac{1}{RT - P_{sat}\left(V_{sat} - b\right)} = \frac{\left(V_{sat}{}^2 + \delta V_{sat} + \varepsilon\right)}{\theta\left(V_{sat} - \eta\right)}. \quad (3)$$

For ease of fitting and because $V_{sat}>>b$,[1] we may approximate

$$f\left(V_{sat}\right) \equiv \frac{1}{RT - P_{sat}V_{sat}} = \frac{\left(V_{sat}{}^2 + \delta V_{sat} + \varepsilon\right)}{\theta\left(V_{sat} - \eta\right)} . \quad (4)$$

Therefore, plots of $f(V_{sat})$ versus V_{sat} may provide insight into the intermolecular interactions (for an ideal gas, $f(V_{sat})=\infty$), and one may anticipate a quadratic appearance except near a pole (i.e., where f becomes locally infinite) located at $V_{sat}=$□. The resulting curves may be scaled so that all of the data fall onto a single master curve and then be fit with a bipartite form as the resulting curves suggest.

Fitting of the gas phase data was accomplished in Excel, whereas the liquid phase data was fit using Mathematica, both using expressions suggested by Eq. 4. Constants determined from Eq. 4 as functions of temperature and initial polymer composition were used in Eq. 2 with b=0. Data for which the liquid density substantially exceeded that of pure liquid water were considered to be outliers.

3. RESULTS AND DISCUSSION

The objective of this study is to quantify the phase behavior of StimuFrac, a polymeric fluid, in the range of 100-200°C (212-392°F) for pressures up to 39 MPa (5650 psi) and initial PAA weight fractions of 0.5-2.0 wt%. The remainder of this paper evaluates the data obtained experimentally in the context of the fitting process described above, summarizes the resulting equations of saturated state and culminating phase diagrams, and finally presents liquid density as a function of pressure. Molar volumes and mass densities are mixture values.

3.1 Equations of Saturated State

The expression of Eq. 4 is plotted in Fig. 2 for each of the four temperatures. If the fluid were an ideal gas, the ordinate would be infinite. Yet, the data are finite at multiple conditions in the figure, indicative of significant interparticle forces relative to an ideal gas. In this form of $f(V_{sat})$ versus V_{sat}, the data do indeed collapse across initial compositions onto a single curve for each temperature. This is surprising because the composition may have been expected to play a more prominent role. Yet, the composition appears to play at most a very modest role, perhaps because the concentrations themselves are relatively modest. As suggested by Eq. 4, the saturated vapor data at larger saturated molar volumes do indeed suggest a quadratic appearance with a pole. However, the saturated liquid data are inconsistent with a quadratic-pole mathematical form. Therefore, the saturated liquid and saturated vapor are fit separately. The need to fit liquid and vapor data separately is not particularly surprising, because cubic equations of state are known to struggle with liquid-phase data.

[1] In principle, the value of b may be determined from any one of a number of different expressions, but this value is often considered to be small (Rowley, 2019). For water and CO_2 using the van der Waals and Redlich-Kwong formulations, b=2.1·10^{-5} -4.3·10^{-5} m^3/mol, which confirms that it is usually small compared to the vapor molar volumes, justifying its absence for vapor. For the liquid phase, molar volumes overlap the expected value of b. Because *V must* exceed *b* and because *b* makes little if any numerical improvement in the quality of the curve fitting, *b* is not included for the liquid either.

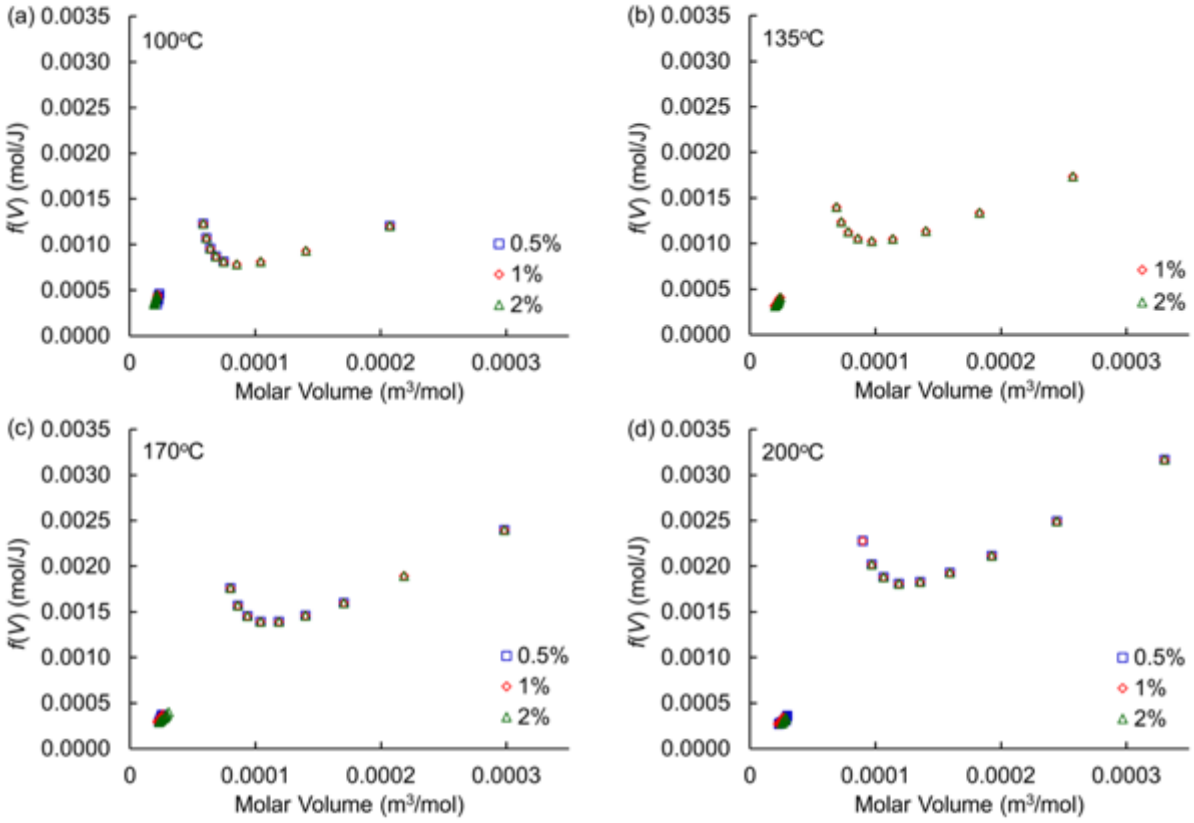

Figure 2: The expression of $f(V_{sat})$ versus V_{sat} as given in Eq. 4. The data for each temperature collapse to a single curve, and the curves across temperatures are qualitatively similar.

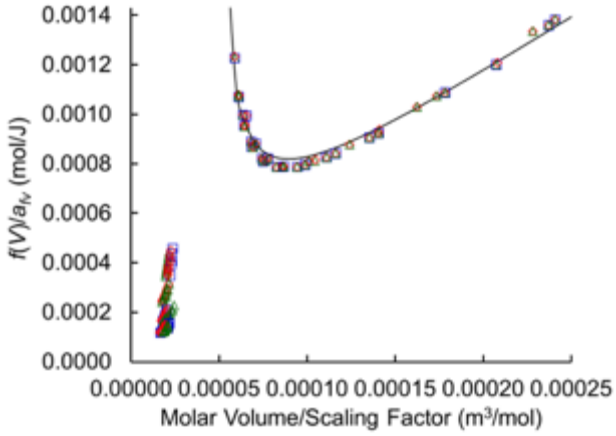

Figure 3: The expression of $f(V_{sat})$ as defined in Eq. 4 scaled on a_{fv} versus V_{sat} scaled on a_v for all of the data in Fig. 2 with corresponding symbols. Scaling factors are $a_{fv}=f(V_{sat},T)/f(V_{sat},100°C)=(0.0000658\ K^{-2})T^2-(0.0427455\ K^{-1})T+7.7835012$ for $T>325$ K and $a_v=V_{sat}(T)/V_{sat}(100°C)=(0.00375\ K^{-1})T-0.40271$, for both of which R^2 exceeds 0.97. Fit given as $f(V_{sat})/a_{fv}=\square_1(V_{sat}/a_v)^2/(V_{sat}/a_v-\square_2)$, where $\square_1=4.575\ mol^2/(J{\cdot}m^3)$ and $\square_2=0.0000448\ m^3/mol$.

Given the similarity of the curves in Fig. 2, the vapor portion of the data (larger molar volumes) may be rescaled using the minimum as a fixed point. Figure 3 shows that the vapor portions of curves at the four temperatures do indeed collapse onto a single curve with appropriate selection of temperature

dependent scaling factors. The collapse of the saturated liquid data is not as compelling, indicating that saturated liquid data need separate scaling, again suggesting a bipartite result. For the vapor, we find

$$f\left(V_{sat}^{\ vap}\right)=\frac{a_{fv}\alpha_1}{a_v}\frac{\left(V_{sat}^{\ vap}\right)^2}{\left(V_{sat}^{\ vap}-a_v\alpha_2\right)}, \tag{5}$$

where a_{fv} is the scale factor for f, a_v is the scale factor for the molar volume, and α_1 and α_2 are fitting constants as determined from Fig. 3. Comparison with Eq. 4 returns $\alpha=0$, $\beta=0$, $\gamma=a_v/(a_{fv}\alpha_1)$, and $\delta=\alpha_2 a_v$. From here, then, the equation of saturated state for the vapor becomes

$$P_{sat}=\frac{RT}{V_{sat}^{\ vap}}-\frac{\theta\left(V_{sat}^{\ vap}-\eta\right)}{\left(V_{sat}^{\ vap}\right)^3}, \tag{6}$$

where

$$\theta=\frac{\frac{0.00375}{\mathrm{K}}T-0.40271}{4.575\left(\frac{0.0000658}{\mathrm{K}^2}T^2-\frac{0.0427455}{\mathrm{K}}T+7.7835012\right)}\frac{\mathrm{J\cdot m^3}}{\mathrm{mol^2}} \tag{7}$$

and

$$\eta=0.0000448\left(\frac{0.00375}{\mathrm{K}}T-0.40271\right)\frac{\mathrm{m^3}}{\mathrm{mol}}, \tag{8}$$

where the temperatures here are absolute temperatures (K), and w is in mass percent not mass fraction. This expression is compared to data in Fig. 4.

Separately, the saturated liquid data, $f(V_{sat}^{\ liq})$ versus $V_{sat}^{\ liq}$, may be fit across all of the data with a polynomial in $V_{sat}^{\ liq}$ that has coefficients β_i that depend on temperature T and mass percent w. The selected quadratic polynomial,

$$f\left(V_{sat}^{\ liq}\right)=\beta_o+\beta_1 V_{sat}^{\ liq}+\beta_2\left(V_{sat}^{\ liq}\right)^2, \tag{9}$$

is chosen in the spirit of a cubic equation of state. After fitting, the coefficients, β_i, become

$$\beta_o=\left(\begin{array}{l}-0.028317+\frac{0.00014729}{\mathrm{K}}T-\frac{2.1779\times10^{-7}}{\mathrm{K}^2}T^2+\frac{7.7492\times10^{-11}}{\mathrm{K}^3}T^3\\ +0.0018059w-\frac{0.000012591}{\mathrm{K}}Tw+\frac{1.0244\times10^{-8}}{\mathrm{K}^2}T^2w+0.0013824w^2\\ +\frac{2.5394\times10^{-7}}{\mathrm{K}}Tw^2-0.00040416w^3\end{array}\right)\frac{\mathrm{mol}}{\mathrm{J}}, \tag{10}$$

$$\beta_1=\left(861.17-\frac{4.2567}{\mathrm{K}}T+\frac{0.0050647}{\mathrm{K}^2}T^2-26.340w+\frac{0.11578}{\mathrm{K}}Tw-5.1227w^2\right)\frac{\mathrm{mol^2}}{\mathrm{J\cdot m^3}}, \tag{11}$$

and

$$\beta_2=\left(6.2541\times10^6-\frac{12176}{\mathrm{K}}T-280144w\right)\frac{\mathrm{mol^3}}{\mathrm{J\cdot m^6}}, \tag{12}$$

where the temperatures here are absolute temperatures (K), and w is in mass percent not mass fraction. Then, the equation of saturated liquid state becomes

$$P_{sat} = \frac{RT}{V_{sat}^{liq}} - \frac{1}{\beta_o V_{sat}^{liq} + \beta_1 \left(V_{sat}^{liq}\right)^2 + \beta_2 \left(V_{sat}^{liq}\right)^3}. \quad (13)$$

The results of this fitting process are also shown in Fig. 4.

3.2 Phase Diagrams and Density Plots

Figure 4 presents phase diagrams predicted from Eqs. 6 and 13. In the figure, the curves at lower molar volumes represent the boundary between liquid only regions and the two-phase saturated region; curves at higher molar volumes represent the boundary between vapor only and the two-phase saturated region. For the vapor boundary, the overlap between the experimental data and equation of saturated state prediction remains remarkably close. Though not perfect, the fits are quite reasonable with essentially a single curve for each temperature. For the liquid boundary, the overlap between the experimental data and equation of saturated state prediction remains reasonable. In contrast to the vapor boundary, the saturated liquid boundary appears to depend on both temperature and on the added PAA mass.

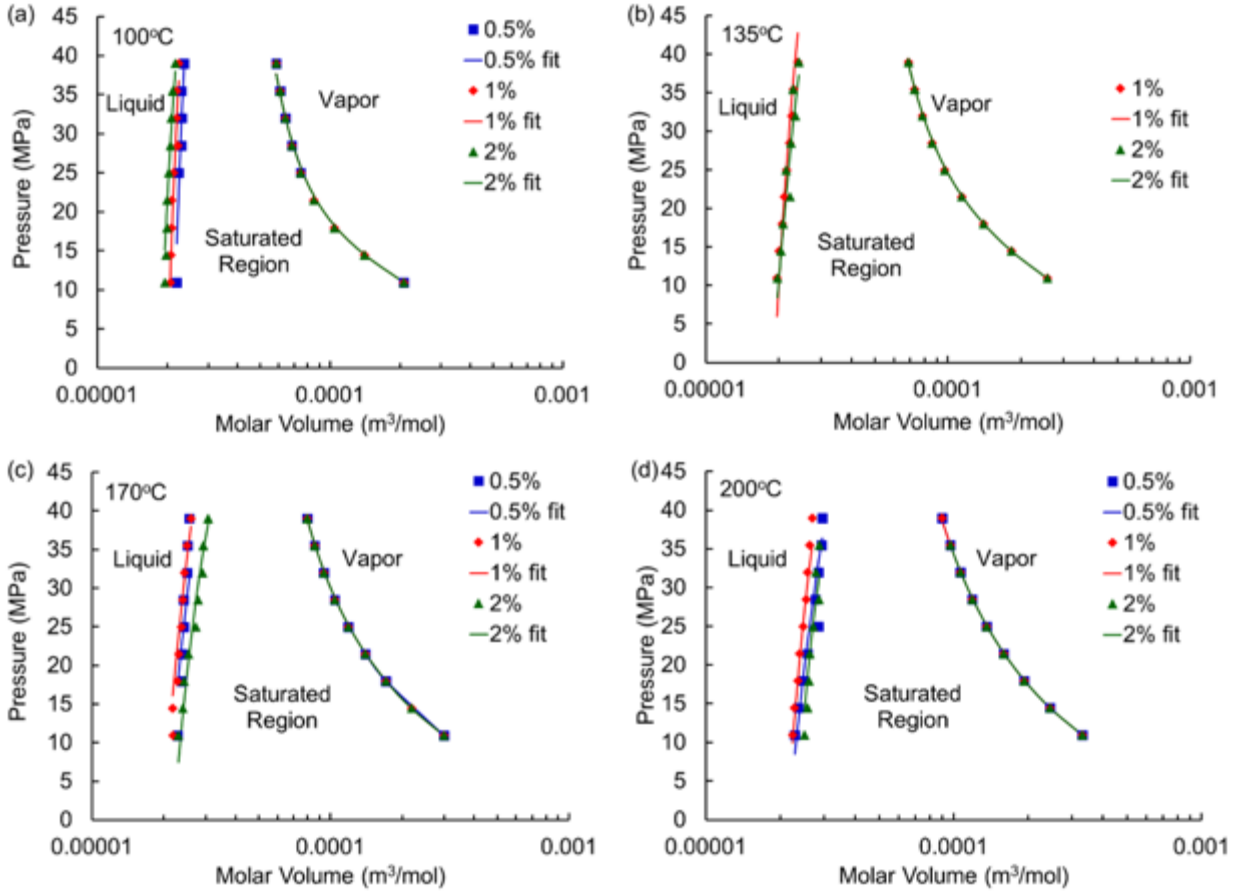

Figure 4: Phase diagrams highlighting the saturation envelope that follows from Eqs. 6 and 13.

The information in Fig. 4 may be converted into plots of density versus pressure as seen in Fig. 5. In general, the experiments found that aqueous phase density decreased as pressure increased along the phase envelop. The match between experiment and prediction remains quite reasonable given that at least some of the variation is experimental. Nevertheless, these results provide critical insight and essential inputs to numerical simulation efforts to come.

4. CONCLUSIONS

In this study, we evaluated the phase behavior of StimuFrac, a PAA rich aqueous fluid known to polymerize in the presence of CO_2. High pressure/high temperature measurements determined the phase envelope in the range of 100-200°C, at pressures at or below 39.0 MPa (5650 psi), and for PAA additions of 0.5-2.0 wt%. Equations of saturated state were used to describe the phase envelope over the range of interest, essential to generating phase diagrams. Predictions of the curves for density versus pressure at saturation across temperatures and added PAA remain in reasonable agreement with experimental determinations of the same.

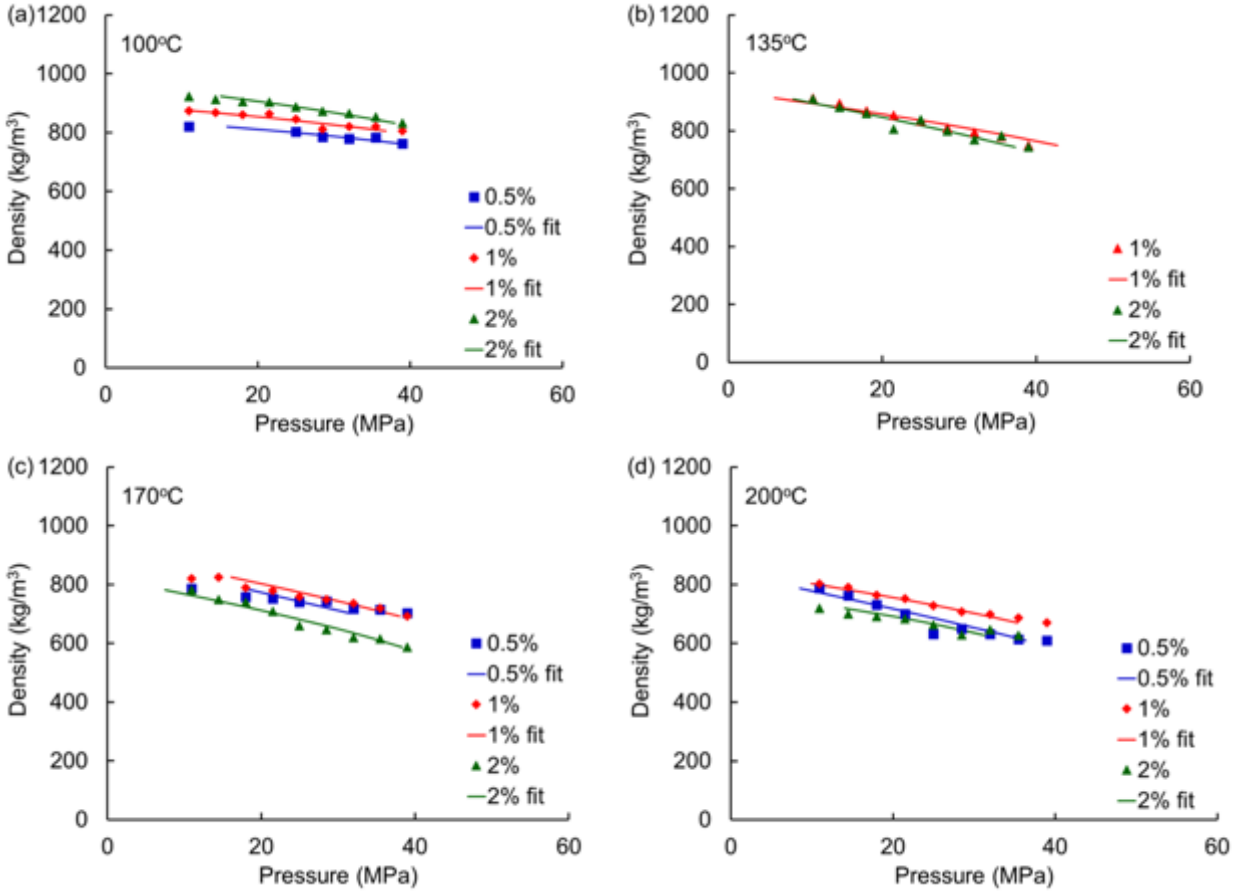

Figure 5: Liquid density versus pressure at saturation along the phase envelope. Conversions from molar volume to density used an approximate molecular weight of 18 g/mol; the average liquid molecular weight varies from 18.0-22.0 g/mol with the addition of CO_2.

5. ACKNOWLEDGEMENTS

Funding for this research was provided by the U.S. Department of Energy's Geothermal Technology Office. Pacific Northwest National Laboratory (PNNL) is a multiprogram national laboratory operated for the U.S. Department of Energy by Battelle Memorial Institute under Contract DE-AC05-76RL01830.

6. REFERENCES

Burden, S., Dean, J., Koplos, J., Meza-Cuadra, C., Singer, A., Tuccillo, M.E.: Analysis of Hydraulic Fracturing Fluid Data from the FracFocus Chemical Disclosure Registry 1.0, Office of Research

and Development, U.S. Environmental Protection Agency, Washington, DC., EPA/601/R-14/003 (2015).

Dunham, J.: Business Impact of Proposed Changes to Well Completion Regulations, *Dunham and Associates*, 2012, https://www.westernenergyalliance.org/wp-content/uploads/2012/05/Revised-Cost-Memo.pdf, downloaded 7/29/2019.

Efika, E.C., Hoballah, R., Li, X., May, E.F., Nania, M., Sanchez-Vicente, Y., and Trusler, J.P.M.: Saturated Phase Densities of (CO_2 + H2O) at Temperatures from (293 to 450) K and Pressures up to 64 MPa, *J. Chem. Thermo*., **93**, (2016), 347–359.

Jung H.B., Carroll, K.C., Kabilan, S., Heldebrant, D.J., Hoyt, D.W., Zhong, L., Varga, T., Stephens, S., Adams, L., Bonneville, A., Kuprat, A., and Fernandez, C.A.: Stimuli-Responsive/Rheoreversible Hydraulic Fracturing Fluids as a Greener Alternative to Support Geothermal and Fossil Energy Production, *Green Chemistry*, **17** (2015), 2799-2812, doi:10.1039/c4gc01917b.

Rowley, R.L.: www.et.byu.edu/~rowley/ChEn273/Topics/Mass_Balances/Single_Phase_Systems/Corresponding_States.htm, downloaded 7/29/2019.

Shao H., Kabilan, S., Stephens, S., Suresh, N., Beck, A.N., Varga, T., Martin, P.F., Kuprat, A. Jung, H.B., Um, W., Bonneville, A., Heldebrant, D.J., Carroll, K.C., Moore, J., and Fernandez, C.A.: Environmentally Friendly, Rheoreversible, Hydraulic-fracturing Fluids for Enhanced Geothermal Systems, Geothermics, **58** (2015), 22-31, doi:10.1016/j.geothermics.2015.07.010.

Shao H., Kabilan, S., Childers, M.I., Stephens, S., Suresh, N., Beck, A.N., Varga, T., Martin, P.F., Kuprat, A. Jung, H.B., Um, W., Bonneville, A., Heldebrant, D.J., Carroll, K.C., Moore, J., and Fernandez, C.A.: Corrigendum to "Environmentally Friendly, Rheoreversible, Hydraulic Fracturing Fluids for Enhanced Geothermal Systems" [Geothermics 58 (2015) 22-31]. Geothermics, **72** (2018) 323-325, doi:10.1016/j.geothermics.2017.12.002.

Smith, J.M., Van Ness, H.C., and Abbot, M.M.: Introduction to Chemical Engineering Thermodynamics. McGraw-Hill: New York, 1996.

Tollefson, J.: Secrets of Fracking Fluids Pave Way for Cleaner Recipe, *Nature*, **501** (2013), 146-147, doi:10.1038/501146a.

Waxman, H.A., Markey, E.J., and DeGette, D.: Chemicals Used in Hydraulic Fracturing, Minority Staff of Committee on Energy and Commerce, *United States House of Representatives*, Washington D.C. (2011).

PHASE II

Evaluation of a Greener Fracturing Fluid for Geothermal Energy Recovery: An Experimental and Simulation Study

ABSTRACT:

The objective of this work is to study the performance of 1wt% StimuFrac fluid [polyallylamine (PAA) in water] in ½-foot size rock samples under thermal and fluid phase conditions representative of enhanced geothermal systems (EGS) and reveal the mechanisms governing the fracturing process. Four fracturing fluids including water, CO_2, CO_2 with water, and CO_2 with aqueous PAA were used.

For all the water "only" fracturing tests, the conductivity of the rock fractured is quite low (less than 2 μm^3 based on radial flow assumption), regardless of the constant pump displacement rate or discrete pressure increments injection approach. For all three CO_2-based fracturing fluids, granite was fractured at higher breakdown pressures, higher transient pump displacement rates, and generated higher-conductivity fractures as compared to water. When partially saturating the rock sample with 1wt% PAA aqueous solution followed by fracturing with CO_2, the volume expansion and viscosity increase triggered by CO_2-induced cross-linking PAA leads to a faster pressure increase than CO_2 in water saturated or initially dry. This faster pressurization rate is caused by a decrease in relative permeability of CO_2 in the presence of the high-viscosity cross-linked fluid compared to the un-crosslinked CO_2/water.

It was also found that CO_2 as a fracturing fluid can generate high fracture conductivity only when injected at very high pump displacement rates in the presence of water or in hot dry rock (HDR). However, the conductivity of CO_2 fracturing in HDR is highly variable. CO_2 injected in the presence of 1wt% aqueous PAA generates fractures with the highest conductivity independently of injection pump displacement rates and using 1/6 of the mass of CO_2 as compared to CO_2 fracturing in HDR.

The results of this study suggest CO_2/PAA is the best performing stimulation fluid under the studied P/T conditions. CO_2/PAA offers the following three additional advantages over waterless CO_2, and CO_2/water fracturing fluids: i) it requires significantly lower volumes of CO_2 due to the reduced leak off; ii) large fractures can be generated reproducibly at both low and high CO_2 injection pump displacement rate, and iii) the reversible (previously reported) viscosity increase could be beneficial to transport proppants when they become available for EGS.

1. INTRODUCTION

Enhanced geothermal systems (EGS) are designed to extract energy from geothermal reservoirs containing hot rock but insufficient natural permeability or fluid saturation. In an EGS reservoir, cold, high-pressure fluid is injected under carefully controlled conditions. The pressurized fluid opens new or pre-existing fractures and flows through them, gradually increasing in temperature as it travels towards a production well. EGS has the potential to make geothermal energy widely available (Lund, 2011; Lund et al., 2005; Lund and Boyd, 2016; Lund and Freeston, 2001).

Hydraulic fracturing is recognized as an efficient way to further increase the permeability of the hot rock, and, as a result, the injectivity and heat exchange efficiency. To fracture the hot rock, operators need advanced stimulation fluids and tools that can withstand high-temperature environments, but many current technologies are designed for low temperatures (e.g., below 70 °C) applications. For example, gellants such as xanthan gum used to increase viscosity and enable proppant transport in tight oil and gas recovery cannot withstand temperatures above 120 °C. It is crucial to develop fracturing fluids that can efficiently fracture hot reservoirs without undergoing degradation of their chemical components. As importantly, operators need stimulation technologies that reduce water requirements, as EGS fracturing operations require on average ten times the water needed for tight oil stimulation operations (Bradford et al., 2014; Chabora et al., 2012). Therefore, research efforts have been also directed to develop alternative fluids that either reduce or completely replace water without a negative impact on fracturing performance.

In this regard, waterless fluid technologies (Isaka et al., 2019; Song et al., 2019), including propellants and fluids such as CO_2, and N_2, have been explored at small scales and in shallow reservoirs. The high-pressure pulses generated by propellants can initiate fractures though concerns remain about their ability to propagate fractures beyond the near-wellbore region and their safe deployment. Our group has recently developed CO_2-reactive fracturing fluids that undergo a volume expansion triggered by the crosslinking reactions between an aqueous polymer solution, polyallylamine (PAA), and CO_2. These reactions and the resulting volume expansion are favored at high temperatures. We demonstrated that this fracturing fluid, hereafter called StimuFrac or simply PAA, can mediate a reversible chemically-activated expansion and viscosity increase in confined environments (B. Jung et al., 2015; Fernandez et al., 2019; Shao et al., 2015). Indeed, high pressure/temperature laboratory-scale experiments that simulated geothermal reservoir conditions at different depths (different confining P and T) demonstrated efficient fracture creation on Coso reservoir samples and in non-porous fused silica samples with rock-like mechanical properties (Fernandez et al., 2019).

Nevertheless, questions remain regarding how the CO_2-triggered volume expansion and rheo-reversible properties impact fracturing performance and how to deploy and optimize StimuFrac-based stimulations in real boreholes. In this work, we report on a series of fracturing experiments in larger (½-foot side) cubic granite rocks and compare the performance of the StimuFrac stimulation fluid to that of water, CO_2, and water/CO_2 in terms of breakdown pressure, permeability enhancement, and volumes of fluid used.

2. MATERIALS AND METHODS

2.1. Fracturing procedure

The sample is placed into the testing apparatus, described in detail in the supplemental material. The loading frame creates the principal stress difference that directs the fracture orientation as occurs in **Fig. 1**. The stress field used in this test is $\sigma_{T-B}/\sigma_{N-S}/\sigma_{W-E}$ =7.58/9.65/9.65 MPa (1100/1400/1400 psi) which means the stress in the direction perpendicular to the top and bottom of the rock sample is the minimum principal stress. All experiments were performed under identical temperature conditions of 200°C. Four different stimulation tests were performed on ½-foot side cubic HDR and pre-saturated samples (Sierra White granite), as shown in **Fig. 1**, at either discrete pressure increments injection mode (i.e., discrete pressure increments) or constant pump displacement rate mode. A notch in the horizontal (radial) direction was created (about 0.1mm deep) and the wellbore was polished to facilitate the introduction of the casing without damaging the O-rings that provide zonal isolation.

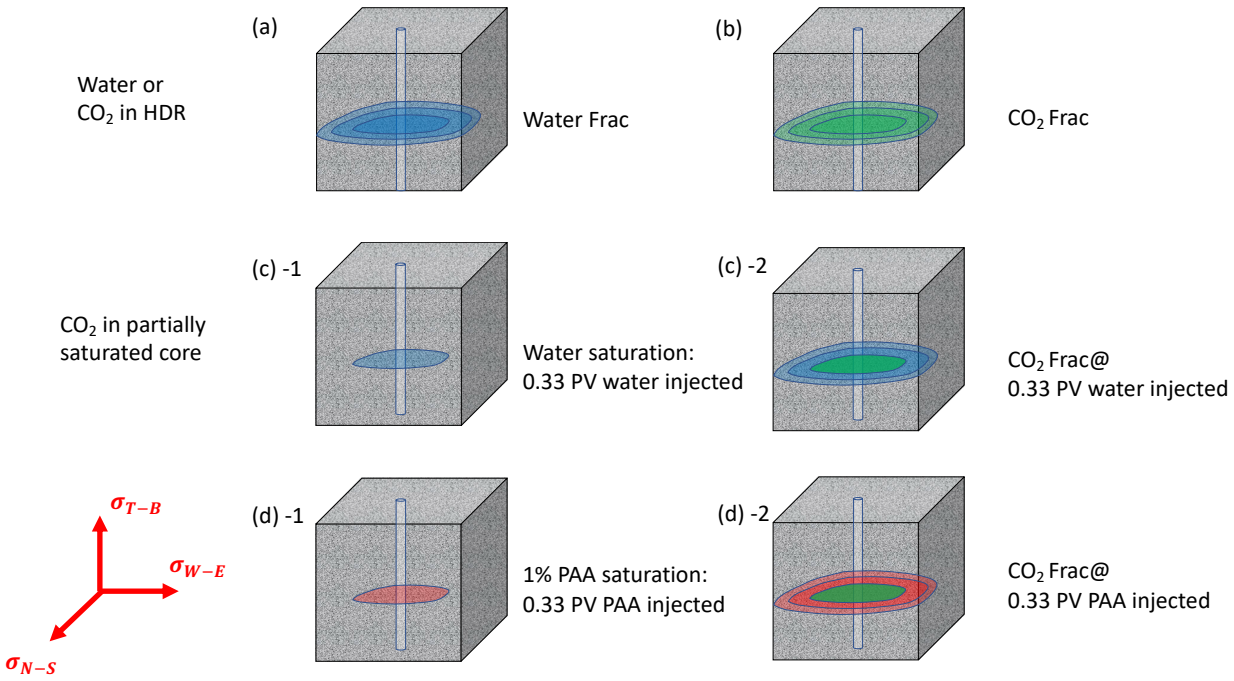

Fig. 1. Four injection strategies for hydraulic fracturing including (a) water fracturing in HDR; (b) CO_2 fracturing in HDR; (c) CO_2 fracturing with rock pre-saturated with 0.33 PV water injection; (d) CO_2 fracturing with rock pre-saturated with 0.33 PV of PAA injection; rock dimension=6"×6"×6"

Four stimulation strategies were used, each of which differs in the initial fluid saturation conditions they create in the sample, and/or which fluid is used to drive the fracture propagation. For each of the four strategies, the fracture can be driven using either a constant-rate injection or using a series of constant-pressure steps. The rock was heated to 200 °C before each test. The four stimulation strategies are described next.

For the first stimulation strategy, referred to in **Fig. 1**a, water was first injected in constant-pressure mode at 6.89 MPa (1000 psi) which is higher than water vapor pressure 1.55 MPa (225 psi) at 200 °C. After the pump displacement rate reached a nominally steady state (due to leakoff from the wellbore), the water fracturing was initiated with constant pump displacement rate or discrete pressure increments mode until the fracture is estimated to have been driven to the edge of the rock. In the plots shown later, this stimulation strategy is labeled simply H_2O. In this condition most of the block is in an unsaturated condition. This is not representative of most subsurface EGS conditions but is a condition that is frequently used in laboratory studies because of the difficulty of saturating such low permeability rocks. It is useful in this study for comparison to other studies and because it offers insight into mechanisms at play in the fracturing.

For the second strategy, referred to in **Fig. 1**b, CO_2 is first injected in constant-pressure mode at 8.96 MPa (1300 psi) until the pump displacement rate reached nominally steady-state (due to leakoff from the wellbore). After that, the CO_2 fracturing is initiated with constant pump displacement rate or discrete pressure increments mode until the fracture is estimated to have been driven to the edge of the rock. In the plots shown this strategy is labeled simply CO_2.The rock in this strategy is also unsaturated, which as discussed above is not representative of EGS conditions but is nonetheless useful for comparison to other studies and for understanding the mechanisms responsible.

For the third strategy, CO_2 fracturing in partially water saturated rock referred to in **Fig. 1**c, water is injected into the wellbore in constant-pressure mode at 8.27 or 8.96 MPa (1200/1300 psi) until 1/3 of the estimated pore volume of rock has been injected. The porosity was estimated to be 1%. It must be noted that the saturation distribution of the water could be heterogeneous such as a higher liquid saturation near the wellbore and a lower water saturation far from wellbore. After this water pre-saturation period, CO_2 is injected in constant-pressure mode at 8.27 or 8.96 MPa (1200 psi or 1300psi). After the pump displacement rate reached a nominal steady-state due to leakoff (about 300 seconds), additional CO_2 is injected into the sample in either discrete pressure

increments (pressure is held for approximately 300 sec at each pressure step) or constant flow-rate mode. In the plots shown later this strategy is referred to as CO_2/H_2O.

For the fourth strategy, CO_2 fracturing in the porous matrix with 1% aqueous PAA partially saturated referred to **Fig. 1**d, is identical to the CO_2/H_2O strategy except that instead of pre-saturating the rock sample with water, the rock is saturated with 1wt% aqueous PAA. In the plots shown later this strategy is referred to as CO_2/PAA.

In the third and fourth strategy the rock is closer to the water saturated conditions that prevail in most real candidate EGS reservoirs. The pore pressure, however, varies from 1200-1300 psi near the wellbore to atmospheric pressure at the edge of the block, which is of course lower than would exist in a deep EGS reservoir. To our knowledge, no laboratory polyaxial tests in low permeability crystalline rock or mudstones have been conducted under elevated pore pressure conditions, and the vast majority are conducted under so-called as-received partially saturated conditions. There are two primary reasons for this. First, even though fluid pressure within a fracture reacts against the total stress acting in the surrounding rock, the fracturing process itself is generally believed to be governed by difference between the principal stresses (often called the differential stress), and by the difference between the fracturing fluid pressure and the total rock stress (often called the net pressure). The fundamental equations of linear elastic fracture mechanics, most commonly assumed to govern hydraulic fracturing, do not involve the absolute values of the stresses or the pore pressure. The second reason for laboratory tests with low permeability rocks generally being performed without full water saturation or elevated pore pressure is that saturating large samples of such low permeability rock is difficult to achieve and very time consuming. The extreme time and expense to achieve this condition is not judged necessary given the first reason (Ghassemi, 2012; Hu et al., 2020; Kamali and Ghassemi, 2018; Lu and Ghassemi, 2019; Ye and Ghassemi, 2019, 2018).

This type of testing has a much longer history for petroleum applications than for geothermal applications. To our knowledge, of the polyaxial hydraulic fracturing tests in the literature focusing on EGS all have been conducted at relatively low temperature conditions (Ghassemi, 2012; Hu et al., 2020; Kamali and Ghassemi, 2018; Lu and Ghassemi, 2019; Ye and Ghassemi, 2019, 2018). Similar to the argument made above justifying low pore pressure conditions, the rock temperature does not directly enter into the equations of linear elastic fracture mechanics that are generally assumed to govern hydraulic fracture propagation. It is likely that the fracture toughness, for example, is temperature dependent and so temperature may enter indirectly, though most likely adding a second-order effect as far as advancing EGS stimulation technology. Because of this, the added difficulty and hazard of working with superheated fluids is avoided because there is little apparent value. The multi-phase flow conditions introduced by fracturing with CO_2 and the cross-linking reactions introduced by the CO_2/PAA solution change this calculation. The cross-linking reaction is strongly temperature dependent, so to test the hydraulic fracturing performance of this fluid requires the elevated temperatures used in the experiments studied. Furthermore, since CO_2 is in a supercritical state at EGS conditions, stimulation with CO_2 will involve multiphase flow both within the fracture and in the rock matrix through leakoff. Unlike fracturing with water in a water saturated rock, this requires consideration of relative permeability effects. The testing protocols devised here represent a significant step (1) in the direction of enabling the study of fracturing fluids that have significantly different properties at elevated temperatures and (2) at studying the effects of multi-phase flow. By achieving partial water saturation and keeping water in a liquid phase near the center of the blocks, where the fractures are propagating, we believe that the testing protocol devised here largely preserves these physics as they would occur under field conditions. With that being said, as discussed below, the atmospheric pressure on the periphery of the block allows a steam phase to develop. This is expected to only have a minor effect on leakoff and to influence fracture propagation at the very edge of the block where the stress field is also strongly influenced by the boundary.

2.2. Preparation of rock thin sections and optical microscopy analysis

The five thin sections were prepared from the split rock surfaces for the five-injection strategies: 1) water fracturing in HDR (Q=2 mL/min); 2) water fracturing in HDR (Q=25 mL/min); 3) CO_2 fracturing in HDR (Q=10 mL/min); 4) CO_2 fracturing (Q=10 mL/min) with rock pre-saturated with 0.33 PV water injection; 5) CO_2 fracturing (Q=10 mL/min) with rock pre-saturated with 0.33 PV PAA injection. Different minerals were stained with different colors. The color codes by stains of the thin section are K-Feldspar Stain(yellow); Plagioclase Stain (orange red); Calcite Stain (pink-red); Iron Stain(blue); Others(quartz): white or grey. Red fluorescent epoxy was

used for vacuum/pressure impregnation. A microscope (type 020-520.716 DM LM/P, Bartels & Stout, Inc. distributed by Leica) was used and a camera (Model#LU1276C-CLX, Clemex Technologies Inc) was connected to the microscope to capture the images of thin sections with 100x or 50x magnifications.

3. RESULTS AND DISCUSSIONS

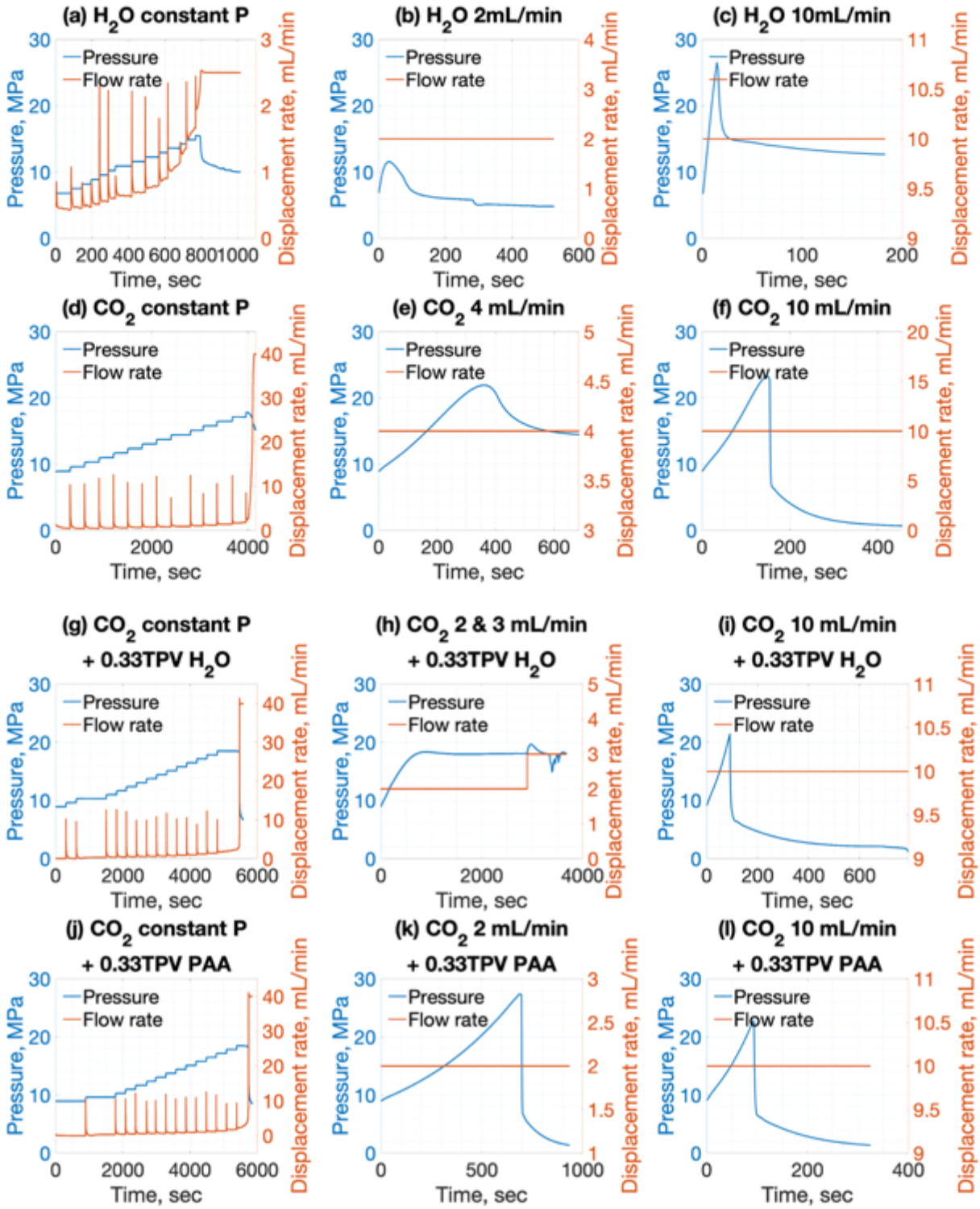

Fig. 2. Fracturing with four different injection strategies (H_2O, CO_2, CO_2/H_2O and CO_2/PAA) with discrete pressure increments or constant pump displacement rate mode

3.1. Stimulation with water

Fig. 2a to c show the pressure and pump displacement rate history for fracturing tests using water in HDR. The fracture initiation pressure is difficult to be determined accurately from the pressure record as shown in **Fig. 2**a. It appears to have occurred somewhere between 11.72 MPa (1700 psi) and 13.79 MPa (2000 psi), where there is a clear increase in pump displacement rate during which the discrete pressure increments hold. The pump displacement rate increases during each pressure step until about 13.79 MPa (2000 psi) at which point the fracture begins to grow unstably around 550 seconds in **Fig. 2**a. Following the sharp decline in pressure between 800 and 850 seconds, the pressure declined more gradually, which would be interpreted as slow, leakoff-dominated fracture growth until pumping of water is stopped at about 1020 seconds. When the fracture grew unstably, a volume of fluid that was originally stored elastically in the wellbore/pump is discharged into the fracture. For fracturing using constant pump displacement rate as shown in **Fig. 2b** and **c**, water was pressurized to 6.89MPa (1000psi) first, then the pump was changed to constant pump displacement rate mode (2 mL/min or 10 mL/min or 25 mL/min) and water was injected into the wellbore until the rock fractured. To inhibit healing of the hydraulic fracture (Jian et al., 2020b), an oil (Dynalene HT oil) slug is injected into the rock after the rock was fractured for subsequent permeability tests.

3.2. Stimulation with CO_2

Fig. 2d to **f** shows the pressure and pump injection rate history for fracturing tests performed by injecting CO_2 in HDR at constant pressure mode, and constant pump displacement rate mode (4 mL/min and 10 mL/min) respectively. CO_2 was pressurized to 8.27/8.96MPa (1200/1300psi) within the pump before injection. As shown in **Fig. 2d,** for discrete pressure increments mode fracturing, the pressure at each incremental step is held for around 300 seconds until the rock is fractured. A faster discrete pressure increment fracturing using CO_2 was also conducted holding pressure for 120 seconds at each pressure step. For fracturing using constant pump displacement rate as shown in **Fig. 2e** and **Fig. 2f,** CO_2 was pressurized to 8.96MPa (1300psi) first, then the pump was switched to constant pump displacement rate (4 mL/min or 10 mL/min) and CO_2 was injected into the wellbore until the rock was fractured.

3.3. Stimulation with CO_2/H_2O

Fig. 2g to **i** show pressure history for the fracturing tests by injecting CO_2 into the 1/3 total pore volume (TPV) of water-saturated rock with either discrete pressure increments mode or constant flow mode. For CO_2 injection in discrete pressure increments mode, as shown in **Fig. 2g**, the pressure at each incremental step is held for around 300 seconds until the rock gets fractured. For fracturing using constant pump displacement rate (**Fig. 2h** and **i**), CO_2 was pressurized to 8.96 MPa (1300 psi) first with the pump in discrete pressure increments mode. Then, the pump was switched to constant flow mode (2 & 3 mL/min or 10 mL/min) and CO_2 was injected into the wellbore. For the experiments where CO_2 is injected at 2 mL/min (**Fig. 2h**), the pressure stabilizes and reaches a steady state. Therefore, the pump displacement rate was increased to 3 mL/min with a resulting temporary increase in pressure followed by a pressure reduction to steady values similar to the ones observed at 2 mL/min. No rock breakdown was observed. The pressure fluctuation observed during the injection of CO_2 at 3 mL/min may be caused by the water saturation changes due to drainage at a high fractional flow of the wetting phase (water).

3.4. Stimulation with CO_2/PAA

Similar to the above-described fracturing using CO_2 in partially water-saturated granite (1/3 of TPV), CO_2 was injected in granite partially saturated with PAA. **Fig. 2j** shows one of the fracturing tests performed by injecting

PAA solution at discrete pressure increments to saturate about 1/3 of the TPV followed by injection of CO_2 in discrete pressure increments. In this experiment, the pressure at each incremental step was held for around 300 seconds until the rock fractured. For fracturing experiments by injecting CO_2 at constant pump displacement rate (**Fig. 2k** and **Fig. 2l**), CO_2 was first pressurized to 8.27/8.96 MPa (1200/1300 psi). Then the pump was switched to constant pump displacement rate mode (2 mL/min or 10 mL/min) and CO_2 was injected into the wellbore followed by penetrating the PAA partially saturated rock. Contrary to the case where the rock was partially saturated with water (**Fig. 2h**), CO_2 (Q=2 mL/min) fractured the rock partially saturated with PAA.

3.5. Diagram of conductivity versus breakdown pressure (Pb) or pressurization rate

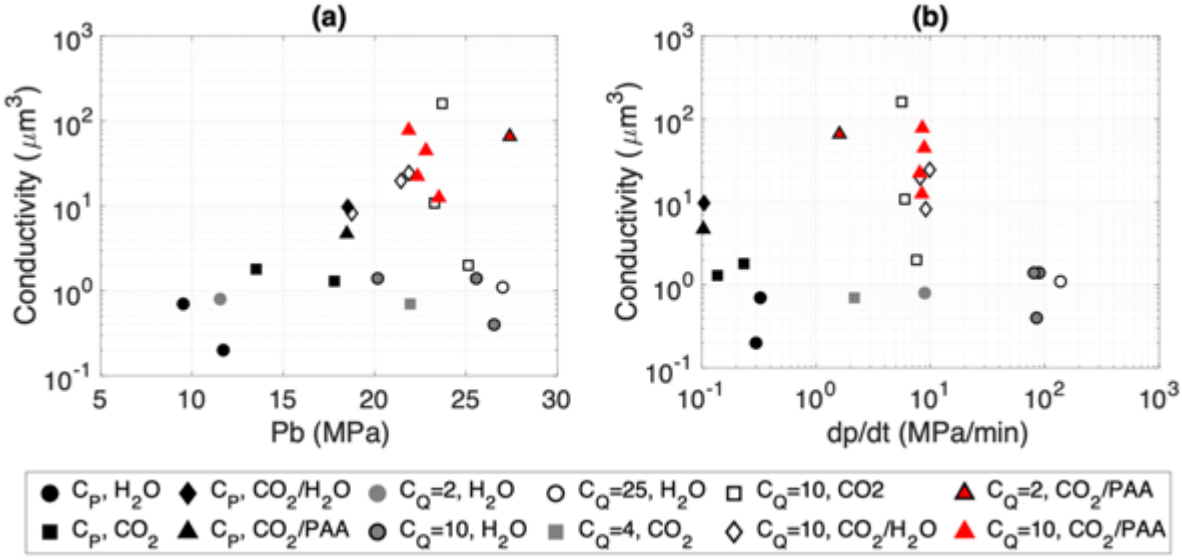

Fig. 3. (a) conductivity of fracture versus breakdown pressure with different injection modes; (b) conductivity of fracture generated as a function of pressurization rate of fluids injected.

Fig. 3 summarizes the fracture conductivity versus breakdown pressure or pressurization rate for the different fracturing fluids at constant pump displacement rate and discrete pressure increments modes. All the tests were conducted at 200 ºC. The circle symbols in **Fig. 3** represent the first stimulation strategy, water injection in HDR. The breakdown pressure ranged from 9.65 MPa (1400 psi) to 26.89 MPa (3900 psi), with fracture conductivity values lower than 2 μm^3 independently of injection strategy, i.e., at either discrete pressure increments or constant pump displacement rate (up to 25 mL/min).

The second stimulation strategy, i.e., CO_2 injection in HDR (square symbols in **Fig. 3**) generated fractures with a wide range of conductivity values. When injecting CO_2 in HDR using discrete pressure increments mode the conductivity is low. The same low conductivity values are observed for constant pump displacement rate injection mode when the pump displacement rate is 4 mL/min but noticeably increases (2.0-4.2 μm^3, 10.8-23.1 μm^3, and 160-341 μm^3) at high (10 mL/min) pump displacement rates though with fracture conductivity values that differ by an order of magnitude.

Diamond symbols in **Fig. 3** represent CO_2/H_2O stimulation strategy, i.e., injecting 0.33 TPV water at discrete pressure increments followed by CO_2 injection in discrete pressure increments or at constant pump displacement rate. When comparing discrete pressure increments injection regimes, CO_2/H_2O stimulation strategy resulted in relatively higher fracture conductivity compared to water in HDR or CO_2 in HDR. However, for CO_2/H_2O stimulation strategy, fracturing efficiency was negligible at low injection rates and the rock was fractured only at high injection rates (10 mL/min) with conductivity values in the 8.2-51.9 μm^3 range.

The fourth stimulation strategy, CO_2/PAA (triangles symbols in **Fig. 3**), with discrete pressure increments injection mode fractured granite at similar breakdown pressures as CO_2/H_2O. However, in constant pump displacement rate mode, CO_2/PAA consistently attained very large conductivity values (with two of the largest measured) independently of injection pump displacement rate (10 mL/min: 12.5-139.5 μm^3; 2 mL/min: 65.7-139.5 μm^3). It is also important to note that CO_2/PAA stimulation strategy consistently generated highly conductive fractures independently of injection mode (discrete pressure increments or constant pump displacement rate).

Fig. 3b shows the effect of the pressurization rate of fracturing fluids on fracture conductivity. Pressurization rate is calculated based on the fluid pressure increase divided by the time when rock fractures. In general, for all stimulation strategies, the higher the pressurization rate, the higher is the fracture conductivity. The exception are the tests conducted with H_2O injected in HDR, where the conductivity of the fracture is less than 2 μm^3 for both discrete pressure increments and constant pump displacement rate tests even at pump displacement rates as high as 25 mL/min.

For the second stimulation strategy, CO_2 fracturing in HDR, low injection rates generate low conductivity fractures while rapid (constant flow, 10 mL/min) injection generates conductivity values (with large variability up to two orders of magnitude). The same trend applies to stimulation strategy CO_2/H_2O. The exception is the injection strategy of CO_2/PAA. This stimulation strategy consistently generated highly conductive fractures independently of pressurization rate as shown in red triangle symbols in **Fig. 3**b. The reason for this will be discussed next.

It is important to note that there may exist a temperature gradient in the near well bore region which may affect the fracturing process. Once the CO_2 reaches the center of the rock, it will penetrate through the pore media of the rock. CO_2 will decrease the temperature of the rock near the wellbore. Therefore, a temperature gradient (in both fluid and rock) exists in a domain from the wellbore (center of the rock) to the surface of the rock (as the thermal conductivity of the rock is anticipated to be low), which will affect the CO_2 fracturing process. (Zhou et al., 2019) investigated the injection of CO_2 at 5°C on rock samples heated at different temperature (25-100 °C) and found that the breakdown pressure decreases as the temperature of the rock increases. They also proposed that the thermal stress in the rock when using cold CO_2 as a fracturing fluid can help generate a more branched fracture network around the main fracture. In our study, this may be one of the factors contributing to the larger conductivity of rock samples fractured with CO_2 as compared to those fractured with water.

Table 1 reports values of breakdown pressure, fracture conductivity, permeability and aperture, as well as water (or aqueous PAA), and CO_2 mass consumption. The injected masses of water (or 1% PAA) and CO_2 were calculated within the time range between the beginning of pressure steps (or constant pump displacement rate) injection to the time when breakdown pressure was reached. As shown in Table 1**,** for the CO_2/H_2O stimulation strategy (entry 16), when the pump displacement rate of injected CO_2 equals to 2mL/min or 3 mL/min, the rock does not fracture. Similarly, when injecting CO_2 in HDR at low/intermediate pump displacement rates the stimulation generates low fracture conductivity (entry 12). Discrete pressure increments injection mode generally consumes more CO_2 than constant pump displacement rate mode due to the time interval (300 sec) between pressure steps. This can be noted by comparing entries 3 and 4 versus entries 13 through 15 (stimulation strategy CO_2 in HDR), by comparing entry 5 against entries 17 through 19 (stimulation strategy CO_2 in rock partially saturated with water) and entry 6 with entries 21 through 24 (stimulation strategy CO_2 in rock partially saturated with aqueous PAA).

Table 1**.** Summary of fracturing results with different stimulation strategies/fluids with constant pressure or pump displacement rate injection modes

Test	Rock ID	Mode/Rate	Strategy	P_b	C_f	K_f	h	m_{H_2O} / m_{PAA}	m_{CO_2}
		(mL/min)		(MPa)	(μm^3)	(μm^2)	(μm)	(g)	(g)
1	#7	C_P	H_2O	*11.72	*0.2-0.4	*0.2-0.3	*1.4-1.7	8.3	0
2	A8	C_P	H_2O	9.53	0.7-1.5	0.3-0.6	2.0-2.6	1.2	0
3	#9	C_P	CO_2	13.52	1.8-3.8	0.7-1.1	2.8-3.6	0	43.7
4	A9	C_P	CO_2	17.80	1.3-2.8	0.5-0.9	2.5-3.2	0	49.6
5	A6	C_P	CO_2/H_2O	18.53	9.7-20.5	2.0-3.3	4.9-6.3	11.3	42.4
6	A5	C_P	CO_2/PAA	18.48	4.7-10.0	1.22-2.0	3.8-4.9	11.3	55.9
7	B3	$C_Q = 2$	H_2O	11.55	0.8-1.7	0.4-0.6	2.1-2.7	0.9	0
8	D4	$C_Q = 10$	H_2O	26.54	0.4-0.8	0.2-0.4	1.7-2.1	1.3	0
9	D5	$C_Q = 10$	H_2O	25.57	1.4-2.9	0.5-0.9	2.5-3.3	0.8	0
10	D6	$C_Q = 10$	H_2O	20.17	1.4-3.0	0.6-0.9	2.6-3.3	1.2	0
11	B8	$C_Q = 25$	H_2O	27.01	1.0-2.1	0.4-0.7	2.3-2.9	0.6	0
12	B10	$C_Q = 4$	CO_2	21.95	0.7-1.5	0.4-0.6	2.0-2.6	0	9.7-14.5
13	B2	$C_Q = 10$	CO_2	23.70	160.6-341.1	12.9-21.3	12.4-16.0	0	7.8-12.8
14	C1	$C_Q = 10$	CO_2	23.28	10.8-23.1	2.2-3.6	5.0-6.5	0	4.0-8.3
15	C7	$C_Q = 10$	CO_2	25.13	2.0−4.2	0.7-1.1	2.9-3.7	0	5.6-9.5
16	B1	$C_Q = 2\ or\ 3$	CO_2/H_2O	N/A	No frac	No frac	No frac	11.3	N/A
17	B1	$C_Q = 10$	CO_2/H_2O	21.44	19.7-41.8	3.2-5.3	6.2-7.9	11.3	0-2.5
18	C8	$C_Q = 10$	CO_2/H_2O	21.88	24.4-51.9	0.7-1.1	6.6-8.5	11.3	0-2.1
19	C9	$C_Q = 10$	CO_2/H_2O	18.75	8.2-17.5	1.8-3.0	2.9-3.7	11.3	0-1.9
20	A10	$C_Q = 2$	CO_2/PAA	27.40	65.7-139.5	7.1-11.8	9.2-11.9	11.3	1.1-4.9
21	B7	$C_Q = 10$	CO_2/PAA	22.81	44.7-95.0	5.5-9.1	8.1-10.5	11.3	0-2.3
22	D3	$C_Q = 10$	CO_2/PAA	21.87	77.7-165.1	8.0-13.2	9.8-12.6	11.3	0-0.9
23	D7	$C_Q = 10$	CO_2/PAA	22.35	22.3-47.3	3.5-5.7	6.4-8.3	11.3	0-0.9
24	D8	$C_Q = 10$	CO_2/PAA	23.52	12.5-26.5	2.4-3.9	5.3-6.8	11.3	0-2.0

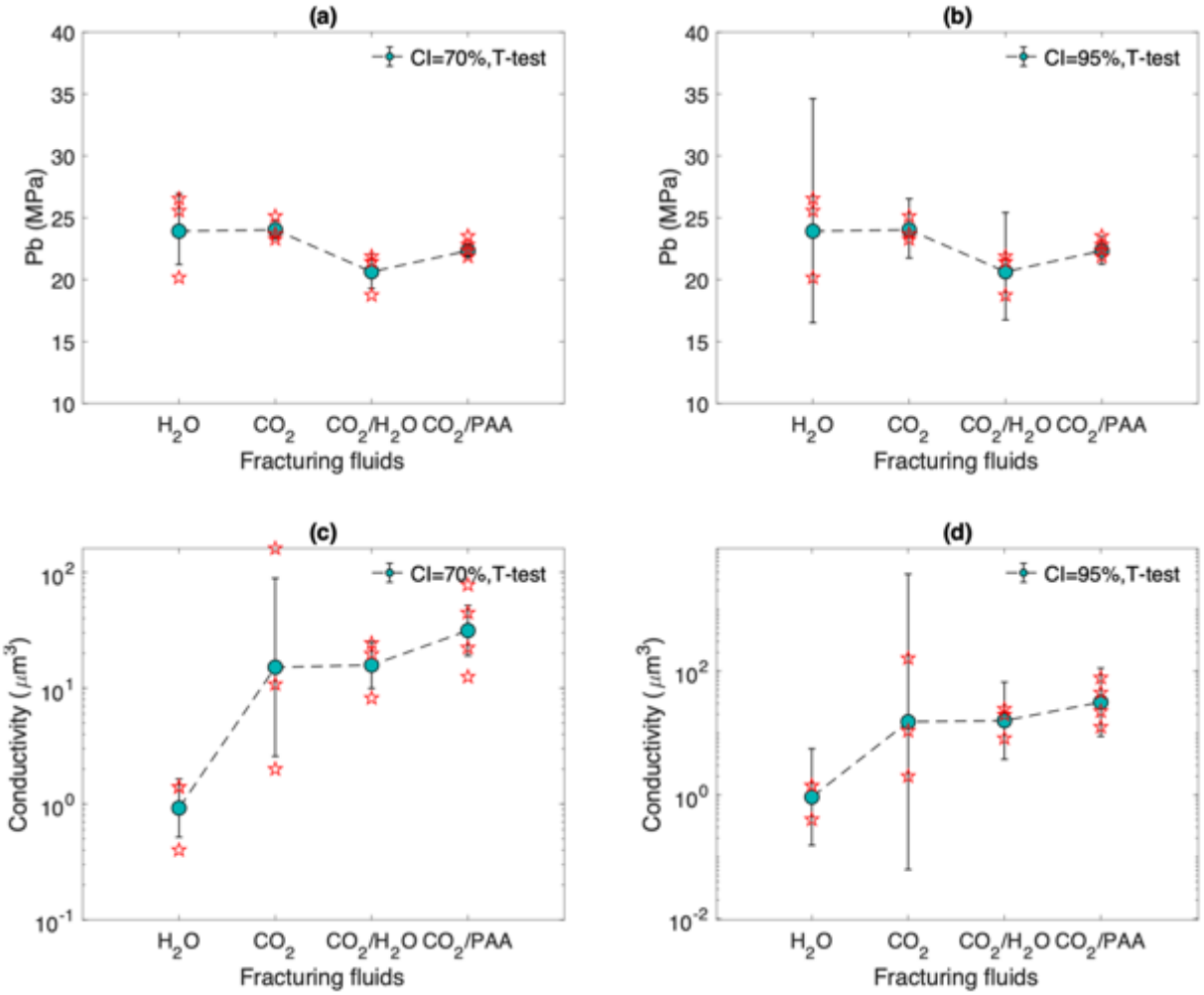

Fig. 4. Breakdown pressure (a) with 70% confidence interval and (b) with 95% confidence interval; conductivity (c) with 70% confidence interval and (d) with 95% confidence interval for four fracturing strategies at 10 mL/min

Fig. 4a and b are plots of the observed mean breakdown pressures (marker) with Student's T distribution assuming a lognormal distribution. A lognormal distribution (Heath, 1967) is used because it is generally more appropriate for strength/fracture estimations since it only admits positive values. The error bars indicate the 70% confidence interval for the true mean. At this level of confidence, the CO_2/PAA, at 10 mL/min injection rate has a higher true mean breakdown pressure than CO_2/H_2O and lower than CO_2 in HDR. Water has a higher degree of variability at 10 mL/min than the CO_2-based fluids. There is no statistical difference (70% or 95% confidence level) in breakdown pressure using H_2O or CO_2 when injecting at 10 mL/min.

Fig. 4c and d are plots of the observed mean fracture conductivity values for each testing condition along with confidence intervals using the same approach discussed above and assuming that the fracture conductivity follows a lognormal distribution (Bee et al., 1995). At 10 mL/min, all CO_2-based fluids outperform water at 70% confidence level. CO_2/PAA performs better than CO_2/H_2O, at both 70% and 95% confidence level for fracture conductivity.

3.6. *Pump pressure and pump displacement rate of fracturing fluids deployed in discrete pressure increments injection mode*

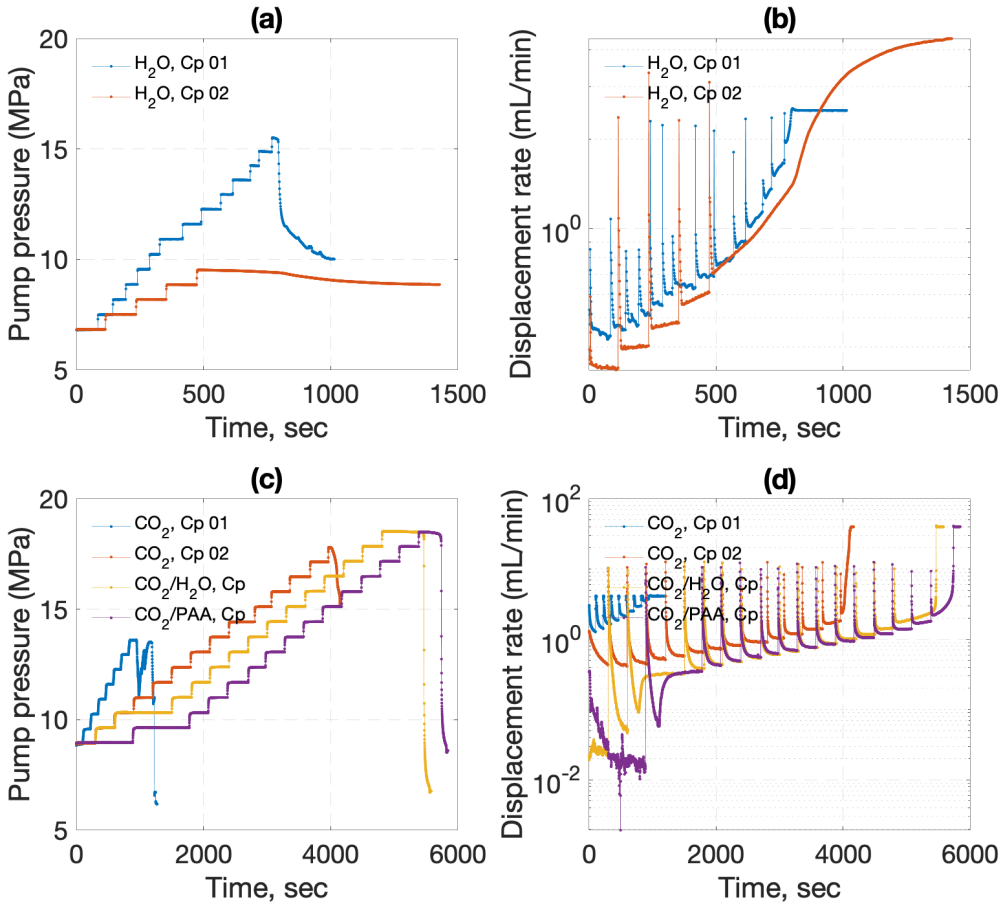

Fig. 5. (a) Pump pressure history and (b) pump displacement rate history of two water fracturing test in constant-pressure mode; (c) pump pressure history and (d) pump displacement rate history of three stimulation strategies: CO_2 in HDR, CO_2/H_2O, and CO_2/PAA at discrete pressure increments mode. All tests were conducted at 200 °C.

Fig. 5a to b show the pump pressure and pump displacement rate history of injected fracturing fluids for all the stimulation experiments performed at discrete pressure increments mode. As the fluid pressure increases in discrete steps, the pump displacement rate increases. Once the fracture is initiated, the conductivity of the whole rock system dynamically increases which leads to an increasing leakoff rate of the fracturing fluids. It is observed that tests with H_2O injection in HDR stimulation strategy have much lower breakdown pressure (9.53-11.72MPa) than all other stimulation strategies. For the CO_2 in HDR stimulation strategy, shown in the blue curve in **Fig. 5**c, the breakdown pressure is 13.52 MPa or 17.80 MPa. While for CO_2/H_2O and CO_2/PAA stimulation strategies, the breakdown pressure is between 18.48 MPa and 18.53 MPa.

The pressures and pump displacement rate data of three stimulation strategies involving CO_2, CO_2/H_2O, and CO_2/PAA are plotted in **Fig. 5**c and d. The results show that at each pressure stage, the leakoff rate of CO_2 is different. The stimulation strategy of CO_2 in HDR resulted in the highest leakoff rate among the three tests. This

is explained by the fact that for CO_2 in HDR stimulation experiment, there is no liquid phase in the rock matrix. Thus, the effective permeability of CO_2 is higher than that of CO_2/H_2O and CO_2/PAA stimulations. For the CO_2/PAA and CO_2/H_2O stimulation strategy tests with discrete pressure increments steps, the leakoff rates at each pressure stage are similar. Once the pump pressure approaches the breakdown pressure, the CO_2 pump displacement rate increases as a function of time due to fracture initiation and propagation.

3.7. *Pump pressure and pump displacement rate history of fracturing fluids deployed in constant pump displacement rate injection mode*

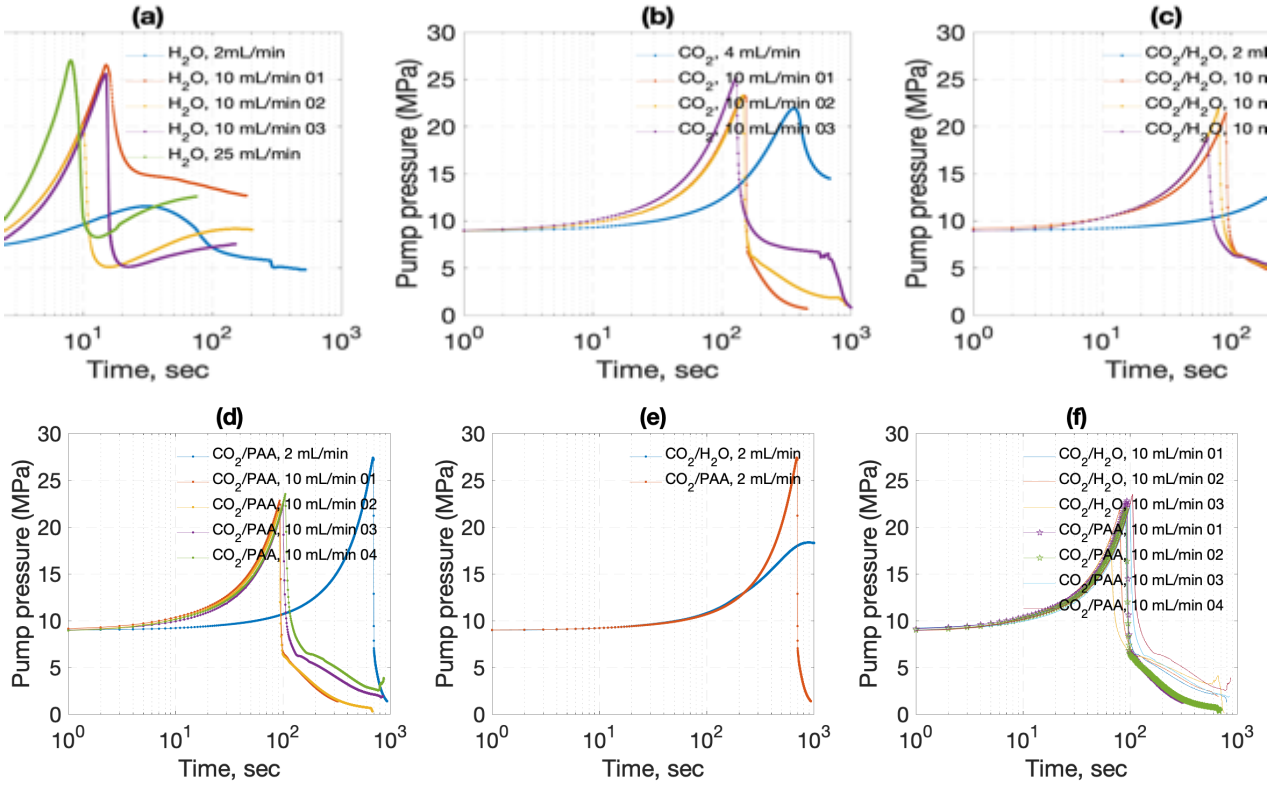

Fig. 6. Pump pressure history plots of all four stimulation strategies in constant pump displacement rate mode (a) H_2O in HDR, Q=2 or 10 mL/min; (b) CO_2 in HDR, Q=4 or 10 mL/min; (c) CO_2/H_2O, Q=2 or 10 mL/min; (d) CO_2/PAA, Q=2 or10 mL/min. (e) CO_2/H_2O and CO_2/PAA, Q=2 mL/min; (f) CO_2/H_2O and CO_2/PAA, Q=10 mL/min. All stimulation tests were conducted at 200°C.

Fig. 6 shows pump pressure history plots with all four stimulation strategies/fluids performed in constant pump displacement rate mode. **Fig. 6**a shows that H_2O stimulation generates fractures at significantly higher breakdown pressure at high pump displacement rates (10mL/min and 25 mL/min).

Fig. 6b shows results with the second stimulation strategy, CO_2 injected in HDR. Fracturing test performed at 4mL/min shows that the rock is fractured with a slow fracture propagation process (dark blue plot), at a relatively low breakdown pressure, and attaining a fracture with the lowest conductivity (0.7-1.5 μm^3). However, when the pump displacement rate of CO_2 in HDR is increased to 10mL/min, the rock is fractured significantly faster (red, orange, and purple plots in **Fig. 6**b) and attaining fractures with higher, though markedly variable, conductivity values. For the first of these tests (red plot), the breakdown pressure was 23.27 MPa (3375 psi) while for the second test (orange plot) it was 23.28 MPa (3376psi), and for the third test (purple plot) the breakdown pressure was 25.13MPa (3645psi). However, once the fracture initiates, the first two tests show a notable difference for CO_2 transport in the rock with fracture propagation. From the pressure response plots, the first two curves (red and yellow plots) deviate from each other once the pressure of the wellbore is around 6.21 MPa (900 psi) and this pressure value is just below the minimum principal stress of 7.58 MPa (1100 psi). This suggests that above this point, i.e., when the fracture is created, there is a positive net pressure, and the two fractures have similar

hydraulic properties. However, once the fractures are closed (at a negative net pressure or pressure below the minimum principal stress), the two fractures behave differently. The first stimulation test with CO_2 in HDR (red plot) shows a considerably sharper pressure decline curve below 6.21 MPa (900 psi) which indicates a significantly larger fracture compared to the fracture obtained in the second stimulation test given the fact that the pump displacement rates of CO_2 at the pump are identical in both tests (10 mL/min).

The conductivity measured for the largest fracture is around 160.6-341.1 μm^3 (red plot, first stimulation test with CO_2 in HDR at 10 mL/min) while for the second test performed under identical conditions the fracture conductivity is around 10.8-23.1 μm^3. For the third CO_2 fracturing in HDR, a much smoother pressure decline curve was observed, and the fracturing conductivity was only 2.0-4.2 μm^3. The reason why these three-fracturing tests show similar breakdown pressure, but very different conductivity is still unclear. One of the possible explanations could be associated with differences in rock heterogeneity or even minute natural fractures that could exist in the rock matrix systems which would affect the fracture initiation and propagation process.

Fig. 6c and d show results for CO_2/H_2O and CO_2/PAA stimulation strategies/fluids, respectively under high and low pump displacement rate conditions. Results show CO_2/PAA can fracture the rock at both low and high pump displacement rate injection while CO_2/H_2O can only fracture the rock at high pump displacement rate injection of CO_2. A comparison of stimulation at low pump displacement rate is shown in **Fig. 6**e. These tests were carried out with a CO_2 pump displacement rate of 2 mL/min in rock partially saturated with water or 1wt% aqueous PAA (1/3 of TPV). For the fracturing test with CO_2/H_2O, the rock is not fractured due to the leakoff rate accommodating the entire injected pump displacement rate of CO_2. The pressure reaches a plateau at a constant pump displacement rate of 2 mL/min. However, for a fracturing test performed with CO_2/PAA stimulation fluid, the pressure curve separates from that of the CO_2/H_2O stimulation test at approximately 250 seconds and at a pressure of approximately 15.17 MPa (2200 psi) as shown in **Fig. 6**e.

The curve separation could be caused by i) in-situ crosslinking reaction between CO_2 and PAA with a resulting viscosity increase and ii) volume expansion-induced saturation increases of aqueous phase. For the CO_2 and water two-phase saturated rock, the relative permeability of the CO_2 phase (Jian et al., 2019) based on Corey's model is expressed as shown in Eq. (1), thus the increased saturation of aqueous phase could cause a reduction of relative permeability for the CO_2 phase. Therefore, when the superficial velocity of the CO_2 phase is constant, the pressure gradient will increase according to Darcy's law as shown in Eq (2).

$$k_{rg} = k_{rg}^{0} * \left(\frac{1-S_w-S_{wc}}{1-S_{grw}-S_{wc}}\right)^{n_g} \quad (1)$$

Where k_{rg}^{0} is the endpoint relative permeability of gas; S_w is the water saturation; S_g is the CO_2 saturation; S_{wc} is the connate water saturation; S_{grw} is the residual CO_2 saturation to water; n_g is the exponent coefficient of CO_2 phase in Corey's relative permeability model.

$$\mu_g = -\frac{k_{rock}*k_{rg}}{u_g} * \nabla P \quad (2)$$

Where μ_g is the viscosity of the CO_2 phase; k_{rock} is the permeability of rock; k_{rg} is the relative permeability of CO_2 phase; ∇P is the pressure gradient across the rock; u_g is the superficial velocity of CO_2 phase.

For high pump displacement rate (10 mL/min) stimulation tests, the two pressure decline curves of the CO_2/PAA (green and purple line with star markers) after rock breakdown are sharper than any of the CO_2/H_2O curves (**Fig. 6**f). These two tests generate fractures with significantly higher conductivity values than the rest of the tests according to Table 1, and another two of the CO_2/PAA tests generate fractures with comparable conductivity

with CO_2/H_2O. These results, together with the fact that high conductivity values are obtained independently of injection rates, show that PAA/CO_2 represents an excellent stimulation fluid alternative for EGS.

3.8. *Mass consumption of CO_2 and water*

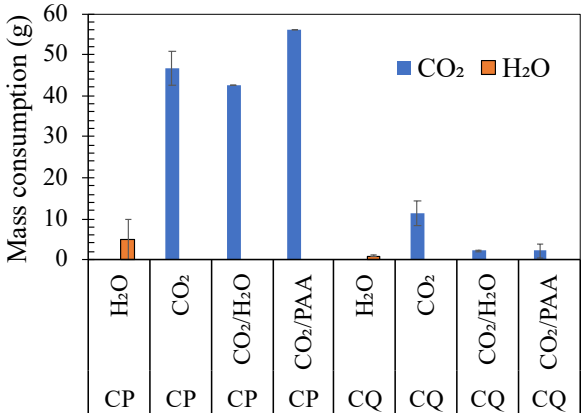

Fig. 7 Mass consumption of CO_2 and water for each fracturing test (CP means discrete pressure increment and CQ means constant pump displacement rate)

Fluid mass consumption during stimulation operations is an important factor at the time of selecting a fluid for EGS stimulation. The mass of fluid injected in each test was calculated from the time the fluid is injected at constant pump displacement rate or at incremental constant pressure steps to the time when the breakdown pressure is reached. **Fig. 7** shows that for different fracturing tests, CO_2 injected in rock partially saturated with aqueous PAA (CO_2/PAA) uses significantly lower CO_2 than CO_2 injection in HDR. For example, for the test at discrete pressure increments mode (denoted as CP), the mass consumption of water or CO_2 is high due to the leakoff at each pressure step. This mass consumption is highly dependent on the time held at each pressure step. For constant pump displacement rate fracturing (denoted as CQ), CO_2 fracturing consumes significantly more CO_2 than CO_2/H_2O or CO_2/PAA. The CO_2 consumption for CO_2/H_2O or CO_2/PAA in constant pump displacement rate mode was similar.

3.9. Simulation of fluid transport with different fracturing fluids

Two classical breakdown criteria have been used extensively for the formation of longitudinal fractures: The first one is called Hubert-Willis (H-W) expression:

$$P_b = 3\sigma_h - \sigma_H + T - P_p \tag{4}$$

and the second one is called Haimson-Fairhurst (H-F) criterion:

$$P_b = \frac{3\sigma_h - \sigma_H + T - 2\eta P_p}{2(1-\eta)} \tag{5}$$

Where P_b is the rock breakdown pressure; σ_h is the least compressive horizontal stress; σ_H is the greatest compressive horizontal stress; T is the rock tensile strength; P_p is the pore pressure and η is the poroelastic parameter in the range of 0 to 0.5.

(Detournay and Carbonell, 1997) have shown that the two criteria can be united into one in the context of poroelasticity, with the H-W criterion being used for rapid pressurizations and low permeability formations, and the H-F criterion being used for slow pressurizations and high permeability formations. All else being equal, the case of slower pressurization and higher permeability is expected to lead to lower breakdown pressures, which is consistent with the results in (Lu et al., 2020; Song et al., 2019). Note that the experimental result shown below are not for longitudinal fractures, and hence these two criteria are not directly applicable, but the same general trends would be expected since the underlying physics are how stress changes with pore pressure diffusion and are not specific to the wellbore geometry. For this sake, nonisothermal multiphase flow simulations were performed using STOMP (White et al., 2012; White and Oostrom, 2003) to estimate the pressure distribution within the rock matrix before fracture initiation and rock breakdown (i.e. excluding fracture mechanics). The details of the rock model are shown in **Fig. 8**. The three-dimensional model was constructed with quarter symmetry through the wellbore. The pump was connected to the wellbore through tubing with ¼ in diameter. The rock surfaces are at constant temperature and connected to the atmosphere which is a typical Dirichlet boundary condition. The pump is displacing with a constant volumetric rate. Van Genuchten capillary pressure relationship (Morel-Seytoux et al., 1996) with Webb extension (Webb, 2000) and the Corey relative permeability curves (Jian et al., 2020a) are used for the modeling. Additional details described in the supplemental material.

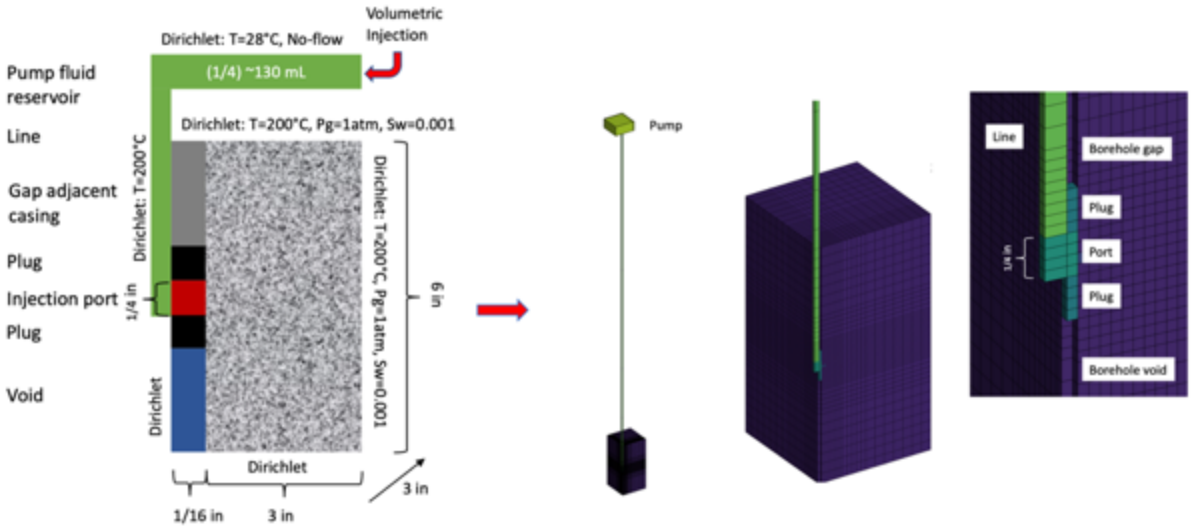

Fig. 8 Model rock system for simulations

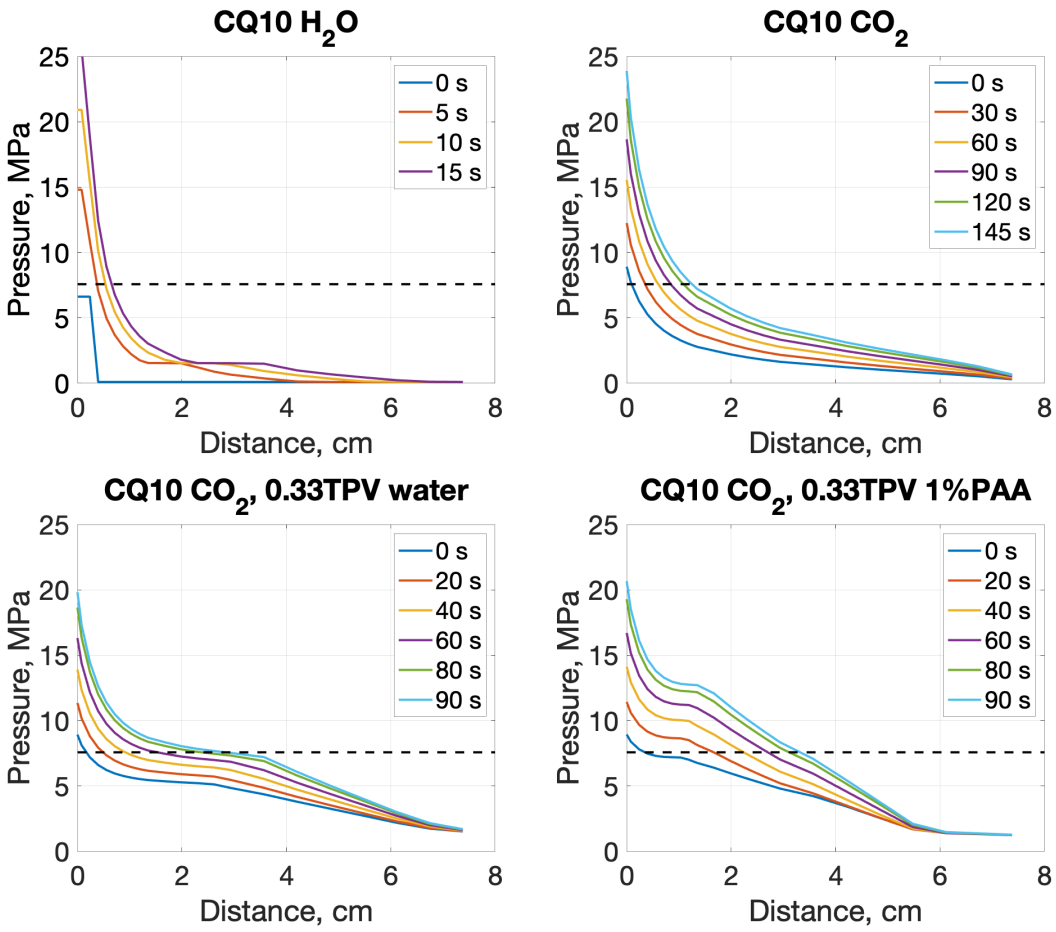

Fig. 9. Simulated pressure distribution curve from injection port to the rock surface

The four injection strategies in constant pump displacement rate mode (Q=10 mL/min) were simulated and the pressure from the wellbore to the rock surface is plotted as shown in **Fig. 9**. The simulated pressurized length where the pore pressure exceeds the minimum principal stress and the breakdown pressure estimated using the H-W criteria is shown in **Table 2**, along with the experimentally determined breakdown pressures. For H_2O fracturing in HDR, the average breakdown pressure is approximately 24.1 MPa. The distance from the wellbore to the rock surface where the pore pressure exceeds the minimum principal stress is 0.66 cm. For CO_2 fracturing in HDR, CO_2 was allowed to leak off at approximately 9 MPa for approximately 240 seconds, after which CO_2 was injected at 10 mL/min. The distance from the wellbore to the rock surface where the pore pressure exceeds the minimum principal stress is approximately 1.24 cm at the breakdown **(Fig. 9b).**

For fracturing experiments where CO_2 is injected in rock partially saturated with water (CO_2/H_2O), water was injected at 6.9-8.8 MPa for 1190 seconds (11 mL, or approximately 33% of the estimated pore volume), then allowed CO_2 to leak off at 9 MPa for approximately 360 seconds. CO_2 was then injected at 10 mL/min. The zone where the pore pressure exceeds the minimum principal stress is approximately 2.79 cm at the breakdown.

For fracturing experiments using CO_2/PAA, a 1wt% PAA aqueous solution was first injected at approximately 6.9-8.8 MPa for approximately 1190 seconds (11.3 mL or approximately 33% of the pore volume). Then, CO_2 was allowed to leak off at 9 MPa for approximately 360 seconds followed by injecting CO_2 at 10 mL/min. To account for the viscosity increase associated with the crosslinking reaction between PAA and CO_2, in the numerical simulations the PAA aqueous solution was simulated with a viscosity 100 times higher than water.

The distance (from the wellbore to the rock surface) where the pore pressure exceeds the minimum principal stress is approximately 3.30 cm at the breakdown **(Fig. 9d**).

The simulation results (**Fig. 9**) also show that when the formation is pre-saturated with CO_2-reacted PAA, the region of elevated pore pressure caused by subsequent CO_2 injection is more spatially concentrated compared to cases with only water pre-saturation. This appears to be the result of the elevated viscosity of the cross-linked CO_2-PAA, which reduces the propagation of pore pressure resulting in a broader region with elevated pore pressure. This may be responsible for the elevated fracture conductivity observed with this fluid, since a broader pressurized region would have the opportunity to generate a more complex fracture that retains more conductivity when closed.

Another effect that is known to influence breakdown is the wellbore compressibility (Lecampion et al., 2017). Larger wellbore compressibility is known to cause larger breakdown pressures. If this mechanism were responsible for the elevated breakdown pressure in the CO_2 tests, this would imply that the fracture was initiated at a pressure comparable to the water tests, but that breakdown did not occur because the flow rate into the initiated fracture was significantly smaller than our injection rate. Therefore, as we continued pumping the pressure continued to rise until the combination of higher pressures and time cause the fracture to grow. The fracture will continue to grow until it could accommodate all the injected pump displacement rate-which is the definition of breakdown. However, from the previous breakdown pressure statistical analysis reported in **Fig. 4**, CO_2 and water don't show a significant difference for breakdown pressure at 95% confidence level. Furthermore, the breakdown pressure in all of our constant injection rate fracturing tests are close, and higher breakdown pressures can be, in general, achieved with higher pump displacement rate injection during pumping.

Table 2 Correlation between breakdown pressure and simulated pressurized length

	Average experimental Pb (MPa)	95% confidence interval of Pb (MPa)	Simulation Pb (MPa)	Simulation pressurized length (cm)
H_2O	23.9	[16.5, 34.6]	26.0	0.66
CO_2	24.0	[21.8, 26.5]	24.4	1.24
CO_2/H_2O	20.6	[16.8, 25.4]	20.2	2.79
CO_2/PAA	22.3	[21.3, 23.5]	21.5	3.30

3.10. *Fracture analysis of rock thin sections*

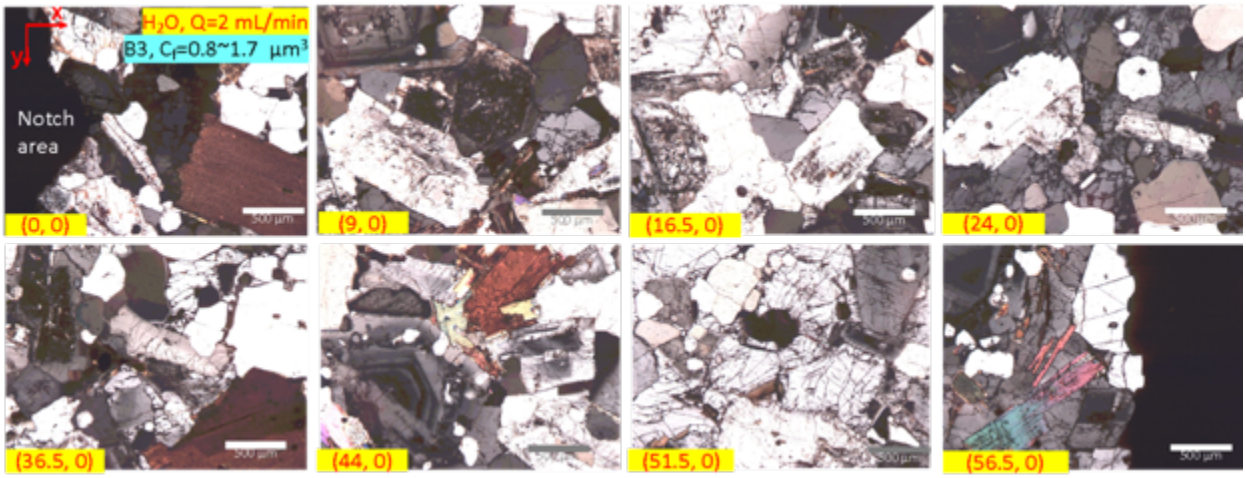

(a)

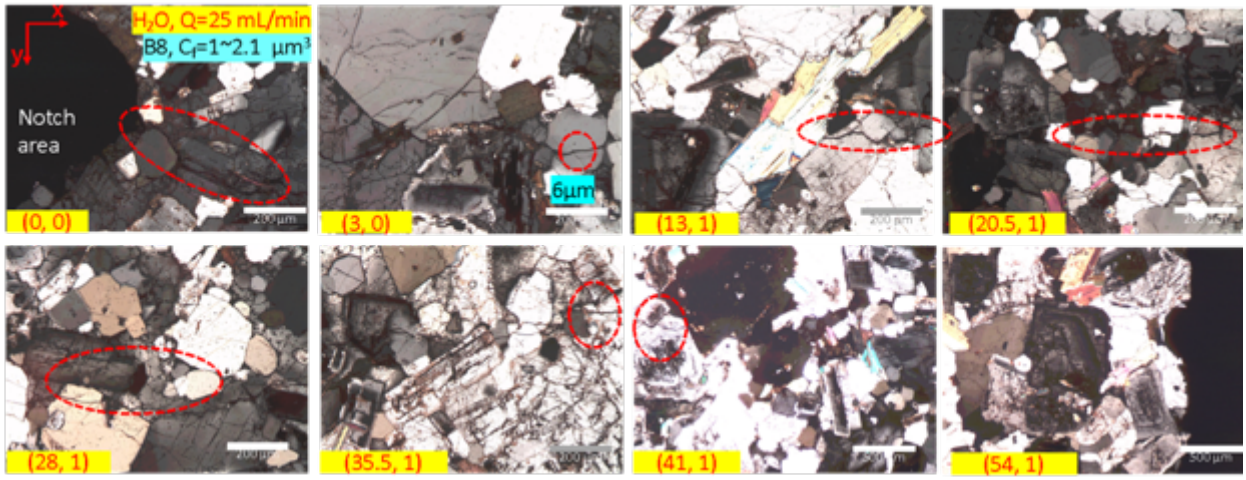

(b)

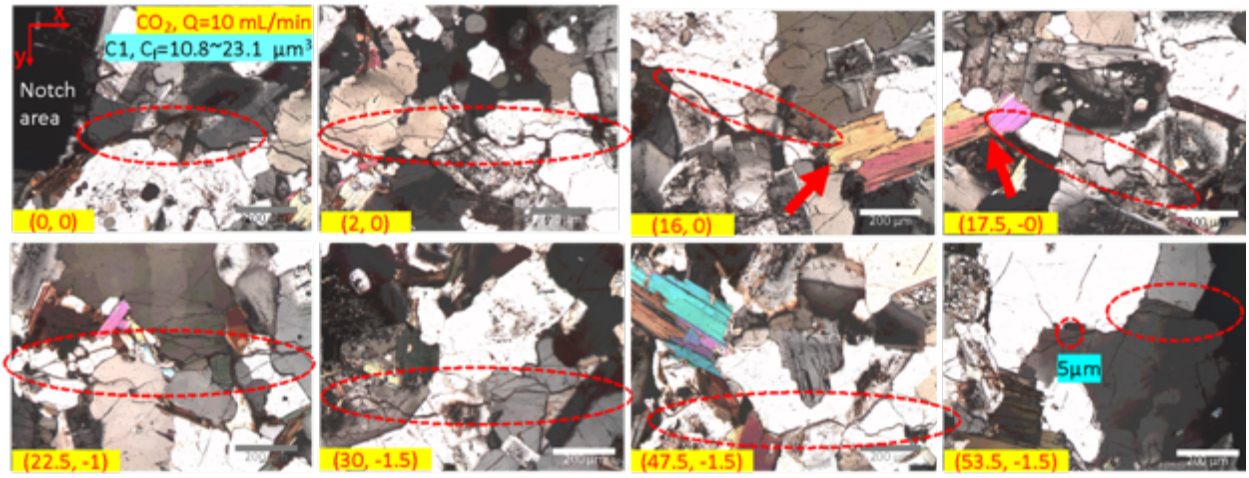
CO2, Q=10 mL/min
C1, Cf=10.8~23.1 μm3
Notch area
(0, 0)
(2, 0)
(16, 0)
(17.5, -0)
(22.5, -1)
(30, -1.5)
(47.5, -1.5)
5μm
(53.5, -1.5)

(c)

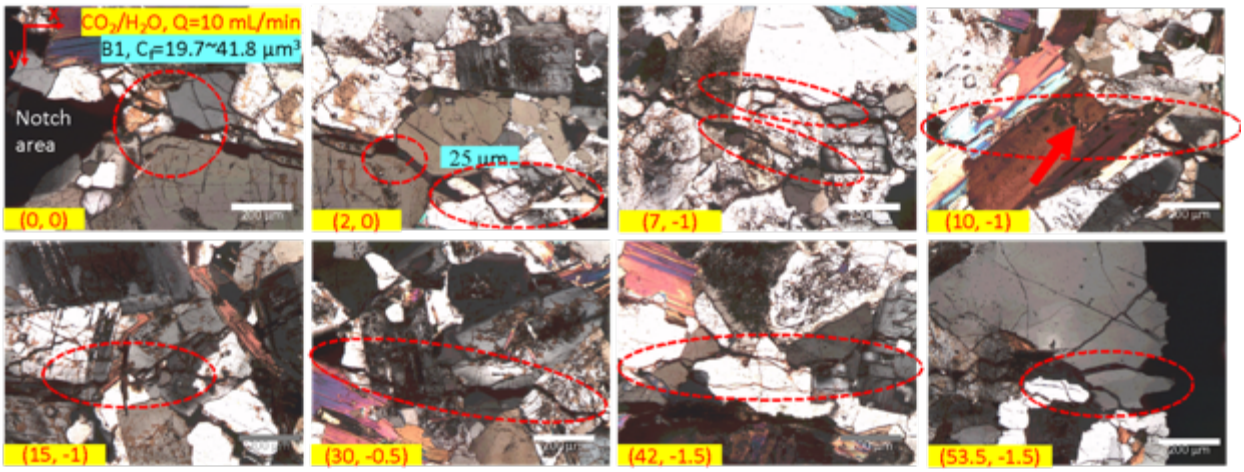
CO2/H2O, Q=10 mL/min
B1, Cf=19.7~41.8 μm3
Notch area
(0, 0)
25 μm
(2, 0)
(7, -1)
(10, -1)
(15, -1)
(30, -0.5)
(42, -1.5)
(53.5, -1.5)

(d)

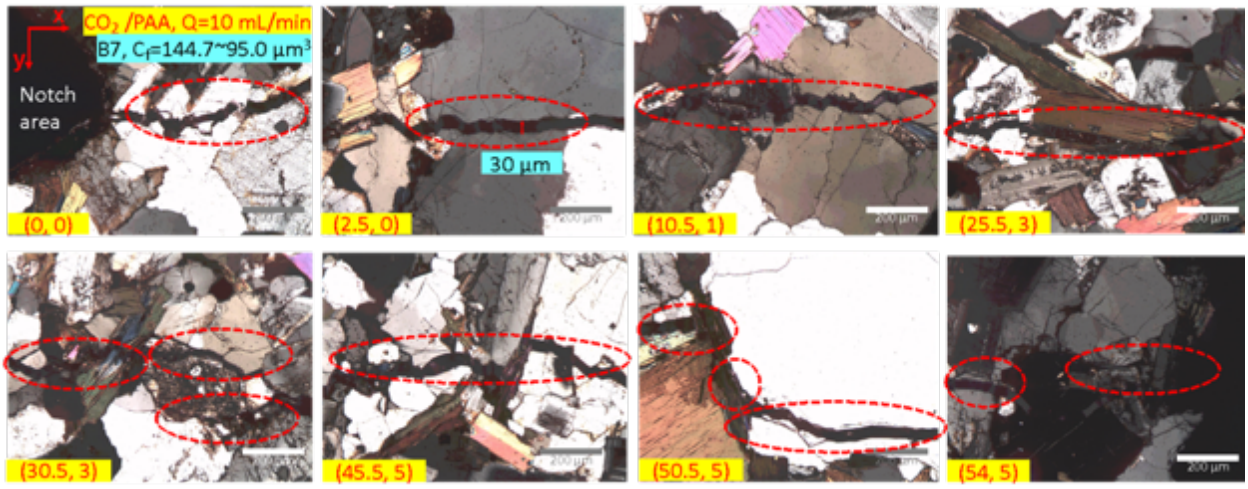
CO2 /PAA, Q=10 mL/min
B7, Cf=144.7~95.0 μm3
Notch area
(0, 0)
30 μm
(2.5, 0)
(10.5, 1)
(25.5, 3)
(30.5, 3)
(45.5, 5)
(50.5, 5)
(54, 5)

(e)

Fig. 10. Thin section analysis of rocks for different fracturing fluids (a) H_2O, Q=2 mL/min; (b) H_2O in HDR, Q=25 mL/min; (c) CO_2 in HDR, Q=10 mL/min; (d) CO_2/H_2O, Q=10mL/min; (e) CO_2/PAA, Q=10mL/min. Color code by stains of thin section: K-Feldspar Stain(yellow); Plagioclase Stain(orange-red); Calcite Stain(pink-red); Iron Stain(blue); Others(quartz): white or grey. The first picture in the top left of each group of eight micrographs (**Fig. 10**a to e) includes the notch. The coordinates for the picture with a notch (origin of the fracture) is denoted as (0,0). From the origin (notch), x and y coordinates change with the "x" direction (axis) corresponding to the fracture propagation direction, and the "y" axis corresponding to the direction of minimum principal stress. The distance unit is mm.

Fig. 10a and b show optical micrographs of thin sections of rocks for two rock samples fractured with water injected in HDR at low and high injection rates. For the rock fractured with low pump displacement rate (2mL/min) water injection, there is no observable fracture formed. For the rock fractured with high pump displacement rate (25 mL/min) water injection, there are fracture bands formed and penetrate to the rock, but the fracture propagation creased at a certain depth from the wellbore to the rock surface direction. The dead-end of the fracture front is shown in the micrograph labeled (54,1) in **Fig. 10**b. This might be due to the water/vapor phase transition under 200 °C after which the fluid pore pressure in the fracture equals water vapor pressure, then not sufficient pressure exists for driving the fracture to the rock surface.

As observed in the thin section of CO_2-based fracturing strategies (**Fig. 10**c to e), the fracture propagation seems to have difficulty passing through plagioclase grains (orange color and tabular). The propagation is bypassing the plagioclase grains. In some cases, particularly with the narrower aperture fractures, the fracture seems to disappear at the plagioclase grains. There is evidence for such small fractures that unfractured ligaments (Ghamgosar and Erarslan, 2016; Labuz et al., 1987) can exist and connect two halves of a fracture. For example, the micrograph labeled (17.5,0) and (16,0) micrographs for CO_2 in HDR at Q=10mL/min (**Fig. 10**c) show how the fracture disappears at a K-feldspar and plagioclase grain (see arrows inside yellow and orange-red circumference). A plausible explanation could be that the fracture grows around the grains. It is clear though that the fracture's aperture is reduced at/around these grains. Similarly, in micrograph labeled (10, -1) in the CO_2/H_2O (Q=10 mL/min) case in **Fig. 10**d, the fracture passes through/around the plagioclase grain and is then filled with a white precipitate within the plagioclase grain (see arrows inside orange-red circumference).
In contrast, micrographs taken on thin sections of rock fractured with CO_2/PAA (Q=10mL/min) show a completely different landscape. Micrograph (2.5,0) (**Fig. 10**e), for example, shows on the right-hand side a plagioclase grain where the fracture cuts through the grain and also makes a parallel path around it. What we speculate occurred is that when the fracture tip propagates in the beginning, it goes around the tougher material because it lacks the energy/aperture to cut through it. Then, after the fracture extends more its aperture increases and new fractures grow in a more straight-line path through the tougher (plagioclase grain) material. A similar example could be the case of micrograph (30.5, 3) for CO_2/PAA (Q=10mL/min), though the color of the grain in question is blue purple with only hints of orange (maybe biotite).
(Jeong et al., 2017) also reported fractures growing in straight lines through quartz grains but only following cleavage planes in plagioclase and K-felspars. This could be largely associated with a viscosity effect. Higher viscosity fluids tend to produce larger fracture apertures. From this analysis it can be concluded that CO_2/PAA fluid system attain fractures with the largest, self-propped, apertures in agreement with the consistently high fracture conductivity values measured post-stimulation and independently of injection pump displacement rate.

4. SUMMARY

Four fracturing fluids (water, CO_2, CO_2/water, CO_2/PAA), were evaluated in ½-foot side cubic granite samples at 200 °C and under geothermal relevant stress conditions with different injection modes (discrete pressure increments or constant pump displacement rate regimes).

1) *For CO_2-based stimulation fluids, i.e., CO_2 in HDR, CO_2/H_2O, and CO_2/PAA, the fracture conductivity is larger than that of water independently of injection mode (discrete pressure increments steps or constant pump displacement rate)*. For the injection strategy consisting of injecting water in HDR, the conductivity is generally less than 2 μm^3 (radial flow) even when fracturing at very high pump displacement rates (25 mL/min). These findings are consistent with other results published in the literature, for both shale and granite at room temperature (Song et al., 2019).

2) *The pressurization rate does not significantly affect fracture conductivity when fracturing with water but is a key factor for generating fractures with high conductivity in CO_2-based fluids.* Rapid pressurization rate (>6.89 MPa/min (1000 psi/min)) of CO_2-based fluids is beneficial for generating fractures with higher conductivity (>10 μm^3). However, when the pressurization rate of CO_2 is lower than 0.69 MPa/min (100 psi/min), the hydraulic conductivity of the fracture (2-10 μm^3) is only slightly higher than that of fractures generated by water injection (<2 μm^3). The exception is the PAA/CO_2 fluid system.

3) *Injection of water or aqueous PAA to partially saturate the rock before CO_2 injection (stimulation strategies CO_2/H_2O and CO_2/PAA) is beneficial to reduce the leakoff rate of CO_2 fracturing test and thus aids to pressure build-up.* The leakoff rate of CO_2 can be significantly reduced using PAA as observed in the constant pump displacement rate fracturing process, and this can be explained by the fact that the CO_2-triggered crosslinking reaction of PAA and associated volume expansion can cause an increase in both viscosity and aqueous phase saturation, thus decreasing the mobility of the CO_2 phase in the porous matrix. As a result, CO_2 can build up pressure faster and create larger fractures as compared to CO_2/H_2O stimulation fluid and with a significantly lower injected mass. Furthermore, CO_2 not only builds up pressure faster but also builds a larger pressure envelope with pressure values above the minimum principal stress.

4) *CO_2/PAA fracturing fluid system was found to consistently generate fractures with the highest conductivity values and independently of injection pump displacement rate.* Breakdown pressures were similar for CO_2 stimulation in HDR and CO_2/PAA fluid systems under identical injection pump displacement rates. CO_2/PAA offers the following three additional advantages; i) it requires a significantly less (1/6) mass of CO_2 (0-2.3g vs 4-12.8 g)), ii) the fracture conductivity is independent of injection pump displacement rate, and 3) the reversible viscosity (B. Jung et al., 2015) increase is beneficial to transport proppants when they become available for enhanced geothermal systems. The microscopy images of rock thin sections also show significantly higher dominant (self-propped) fracture apertures when using CO_2/PAA fluid system than when using the other fluid systems.

ACKNOWLEDGEMENTS

Funding provided by the Department of Energy's Geothermal Technology Office. PNNL is operated by Battelle for the U.S. DOE under Contract DE-AC06-76RLO 1830.

NOMENCLATURE

∇P	Pressure gradient across the rock
k_{rg}	Relative permeability of gas
k_{rg}^0	Endpoint relative permeability of gas
S_w	Water saturation
S_g	Gas saturation
S_{wc}	Connate water saturation
S_{grw}	Residual gas saturation to water
n_g	Exponent coefficient of gas in Corey's model

REFERENCES

Bee, A., Massart, R., Neveu, S., 1995. Synthesis of very fine maghemite particles. Journal of Magnetism and Magnetic Materials 149, 6–9. https://doi.org/10.1016/0304-8853(95)00317-7

B. Jung, H., C. Carroll, K., Kabilan, S., J. Heldebrant, D., Hoyt, D., Zhong, L., Varga, T., Stephens, S., Adams, L., Bonneville, A., Kuprat, A., A. Fernandez, C., 2015. Stimuli-responsive/rheoreversible hydraulic fracturing fluids as a greener alternative to support geothermal and fossil energy production. Green Chemistry 17, 2799–2812. https://doi.org/10.1039/C4GC01917B

Bradford, J., Ohren, M., Osborn, W.L., McLennan, J., Moore, J., Podgorney, R., 2014. Thermal stimulation and injectivity testing at Raft River, ID EGS site, in: Proceedings of 39th Workshop on Geothermal Reservoir Engineering, Stanford, CA, USA.

Chabora, E., Zemach, E., Spielman, P., Drakos, P., Hickman, S., Lutz, S., Boyle, K., Falconer, A., Robertson-Tait, A., Davatzes, N.C., 2012. Hydraulic stimulation of well 27-15, Desert Peak geothermal field, Nevada, USA, in: Proceedings of Thirty-Seventh Workshop on Geothermal Reservoir Engineering, Stanford University, Stanford.

Detournay, E., Carbonell, R., 1997. Fracture-mechanics analysis of the breakdown process in minifracture or leakoff test. SPE production & facilities 12, 195–199.

Fernandez, C.A., Gupta, V., Dai, G.L., Kuprat, A.P., Bonneville, A., Appriou, D., Horner, J.A., Martin, P.F., Burghardt, J.A., 2019. Insights into a Greener Stimuli-Responsive Fracturing Fluid for Geothermal Energy Recovery. ACS Sustainable Chem. Eng. 7, 19660–19668. https://doi.org/10.1021/acssuschemeng.9b04802

Ghamgosar, M., Erarslan, N., 2016. Experimental and Numerical Studies on Development of Fracture Process Zone (FPZ) in Rocks under Cyclic and Static Loadings. Rock Mech Rock Eng 49, 893–908. https://doi.org/10.1007/s00603-015-0793-z

Ghassemi, A., 2012. A review of some rock mechanics issues in geothermal reservoir development. Geotechnical and Geological Engineering 30, 647–664.

Heath, D.F., 1967. Normal or Log-normal: Appropriate Distributions. Nature 213, 1159–1160. https://doi.org/10.1038/2131159a0

Hu, L., Ghassemi, A., Pritchett, J., Garg, S., 2020. Characterization of laboratory-scale hydraulic fracturing for EGS. Geothermics 83, 101706. https://doi.org/10.1016/j.geothermics.2019.07.004

Isaka, B.L.A., Ranjith, P.G., Rathnaweera, T.D., Wanniarachchi, W.A.M., Kumari, W.G.P., Haque, A., 2019. Testing the frackability of granite using supercritical carbon dioxide: Insights into geothermal energy systems. Journal of CO2 Utilization 34, 180–197. https://doi.org/10.1016/j.jcou.2019.06.009

Jeong, S.S., Nakamura, K., Yoshioka, S., Obara, Y., Kataoka, M., 2017. Fracture Toughness of Granite Measured Using Micro to Macro Scale Specimens. Procedia Engineering, ISRM European Rock Mechanics Symposium EUROCK 2017 191, 761–767. https://doi.org/10.1016/j.proeng.2017.05.242

Jian, G., Alcorn, Z., Zhang, L., Puerto, M.C., Soroush, S., Graue, A., Biswal, S.L., Hirasaki, G.J., 2020a. Evaluation of a Nonionic Surfactant Foam for CO2 Mobility Control in a Heterogeneous Carbonate Reservoir. SPE Journal 25, 3481–3493. https://doi.org/10.2118/203822-PA

Jian, G., Fernandez, C.A., Burghardt, J., Bonneville, A., Gupta, V., Garrison, G., 2020b. Alternative, Less Water-Intensive, Fracturing Fluids for Enhanced Geothermal Systems. Presented at the 54th U.S. Rock Mechanics/Geomechanics Symposium, American Rock Mechanics Association.

Jian, G., Zhang, L., Da, C., Puerto, M., Johnston, K.P., Biswal, S.L., Hirasaki, G.J., 2019. Evaluating the Transport Behavior of CO2 Foam in the Presence of Crude Oil under High-Temperature and High-Salinity Conditions for Carbonate Reservoirs. Energy Fuels 33, 6038–6047. https://doi.org/10.1021/acs.energyfuels.9b00667

Kamali, A., Ghassemi, A., 2018. Analysis of injection-induced shear slip and fracture propagation in geothermal reservoir stimulation. Geothermics 76, 93–105. https://doi.org/10.1016/j.geothermics.2018.07.002

Labuz, J.F., Shah, S.P., Dowding, C.H., 1987. The fracture process zone in granite: evidence and effect. International Journal of Rock Mechanics and Mining Sciences & Geomechanics Abstracts 24, 235–246. https://doi.org/10.1016/0148-9062(87)90178-1

Lecampion, B., Desroches, J., Jeffrey, R.G., Bunger, A.P., 2017. Experiments versus theory for the initiation and propagation of radial hydraulic fractures in low-permeability materials. Journal of Geophysical Research: Solid Earth 122, 1239–1263. https://doi.org/10.1002/2016JB013183

Lu, G., Gordeliy, E., Prioul, R., Aidagulov, G., Uwaifo, E.C., Ou, Q., Bunger, A.P., 2020. Time-Dependent Hydraulic Fracture Initiation. Journal of Geophysical Research: Solid Earth 125, e2019JB018797. https://doi.org/10.1029/2019JB018797

Lu, J., Ghassemi, A., 2019. Estimating natural fracture orientations using geomechanics based stochastic analysis of microseismicity related to reservoir stimulation. Geothermics 79, 129–139. https://doi.org/10.1016/j.geothermics.2019.01.003

Lund, J.W., 2011. Direct utilization of geothermal energy 2010 worldwide review. Geothermics 40, 159–180.

Lund, J.W., Boyd, T.L., 2016. Direct utilization of geothermal energy 2015 worldwide review. Geothermics 60, 66–93. https://doi.org/10.1016/j.geothermics.2015.11.004

Lund, J.W., Freeston, D.H., 2001. World-wide direct uses of geothermal energy 2000. Geothermics 30, 29–68. https://doi.org/10.1016/S0375-6505(00)00044-4

Lund, J.W., Freeston, D.H., Boyd, T.L., 2005. Direct application of geothermal energy: 2005 Worldwide review. Geothermics 34, 691–727. https://doi.org/10.1016/j.geothermics.2005.09.003

Morel-Seytoux, H.J., Meyer, P.D., Nachabe, M., Tourna, J., Genuchten, M.T. van, Lenhard, R.J., 1996. Parameter Equivalence for the Brooks-Corey and Van Genuchten Soil Characteristics: Preserving the Effective Capillary Drive. Water Resources Research 32, 1251–1258. https://doi.org/10.1029/96WR00069

Shao, H., Kabilan, S., Stephens, S., Suresh, N., Beck, A.N., Varga, T., Martin, P.F., Kuprat, A., Jung, H.B., Um, W., Bonneville, A., Heldebrant, D.J., Carroll, K.C., Moore, J., Fernandez, C.A., 2015. Environmentally friendly, rheoreversible, hydraulic-fracturing fluids for enhanced geothermal systems. Geothermics 58, 22–31. https://doi.org/10.1016/j.geothermics.2015.07.010

Song, X., Guo, Y., Zhang, J., Sun, N., Shen, G., Chang, X., Yu, W., Tang, Z., Chen, W., Wei, W., Wang, L., Zhou, Jun, Li, Xiao, Li, Xiaofeng, Zhou, Jinhui, Xue, Z., 2019. Fracturing with Carbon Dioxide: From Microscopic Mechanism to Reservoir Application. Joule 3, 1913–1926. https://doi.org/10.1016/j.joule.2019.05.004

Webb, S.W., 2000. A simple extension of two-phase characteristic curves to include the dry region. Water Resources Research 36, 1425–1430. https://doi.org/10.1029/2000WR900057

White, M.D., Bacon, D.H., McGrail, B.P., Watson, D.J., White, S.K., Zhang, Z.F., 2012. STOMP Subsurface Transport Over Multiple Phases: STOMP-CO2 and STOMP-CO2e Guide: Version 1.0 (No. PNNL-21268). Pacific Northwest National Lab. (PNNL), Richland, WA (United States). https://doi.org/10.2172/1059044

White, M.D., Oostrom, M., 2003. STOMP Subsurface Transport Over Multiple Phases Version 3.0 User's Guide (No. PNNL-14286). Pacific Northwest National Lab., Richland, WA (US).

Ye, Z., Ghassemi, A., 2019. Injection-Induced Propagation and Coalescence of Preexisting Fractures in Granite Under Triaxial Stress. Journal of Geophysical Research: Solid Earth 124, 7806–7821. https://doi.org/10.1029/2019JB017400

Ye, Z., Ghassemi, A., 2018. Injection-Induced Shear Slip and Permeability Enhancement in Granite Fractures. Journal of Geophysical Research: Solid Earth 123, 9009–9032. https://doi.org/10.1029/2018JB016045

Zhou, D., Zhang, G., Prasad, M., Wang, P., 2019. The effects of temperature on supercritical CO2 induced fracture: An experimental study. Fuel 247, 126–134. https://doi.org/10.1016/j.fuel.2019.02.099

Effect of Initial Water Saturation on the Performance of Fracturing Fluids with and Without Polyallylamine under Simulated EGS Conditions

ABSTRACT

Objectives/Scope: StimuFrac (US Patents 9,873,828 B2 and 9,447,315 B2), a CO_2-reactive polymer aqueous solution [polyallylamine (PAA) 1wt% in water] combined with CO_2, can be used as a potentially less water-intensive fracturing fluid for enhanced geothermal systems (EGS). Our previous results show that in hot dry rock (HDR), PAA/CO_2 fracturing fluids outperformed other fluids such as water, CO_2, and CO_2/water in generating large fractures with less fluid consumed. The objective of this work is to investigate the effect of initial water saturation on the performance of StimuFrac by conducting hydraulic fracturing tests with ½ foot cubic rock samples held under representative EGS stress/temperature conditions and by using cyclic injection strategies (under constant injection rate). The resulting fracture hydraulic conductivities, breakdown pressures, and volumes of fluids required are compared.

Methods/Procedures/Process: To simulate geothermal reservoir conditions, in all tests, the rock sample was held under triaxial confinement and at 200 °C, and different volumes of water were initially injected into the rock sample before any fracturing processes were initiated. For the single-cycle PAA (or water) alternating CO_2 (PAG or WAG) injection fracturing experiments, one complete cycle consisted of two steps: (1) injecting a PAA slug (or water slug) followed by (2) injecting CO_2 to initiate and propagate the fracture. For experiments involving multiple injection cycles, the CO_2 injection pressure is increased until it peaks and begins to decline (indicating fracture initiation at this moment), and then continued being injected for another 30 seconds to propagate the fracture. Then, these two-step cycles [injection of PAA (or water) followed by CO_2 injection (up to 2-4 mL/min)] are repeated.

Applications/Significance/Novelty: The results of this study suggest that water saturation significantly affects the fracturing fluid transmission into the rock pore space, thus affecting fracture initiation and propagation. In this study, fracturing tests via a single injection cycle or multiple injection cycles were performed. Splitting the rock samples in half after testing reveals that fracture propagation is significantly limited under high water saturation conditions (three-day initial water injection) compared to stimulation experiments performed in hot dry rock. The fractures propagate less than 1/3 of the distance from the wellbore to the outer rock surface, and in some cases, no fracture is generated. This may be caused by leak-off dominating the fracturing process and the fluid injection rate is insufficient to overcome leak-off, even under high injection rate conditions. Additionally, CO_2 could be leaking off into the wellbore annulus and this may be making it more difficult to generate sufficiently high-pressure gradients away from the near-wellbore region. Under low water saturation conditions (dry rock or after 1-day initial water injection), PAA/CO_2 consistently generated significantly larger fractures compared with the other fluids. CO_2 generated large fractures only in the hot dry rock and only when using high injection rates, though data variability is high.

1. INTRODUCTION

Enhanced geothermal systems (EGS) (Lund, 2011; Lund et al., 2005; Lund and Boyd, 2016; Lund and Freeston, 2001) are aimed at recovering thermal energy from geothermal reservoir rocks which have intrinsically ultralow permeability. During a typical production process, working fluids, e.g. water, are pumped into the reservoir and heated. The harnessing of thermal energy takes place by the heated working fluids produced in the production well. The production rate is highly dependent on the characteristics of the natural fracture networks that exist in the geothermal reservoir. Highly permeable fracture networks where working fluids can attain flow rates between 1 and 5 m^3/hour are required for economically viable geothermal energy production.

Hydraulic fracturing is recognized as an effective way for enhancing reservoir permeability, increasing injectivity of the working fluid, and ultimately increasing heat exchange efficiency in enhanced geothermal systems. Many of the currently used stimulating technologies are inherited from oil and gas stimulation operations, such as water fracturing (WF), hydraulic proppant fracturing (HPF), and hybrid fracturing (HF) with the latter using cross-linked gels, linear gels, and slick water fluids. WF is, however, the typical choice since the other technologies are mainly designed for low-temperature applications (e.g., below 120 °C). For example, viscosifier such as xanthan gum or high molecular weight partially hydrolyzed polyacrylamide (HPAM) used as proppant carriers in shale fracturing processes cannot withstand temperatures above 150°C (Jung et al., 2015). In addition, stimulation operations in EGS typically require ten times more water (Bradford et al., 2014; Chabora et al., 2012) than in tight oil reservoir fracturing operations.

Therefore, less water-intensive or water-free fracturing processes need to be developed to make Enhanced Geothermal Systems more environmentally amenable and cost-effective.

CO_2 fracturing as a water-free fracturing technique has attracted lots of attention in recent years. Li et al. (Li et al., 2019) conducted hydraulic fracturing tests with different fluids including gel, slick water, liquid CO_2, and supercritical CO_2 ($scCO_2$) with slickwater. Results show that $scCO_2$ can form fracture networks with multiple bedding planes opened. While for water and gel fracturing, only incomplete propagated transverse fractures are formed. Song et al.(Song et al., 2019) found that CO_2 fracturing can generate complex fractures with lower breakdown pressure than water fracturing or thickened-water fracturing. They explained this is related to the viscosity of the fluid. They also reported that for CO_2 fracturing under different pressurization rates (from 0.5 to 2.0 MPa/min), the breakdown pressure increases with the CO_2 pressurization rate. Isaka et al.(Isaka et al., 2019) report that the breakdown pressure decreases linearly with experimental temperatures using CO_2 as the fracturing fluid. All of the above tests show that when CO_2 is used as a waterless fracturing fluid, it can generate complex and large fractures under wide experimental conditions. However, due to the low viscosity of CO_2 compared with water, it takes significantly longer times for CO_2 to break down the rock due to high leak-off.

CO_2 foam fracturing(Khan et al., 2022) has been investigated to address the high leak-off problem of CO_2 and foam can also increase the proppant carrying ability to deep reservoirs. However, due to the thermodynamically unstable nature of foams, foam stability (Thakore et al., 2021) under high-temperature EGS conditions remains a big challenge for fracturing applications. StimuFrac^{TM}, an aqueous polymer solution of polyallylamine (PAA) combined with CO_2, has been previously reported by our group as an alternative, promising, and less water-intensive fracturing fluid for enhanced geothermal systems (EGS). The PAA-CO_2 crosslinking reactions, volume expansion, and viscosity increase at high temperatures (Fernandez et al., 2019; Jung et al., 2015; Shao et al., 2015) enable the generation of large fractures in hot dry rock systems (Jian et al., 2021). However, the effect of water saturation in the rock is still unclear for the PAA/CO_2 fracturing fluid system. Initial water saturation could be an important parameter governing fracturing processes. First, most geothermal reservoirs are partially (e.g., The Geysers geothermal field in California with water saturation ranging from 8% to 25% (Withjack and Durham, 2001)) or fully saturated with water. Second, water saturation should affect the fracturing fluid's transport since the relative permeability of the fluid is changed. Last, but not least, water saturation can affect the mechanical properties of the rock. In the case of StimuFrac fluid, water in the reservoir may also affect the PAA-CO_2 reaction through dilution. Thus, understanding the water saturation effect on fracturing performance is important for designing fracturing fluid injection strategies for a given geothermal reservoir.

A recent study (Zhuang et al., 2020a) shows that fractures tend to propagate in wider areas for highly water-saturated samples. These results were described to be due to two reasons. One, is the decrease in fracture toughness of the rock with water saturation and the other reason is associated to high water pressure exerted inside the cracks. However, the study doesn't report on the hydraulic conductivity differences before and after fracturing in dry and water-saturated rock samples. Our previous results show that in hot dry rock, PAA/CO_2 outperformed other fracturing fluids such as CO_2, water, or water/CO_2. However, questions remain regarding how the PAA/CO_2 fracturing fluid system performs within rock systems with different initial water saturation. In this work, the effect of initial water saturation was investigated and found to have a significant and complex impact on the fracturing performance of different fracturing fluids. Fracturing in high water saturation conditions (samples initially flooded with water for three days) can lead to very low conductivity fractures for all fluids systems tested. Under hot dry rock or intermediate water saturation (samples initially flooded with water for one day) conditions, PAA/CO_2 generates more conductive fractures than water, CO_2, or water/CO_2. This is particularly the case for single-cycle polymer-alternating-gas (PAG) injections.

2. MATERIALS AND METHODS

2.1 Materials

A borehole is drilled longitudinally through each sample and the granite sample is placed in the heated triaxial load cell (Jian et al., 2021). A representative illustration of the rock sample and the wellbore structure is shown in **Figure 2**. The diameter of the borehole is 5/16 -inch on the top half of the sample and is smaller (1/4 -inch) on the bottom half. This design is aimed to stop the 1/4 -inch casing halfway onto the borehole. The schematic of the casing for fluids injection is shown in **Figure 3**. The casing (with the injection ports) is fixed in the wellbore with packers (by a pair of Ø=5/16" O-rings) located above and below the notch on the wall of the wellbore. The O-rings isolate the injection port from the rest of the borehole and allow for (injection-fluid) pressure buildup during fracturing tests. During the tests, CO_2 is injected into the casing through an inner concentric line with 1/16" tubing outside diameter and 0.014" wall

thickness as shown in the diagram on the left of **Figure 2**, while water or PAA solution is injected through the annulus of the outer tubing with 1/4" tubing outside diameter will wall thickness of 0.035".

The stress field applied by the loading frame is the same in all tests: $\sigma_{T-B}/\sigma_{N-S}/\sigma_{W-E}$ =1,100/1,400/1,400 psi (7.58/9.65/9.65 MPa) which means the stress in the direction perpendicular to the top and bottom of the rock sample is the minimum principal stress. This directs the fracture orientation in the lateral direction as shown in **Figure 6**. All experiments were performed under identical temperature (200 ºC) conditions. The mass consumption of aqueous PAA, water, and CO_2 during the fracturing process is calculated beginning from the injection of fracturing fluids until the breakdown pressure is reached (water injected to increase the initial saturation is excluded from the mass calculations). For all the tests, the dead volume has been deducted when we perform the data analysis.

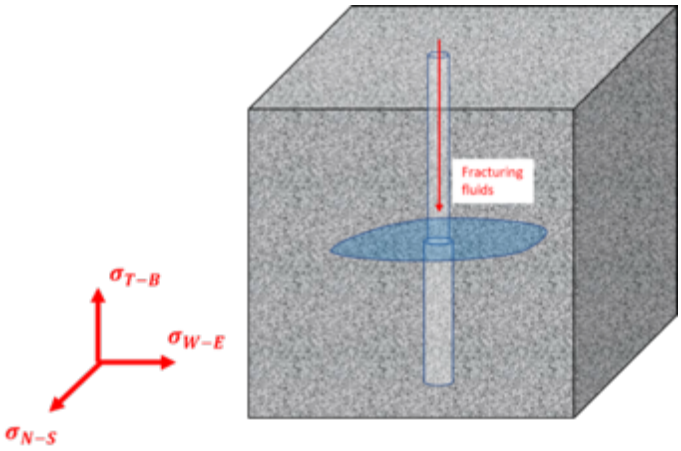

Figure 2 schematic of rock and fracturing fluids

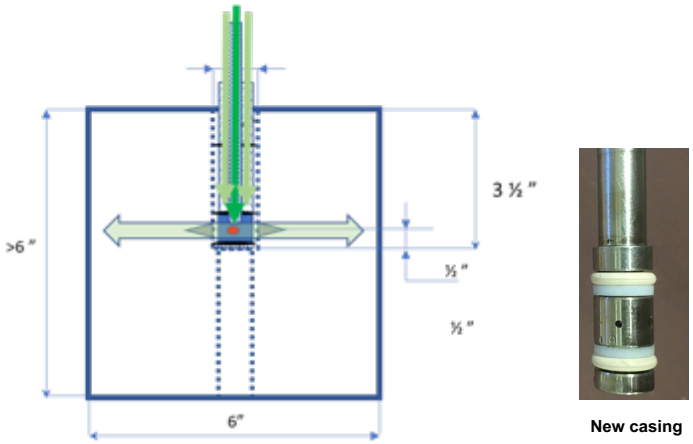

Figure 3 Schematic of the casing and zonal isolation and casing in the high-temperature true triaxial fracturing system

2.2 Injection strategy

There are 33 tests covered in this study which are shown in Error! Reference source not found.. They can be categorized into six fluids/methods as shown in **Figure 4**. Below are the six fluids/methods and the corresponding tests.

Fluid/Method 1: water injection (tests 1-8),
Fluid/Method 2: CO_2 injection (tests 9-16),
Fluid/Method 3: single cycle (WAG01) water/CO_2 injection (tests 13-20),
Fluid/Method 4: single cycle (PAG01) PAA/CO_2 injection (tests 21-30),
Fluid/Method 5: multiple cycles (WAGn) water/CO_2 injection (test 31),
Fluid/Method 6: multiple cycles (PAGn) PAA/CO_2 injection (tests 32 and 33).
Method 1-4 was conducted at different water saturation conditions.

Method 1 and 2 are two commonly used fracturing fluids for hydraulic fracturing processes. Methods 3-6 are designed to investigate the role of PAA in the fracturing processes. Methods 3-4 are single-cycle fracturing processes while methods 5-6 are multiple-cycle injection using water/CO_2 or polymer/CO_2. This is designed to see whether the multiple-cycle injection is beneficial for the fracturing processes. Previous studies show that CO_2 fracturing (Song et al., 2019) can generate large and more complex fractures than water fracturing. However, to the best of our knowledge, there is no study that reports how the alternative injection can affect the fracturing process in different water saturation conditions and under EGS pressure and temperature conditions.

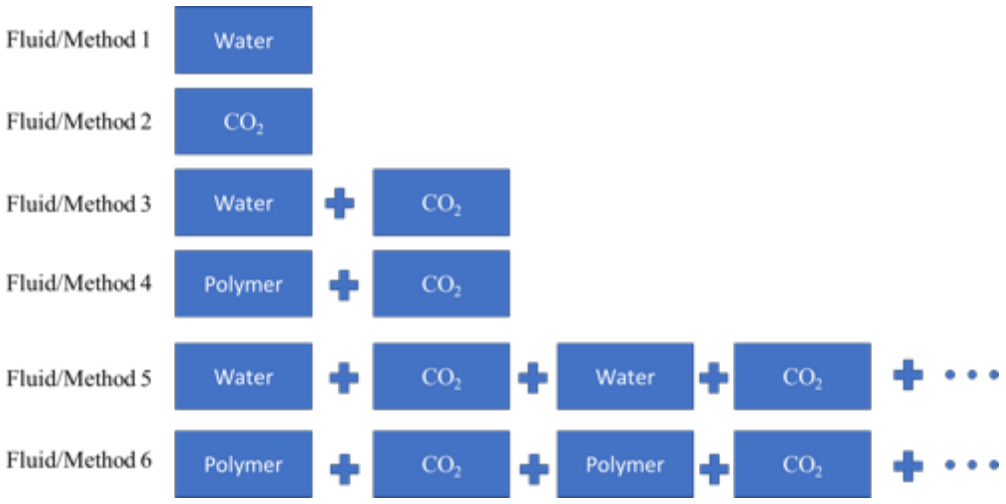

Figure 4 Six injected fracturing fluid/methods

The experiments were conducted under three different initial water conditions: dry or nearly dry rock, rock subjected to water injection for one day, and rock subjected to water injection for three days to simulate different water saturation in EGS reservoirs. The fluid injection rates selected are based on the leak-off rate to ensure that the flow rate is higher than the leak-off rate at a specific pressure value. Then, the injected fracturing fluid can be pressurized to overcome the breakdown pressure of the rock to initiate and propagate the fracture. For field fracturing processes, the actual injection rate needs to be determined according to the wellbore size, zonal isolation volumes, and other reservoir properties such as permeability.

Table 1 Fracturing results in dry and pre-waterflooded rock

Test	Rock ID	Mode/Rate	Fracturing fluid/Method	Water injected into pre-saturated rock (S_{wi})	P_b	C_f	First fixed PAA (or water) slug injected after Swi	Additional PAA (or water) injected	CO_2 usage for fracturing
		(mL/min)		(mL)	(psi)	(μm^3)	(mL)	(mL)	(g)
1	B3*	$C_Q = 2$	Dry-H_2O	0	1675	0.8	0	0.9	0
2	D4*	$C_Q = 10$	Dry-H_2O	0	3849	0.4	0	1.3	0
3	D5*	$C_Q = 10$	Dry-H_2O	0	2925	1.4	0	0.8	0
4	D6*	$C_Q = 10$	Dry-H_2O	0	3708	1.4	0	1.2	0
5	B8*	$C_Q = 25$	Dry-H_2O	0	3917	1.0	0	0.6	0

6	E5	$C_Q = 3\ to\ 12$	H_2O(3day)-H_2O	8242	2131	0.6	0	20.8	0
7	E9	$C_Q = 25$	H_2O(3day)-H_2O	7524	3289	1.0	0	1.4	0
8	F7	$C_Q = 25$	H_2O(3day)-H_2O	13900	2943	1.0	0	2.5	0
9	B10*	$C_Q = 4$	Dry-CO_2	0	3183	0.7	0	0	14.5
10	B2*	$C_Q = 10$	Dry-CO_2	0	3375	160.6	0	0	12.8
11	C1*	$C_Q = 10$	Dry-CO_2	0	3376	10.8	0	0	8.3
12	C7*	$C_Q = 10$	Dry-CO_2	0	3645	2.0	0	0	9.5
13	G4	$C_Q = 25$	H_2O(1day)-CO_2	871	2660	7.5	0	0	<0.1
14	E7	$C_Q = 4\ to\ 20$	H_2O(3day)-CO_2	10702	1722	0.7	0	0	31.1
15	F1	$C_Q = 25$	H_2O(3day)-CO_2	13770	2423	0.4	0	0	10.9
16	F8	$C_Q = 25$	H_2O(3day)-CO_2	9768	2271	0.9	0	0	7.1
17	B1*	$C_Q = 2\ or\ 3$	Dry-WAG01	0	N/A	N/A	11.3	0	N/A
18	B1*	$C_Q = 10$	Dry-WAG01	0	3019	19.7	11.3	0	2.5
19	C8*	$C_Q = 10$	Dry-WAG01	0	3174	24.4	11.3	0	2.1
20	C9*	$C_Q = 10$	Dry-WAG01	0	2720	8.2	11.3	0	1.9
21	A10*	$C_Q = 2$	Dry-PAG01	0	3974	65.7	11.3	0	4.9
22	B7*	$C_Q = 10$	Dry-PAG01	0	3308	44.7	11.3	0	2.3
23	D3*	$C_Q = 10$	Dry-PAG01	0	3172	77.7	11.3	0	0.9
24	D7*	$C_Q = 10$	Dry-PAG01	0	3242	22.3	11.3	0	0.9
25	D8*	$C_Q = 10$	Dry-PAG01	0	3412	12.5	11.3	0	2.0
26	G3	$C_Q = 25$	H_2O(1day)-PAG01	934	3510	90.1	11.3	0	<0.1
27	E8	$C_Q = 4\ to\ 18$	H_2O(3day)-PAG01	9093	1971	0.2	11.3	0	11.5
28	F2	$C_Q = 25$	H_2O(3day)-PAG01	11044	2738	4.3	11.3	0	1.4
29	F9	$C_Q = 25$	H_2O(3day)-PAG01	9035	2724	0.6	11.3	0	5.2

30	G1	$C_Q = 25$	H_2O(3day)-PAG01	11274	2488	1.0	11.3	0	0.7
31	E4	$C_Q = 4$	H_2O(3day)-WAG09	9415	1537	0.7	11.3	16.2	76.9
32	E2	$C_Q = 0.4$ to 2	H_2O(3hour)-PAG17	85.3	2570	0.08	11.3	4.0	58.4
33	E3	$C_Q = 2$	H_2O(1day)-PAG25	718	4283	0.18	11.3	8.7	58.5

Notes: Rock ID columns with * symbols mean the data are cited from our previous published paper (Jian et al., 2021).

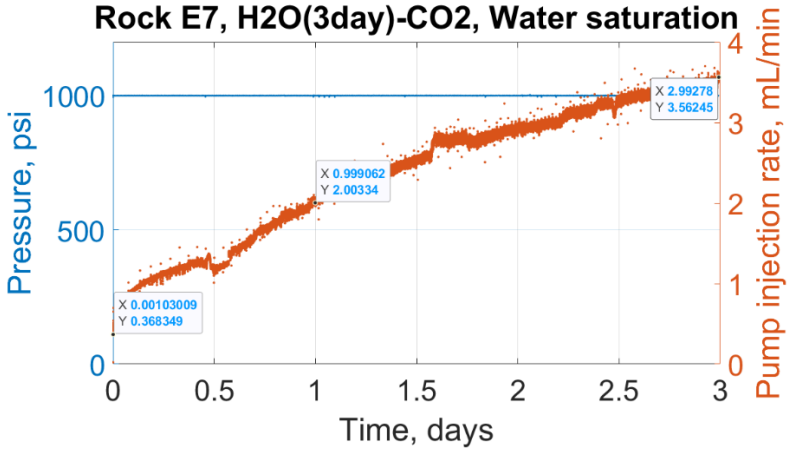

Figure 5 three days water saturation at constant pressure injection

During the initial water injection period, water was injected into the sample at 1,000 psi constant pump pressure (and then water, CO_2, water/CO_2, or PAA/CO_2 were used as fracturing fluids). A 3-day water saturation process is shown in **Figure 5**. The water leak-off rate at the beginning of injection is around 0.37 mL/min, after 1 day it is 2mL/min, and after 3 days it is 3.56 mL/min. Those leak-off rate changes as a function of time mean that the relative permeability of water increases with water saturation. Thus, by controlling the time of water injection, we can control the saturation of water in the rock. For experiments where water was the sole fracturing fluid, water was injected starting from 1,000 psi at a constant injection rate (tests 1-8 in **Table 1**). For experiments where CO_2 was the sole fracturing fluid, CO_2 was injected starting from 1,300 psi at a constant injection rate (tests 9-16 in **Table 1**). For single-cycle WAG experiments denoted as WAG01 in **Table 1**(WAG refers to water alternating CO_2) injection, water was always injected at 1,000 psi and CO_2 was injected starting from 1,300 psi with a constant injection rate (tests 13-20). For single-cycle PAG experiments denoted in **Table 1** as PAG01 (PAG refers to polymer aqueous solution (1% PAA) alternating CO_2) injection, a fixed volume of 11.3 mL of PAA was injected at 1,000 psi in the first cycle, followed by CO_2 injection at constant injection rate starting from 1,300 psi (tests 21-30).

For multiple cycles of WAG or PAG (tests 31-33), the procedure was as follows. In the first cycle, a fixed (11.3 mL or 1/3 total pore volume of rock sample) amount of water (or PAA) was injected followed by injecting CO_2 at a constant injection rate until a pressure peak is observed. Then, we continued injecting CO_2 for an additional 30-seconds. Next, from the second to last cycle, water (or PAA) was injected at constant pressure (1,000 psi) as follows. First, we switched from CO_2 back to water (or PAA) injection at constant pressure (1,000 psi). Since the pressure at the wellbore is originally higher than the pressure at the water (or PAA) pump (i.e., whatever pressure is reached after 30 seconds of CO_2 injection in the first cycle), the injection rate measured in the water (or PAA) pump is negative. Therefore, we waited until the injection rate in the water (or PAA) pump switched to positive values, and then from that point on we continued injecting at constant water (or PAA) pressure (1,000 psi) until an injection rate of zero mL/min (PAA) or significantly small values (water) was measured. Simultaneously, the isolated CO_2 pump pressure is set back to 1,300 psi in preparation for the next cycle injection. At this point, we close the valve connecting the water (or PAA) pump to the wellbore and switched back to CO_2 injection by opening the valve connecting the wellbore

to the CO_2 pump. Since the pressure at the CO_2 pump is 1,300 psi we waited (in constant pressure mode) for the pressure at the CO_2 pump to equilibrate with the wellbore pressure. Then, we switch the CO_2 pump to constant injection rate mode and inject CO_2 until a new pressure peak is reached followed by another 30 seconds of injection. These cycles of water (or PAA)/CO_2 repeat as shown in **Figure 10** and **Figure 11**. It should be noted that the dead volume of the tubing and the valves are determined before the tests, so the time when the fluid reaches the rock can be accurately timed.

Additional information on each test is shown in **Table 1**. The nomenclature used under the column "Fracturing fluid/Method" refers to the rock's initial condition, injection fluid, and the number of cycles. For example, test 33 is named H_2O(1 day)-PAG25. This means that there were 25 injection cycles with alternating PAA and CO_2 injections, and the rock was pre-flooded with water for one day. In the column of "Mode/Rate", C_Q means constant injection rate for the fracturing process. S_{wi} represents the initial water saturation of rock. P_b means breakdown pressure which is the maximum pressure recorded during the fracturing test and C_f is fracture conductivity after the fracturing tests are done.

To determine and compare the performance of each fracturing fluid or method, the quantification parameter used is the fracture conductivity and fluid's mass consumed during the fracturing processes. The fracture conductivity was measured at the same stress and temperature conditions but using oil. The conductivity of the rock can be calculated based on Eq. (1) and (2).

$$Q = \frac{2\pi * k_f * h * (P_e - P_w)}{\mu * ln\frac{R_e}{R_w}} \quad (1)$$

$$C_f = k_f \cdot h = \frac{Q * \mu * ln\frac{R_e}{R_w}}{2\pi * (P_e - P_w)} \quad (2)$$

where Q is the volumetric flow rate; P_e is the pressure of the formation; P_w is the pressure of the wellbore; R_e is the radius of the formation; R_w is the radius of the wellbore; μ is the viscosity of fluids; k_f is the lower limit of fracture permeability, h is the aperture of the fracture. The preferred fracturing fluids/process is the one that can generates highly conductive fractures while using the lowest volume .

2.3. Thin section analysis

Four thin sections were prepared from the split rock surfaces for the four-injection strategies: 1) Dry-WAG01; 2) Dry-PAG01; 3) H_2O(1 day)-CO_2 also called H_2O(1 day)-WAG01; 4) H_2O(1day)-PAG01. Zeiss PALM Laser Capture Dissection Microscope was used for thin section analysis. Images were collected at 5X magnification. Red fluorescent epoxy was used for vacuum/pressure impregnation. For the analysis of fractures with fluorescent dyes, the filter excitation is 572/25 and the emission is 629/62.

3. DISCUSSION

Fluid/Method 1: water injection (tests 1-8)

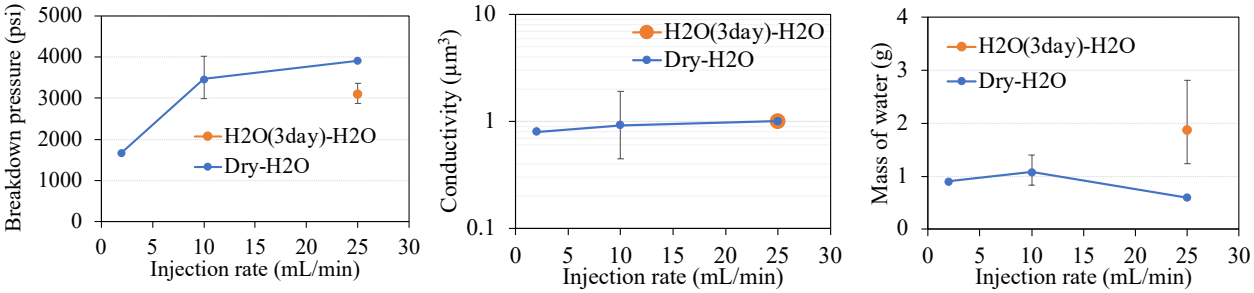

(a) (b) (c)

Figure 6: ***Average (a) breakdown pressure; (b) conductivity; (c) mass of water consumed for single water injection in dry and water-saturated rocks***

Tests 1 to 8 were conducted using water injection in the dry rock and rock pre-waterflooded for 3 days (as shown in **Table 1**). The average (a) breakdown pressure; (b) fracture conductivity; and (c) mass of water injected are shown in **Figure 6**.

The average breakdown pressure in dry rock increases from 1,675 psi to 3,917 psi with the injection rate increasing from 2 mL/min to 25 mL/min as shown in **Figure 6(a)**. This rate-dependent breakdown pressure may not reflect the pressure when the fracture is initiated since the fluid can still be further compressed when the fracture is not conductive enough. The average breakdown pressure in rock pre-water flooded for 3 days is around 3,116 psi, which is lower than that in the dry rock under the same condition. This indicates that the water saturation in the rock can reduce the breakdown pressure for the water fracturing process. Zhuang et al. (Zhuang et al., 2020b) reported a reduction in compressive and (in less extent) tensile strength of granite at high water saturation levels. Another factor affecting breakdown pressure is the extent of the zone of elevated pore pressure surrounding the borehole during pumping. The extend of this zone of elevated pore pressure increases with increased permeability of the rock matrix. Because water saturated rock has a higher relative permeability compared to unsaturated rock, there is expected to be a larger zone where the pore pressure exceeds the minimum principal stress and hence a lower breakdown pressure. For the average fracture conductivity, shown in **Figure 6(b)**, both fracturing tests in dry and pre-waterflooded rocks resulted in very low fracture conductivities. The average fracture conductivity is 0.8~1.1 μm^3 for dry rock comparable to 1.0 μm^3 for 3-day pre-water flooded rock. Hu et al.(Hu et al., 2020) reported an 80 times increase in conductivity after water fracturing stimulation. However, in our case, there is only a slight increase of conductivity which indicates that it is either a very small fracture formed, or the fracture is not a breakthrough fracture, i.e., from the wellbore to the rock surface. From the thin section analysis in our previous study (Jian et al., 2021), both very small fracture apertures and not a through fracture, account for the ultralow conductivity post-stimulation with water. In addition, low conductive fractures are attained under both, dry and high-water saturation conditions as shown in **Figure 6(b)**. Dilatant shear slip (Ye et al., 2017) is recognized as a dominant mechanism for the aperture increase of water fracturing in EGS systems. In this work, we found that the fracture propagation distance is another important factor affecting fracture aperture and conductivity. A fracture that does not breakthrough shows no obvious conductivity enhancement as shown in **Figure 6(b)**.

The average mass consumption of water is shown in **Figure 6(c)**; at 25 mL/min injection rate, the average water consumption is 2.0 g in rock pre-water flooded for 3 days while it is only 0.6g in dry rock. This indicates that high initial water saturation increases water usage, likely because of increased water relative permeability and thus greater water leak-off. On the other hand, in dry rock with nearly zero water saturation, the leak-off rate of water is low due to the low relative permeability.

Fluid/Method 2: CO_2 injection (tests 9-16)

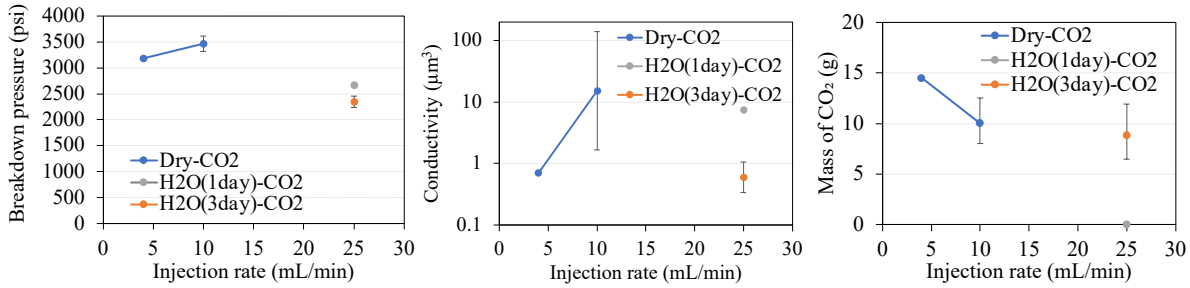

(a) (b) (c)

Figure 7: ***Average (a) breakdown pressure; (b) conductivity; (c) mass of CO_2 consumed for single CO_2 injection in dry and water-saturated rocks***

Tests 9 to 16 were conducted using CO_2 injection in dry and pre-waterflooded rock samples (as shown in **Table 1**). The average (a) breakdown pressure; (b) conductivity; (c) mass of CO_2 consumed are shown in **Figure 7**.

The average breakdown pressure (**Figure 7 (a)**) for dry rock changes from 3,183 psi to 3,465 psi when the injection rate changes from 4 mL/min to 10 mL/min. Lecampion and Song et al. (Lecampion et al., 2017; Song et al., 2019)

reported similar results where breakdown pressure with CO_2 increases at a higher pressurization rate (high injection rate of CO_2). For the breakdown pressure in 1-day and 3-day pre-waterflooded rock, the average breakdown pressure is 2,660 psi and 2,347 psi, which is much lower than in dry rock. This low breakdown pressure may be related to the high pore pressure in the rock matrix surrounding the borehole during pumping as observed by Ranjith et al., 2019. In their study, the team demonstrated that rocks with high permeability (siltstone) were fractured at lower breakdown pressure than low permeability shale rock particularly when fracturing with CO_2.

The average fracture conductivity (**Figure 7 (b)**) seems to increase with the injection rate in dry rock but the data variability is high at 10 mL/min. There is no clear trend on fracture conductivity when fracturing in dry rock, 1-day or 3-day pre-waterflooded rock though the data can't be compared because the injection flow rates are different to begin with. However, when injecting at 25 mL/min, the average fracture conductivity between 1-day and 3-day pre-waterflooded rock is reduced under higher water saturation conditions. This is important since CO_2 has shown better fracturing performance (Ranjith et al., 2019; Zhang et al., 2020) than water in regards to fracturing aperture. However, our results show that under high water saturation conditions, CO_2 fracturing fluid can only generate low conductive fractures as in the case of water as the fracturing fluid. This indicates that the aperture of the fracture propagation during propagation, as well as possibly the fracture length, are smaller in a water saturated rock than in dry rock. Then, under high water saturation conditions, the overall fracture conductivity is low compared to hot dry rock, with the injection rates and volumes used in this experiment.

The average mass consumption of CO_2 (**Figure 7 (c)**) decreases with the injection rate in dry rock. Comparing the results between 1-day and 3-day pre-waterflooded rock, the mass-consumed increases with higher water saturation conditions. This is because the water saturation in the rock is high above the irreducible water saturation conditions. Once the CO_2 is injected into the rock with high water saturation, a two-phase displacement occurs along with the fracturing process. A large amount of CO_2 will be introduced to the rock during this process. Thus, more CO_2 will be required for pressurization and fracturing to compensate for the CO_2 required for displacement. Furthermore, Gooya et al. demonstrated in a water-saturated porous media that when capillary equilibrium is established, CO_2 is safely trapped in the geologic medium but at higher temperatures, the dynamic capillary coefficient is higher, which increases the time (and mass of CO_2) required for reaching capillary equilibrium. This agrees with the results of this work for 3-day water pre-saturated rock. However, for the CO_2 fracturing in 1-day water-saturated rock, the reduced relative permeability of CO_2 dominates the fracturing process which limits the CO_2 transport from the wellbore to the rock. It is important to note that the above-described results could be also affected by the fact that a larger injection rate was used for tests in water-flooded rock (25 mL/min vs 4 mL/min and 10 mL/min) since no fracturing was observed at low injection rates.

Fluid/Method 3: single cycle (WAG01) water/CO_2 injection (tests 13-20)

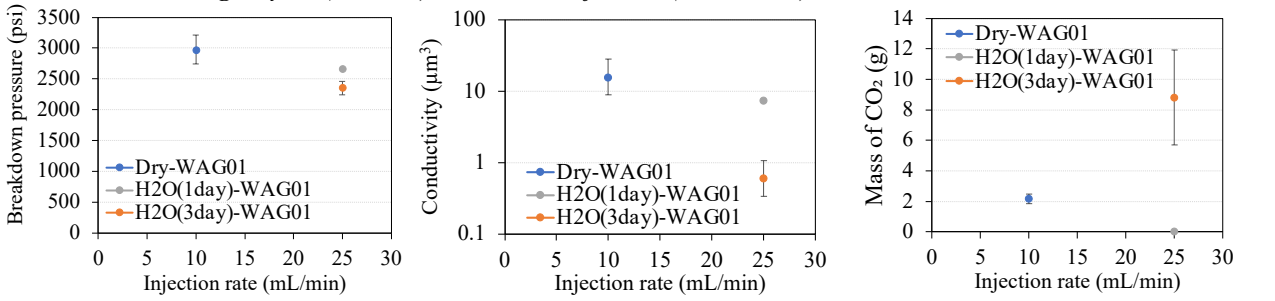

Figure 8: ***Average (a) breakdown pressure; (b) conductivity; (c) mass of CO_2 consumed for the single cycle (WAG01) in dry and water-saturated rocks***

Tests 13 to 20 were conducted using single cycle (WAG01) water/CO_2 injection in dry and pre-waterflooded rock samples (as shown in **Table 1**). It should be noted that test 13, which is H_2O(1day)-CO_2, is equivalent to H_2O(1day)-WAG01 and that tests 14-16, which are H_2O(3day)-CO_2, are equivalent to H_2O(3day)-WAG01. The reason is that the last 11.3 mL injection of water during the pre-flooding corresponds to the water injection in a single cycle of WAG. Therefore, tests 13-16 are used as H_2O(1 day)-WAG01 and H_2O(3 days)-WAG01 for comparison with Dry-WAG01

(which is one cycle WAG in dry rock). The average (a) breakdown pressure; (b) conductivity; (c) mass of CO_2 for single-cycle WAG injection in dry and water-saturated rock are shown in **Figure 8.**

The average breakdown pressure (**Figure 8(a)**) for dry rock is 2,971 psi when the CO_2 injection rate is 10 mL/min. In rock pre-waterflooded for 1 day and 3 days, the average breakdown pressure is lower (2,660 psi and 2,347psi) than in hot dry rock though the CO_2 injection rate used in pre-waterflooded rock samples is 25 mL/min. This lower breakdown pressure observed under high water saturation conditions could be the result of residual pore pressure from the water saturation portion of the experiment and/or the result of water weakening of the rock as previously described. The average fracture conductivity (**Figure 8(b)**) for dry rock averages 17.4 μm^3 while in 1-day and 3-days pre-waterflooded rock, the fracture conductivity is between 0.8-7.5 μm^3. This indicates that the resulting average fracture conductivity is reduced under higher water saturation conditions. We hypothesize that the lower fracture propagation pressures result in small fracture apertures during fracture propagation. The fracture propagation pressure is proportional to the fracture toughness which would be expected to be lower under saturated conditions than under dry conditions. Therefore, we anticipate lower fracture apertures since the fracture aperture during propagation is proportional to the propagation pressure. Then, the potential residual fracture aperture is reduced when the aperture during propagation is reduced.

The average mass consumption of CO_2 (**Figure 8(c)**) in dry rock is less than that in 3 days of pre-waterflooded rock. However, these experiments were performed under different CO_2 injection rates. Now, it was observed an increase in CO_2 mass consumption when fracturing in 3-day pre-waterflooded rock (6-12 g of CO_2) than in 1-day water pre-flooded rock (negligible volume measured) as shown in **Figure 8**(c). The reason for this significant difference was described in the previous section and is due to a two-phase displacement occurring along with the fracturing process and more CO_2 will be required for pressurization and fracturing to compensate for the CO_2 required for displacement.

Fluid/Method 4: single cycle (PAG01) PAA/CO_2 injection (tests 21-30)

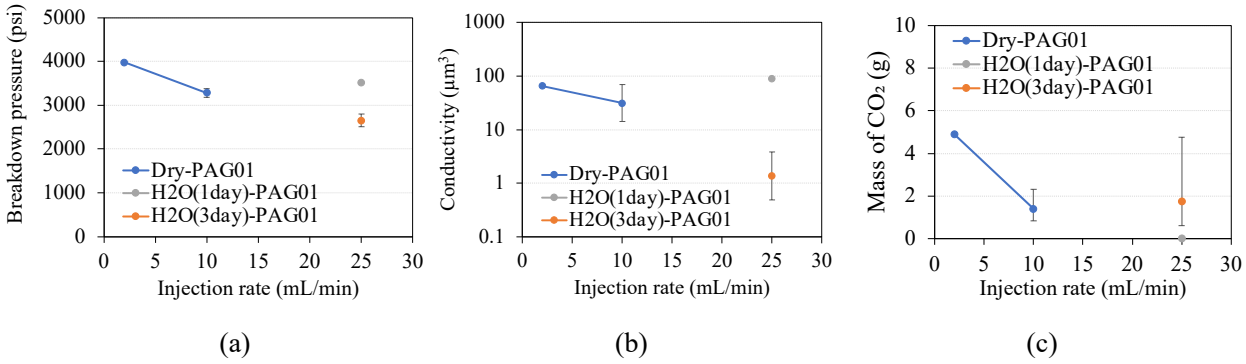

Figure 9: ***Average (a) breakdown pressure; (b) conductivity; (c) mass of CO_2 for the single cycle (PAG01) in dry and water-saturated rocks***

Tests 21 to 30 were conducted using single cycle (PAG01) PAA/CO_2 injection in dry and pre-waterflooded rock samples (as shown in **Table 1**). The average (a) breakdown pressure; (b) conductivity; (c) mass of CO_2 consumed for the single cycle (PAG01) PAA/CO_2 injection in dry and water-saturated rock are shown in **Figure 9.**

The breakdown pressure (**Figure 9(a)**) for dry rock averages 3,974 psi when the injection rate is 2 mL/min and 3,284 psi when the injection rate is 10 mL/min. For the breakdown pressure in 1-day and 3-day pre-waterflooded rock, the average breakdown pressure is 3,510 psi and 2,650 psi. This indicates that high water saturation may reduce the breakdown pressure when fracturing with PAG injection. This is consistent with all the above-mentioned results in rocks using CO_2, water, and WAG as the fracturing fluid because of the high pore pressure of water in combination with the water weakening of the rock as previously described.

The average fracture conductivity (**Figure 9(b)**) in dry rock is 65.7 μm^3 at 2 mL/min CO_2 injection rate and 39.3 μm^3 at 10mL/min CO_2 injection rate. In 1-day pre-waterflooded rock, the fracture conductivity is 90.1 μm^3, while in 3-day pre-waterflooded rock it is only 2.0 μm^3. Comparing these average fracture conductivity values to the values attained for H_2O/CO_2 at 25 mL/min injection rate, the PAA/CO_2 test provides significantly higher fracture conductivity than the H_2O/CO_2 test for the hot dry rock and 1-day pre-waterflooded rock samples (**Figure 8(b**) and **Figure 9(b))**. The

fracture conductivity results for the H_2O/CO_2 tests and PAA/CO_2 tests in 3-day pre-waterflooded rock samples were within the same order of magnitude. The low fracture conductivity attained when using alternating PAA/CO_2 under high water saturation (3 days water injection) is unexpected since the fracture conductivity using PAA/CO_2 under other water saturation conditions (nearly dry and 1-day water saturation) was one to two orders of magnitude higher. Nevertheless, we did not observe fracture breakthrough on the rock surface after the test with water, CO_2, and H_2O/CO_2 but did so (although with a fracture parallel to the wellbore) with PAA/CO_2. As described in the previous section, the results indicate that the resulting average fracture conductivity is reduced under higher water saturation conditions. We hypothesize that the lower fracture propagation pressures result in small fracture apertures during fracture propagation and, since the fracture propagation pressure is proportional to the fracture toughness (which is lower under saturated conditions than under dry conditions), then the potential residual fracture aperture is reduced when the aperture during propagation is reduced.

The average mass consumption of CO_2 (**Figure 9(c))**, is similar in tests with dry rock and 3-day pre-waterflooded rock. However, these experiments were performed under different CO_2 injection rates. The CO_2 mass-consumed for the 1-day pre-waterflooded rock was negligible (or close to the uncertainty of the pump) and significantly lower than the mass of CO_2 consumed for 3-day water preflooded rock under otherwise exact same test conditions (including CO_2 injection flow rates). The reason for high CO_2 consumption under high water saturation (3 days water injection) conditions was described in the previous sections and is associated to the fact that more CO_2 is required for the CO_2/water (or CO_2/PAA) displacement process during the fracturing process.

Fluid/Method 5&6: multiple cycle WAG (test 22) and multiple cycle PAG injections (tests 31-33)

Figure 10 shows the continuous pump pressure and pump injection rate information for the multiple-cycle WAG case (WAG09). The top and bottom plots are complementary to each other: the top figure shows the water injection information while the bottom figure shows the CO_2 injection information. The pre-waterflooding period is not shown here. The rate of saturating water injection after 3 days of injection is around 3.7 mL/min (with an initial rate of water injection of 0.35mL/min). For the fracturing process illustrated in **Figure 10**, water was injected at a constant pressure of 1,000 psi. Then, CO_2 was initially injected at 2 mL/min, during which the pressure increased by several psi and then decreased significantly to around 1,100 psi (shown with black dashed arrows). In the following cycles, CO_2 was injected at 4 mL/min, and it seemed that no fracture was formed since during each cycle the leak-off rate of water was decreasing to values significantly lower than the water leak-off rate values (3.7 mL/min) observed during the end of the 3-days water saturation process. In addition, if a fracture is initiated and propagated from the wellbore to the rock's external walls, the water injection rate (constant pressure conditions) should increase steadily. This was not observed in all the cycles. Nevertheless, **Figure 10** plots correspond to those of a typical WAG injection, where CO_2 injection pressure steadily increases due to the reduced total mobility associated with phase interference and CO_2 trapping. The final measured average rock conductivity is 0.7 μm^3, which is very low and indicates that there is no large effective fracture formed in this test.

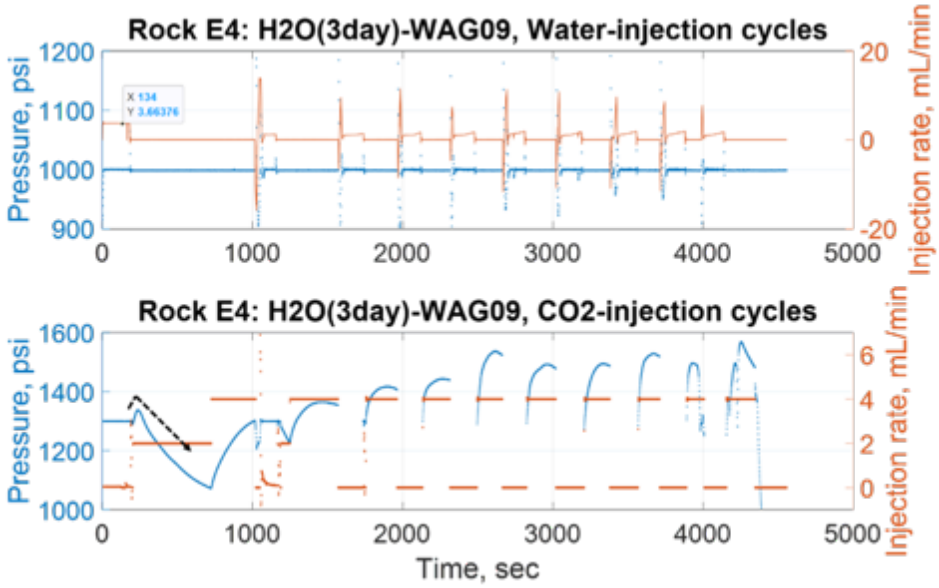

Figure 10: Nine cycles of WAG fracturing with H_2O-CO_2 in 3-day pre-waterflooded rock

Figure 11 shows the continuous pump pressure and pump injection rate information for the multiple-cycle PAA-CO_2 test case PAG25. Only the fracturing period is shown and the 1-day pre-waterflooding period is not shown. The leadoff rate of water in this case before the fracturing process is around 1.1 mL/min as labeled in **Figure 11**(a). In the first injection cycle, 11.3 mL of PAA was injected at 1,000 psi, then CO_2 was injected at 2 mL/min until the pressure peaked (and began to decline, again indicating either breakthrough/leak-off or fracture initiation). The CO_2 injection continued then for 30 more seconds. Subsequent cycles followed, with an injection of PAA at constant pressure (1,000 psi) until the PAA injection rate is reduced to around 0 mL/min [this is shown in each cycle in the top plot of **Figure 11**(a) and (b)]. The bottom figure in **Figure 11**(a) shows that the CO_2-pressure peaks and this maximum steadily increases during cycles 1-15 as labeled in **Figure 11**(a). Then, this maximum plateaus and decreases. The detailed pressure behavior of PAA can be read from the zoomed-in cycle 3 for PAA and CO_2 injection, which is shown in **Figure 11**(b). At the beginning of each cycle, there is a negative injection rate of PAA since the pressure at the wellbore is high due to the high-pressure CO_2 that remains from the previous cycle. After a few seconds, the PAA injection rate becomes positive and is followed by a sharp reduction to 0 mL/min as shown in the top plot of **Figure 11**(b). The net injection volume of PAA is positive and is quantified in each cycle. We hypothesize that at the end of each PAA/CO_2 cycle, fresh PAA becomes in contact and reacts with CO_2. As a result, the CO_2-crosslinked polymer product reduced the relative permeability of PAA, and the injection rate of PAA was reduced to 0 mL/min. Since multiple processes are taking place over each cycle, including 1) PAA-CO_2 reaction, 2) saturation changes of PAA and CO_2, and 3) pore pressure changes, it is difficult to infer whether a fracture is generated and propagated from simply measuring the injection rates and pump pressures. The average conductivity of the post-test sample is only 0.13 μm^3, which indicates that for cyclic injection at these injection rates, PAA/CO_2 is not efficient in generating highly conductive fractures, unlike in the case of higher injection rates previously discussed in single-cycle PAG.

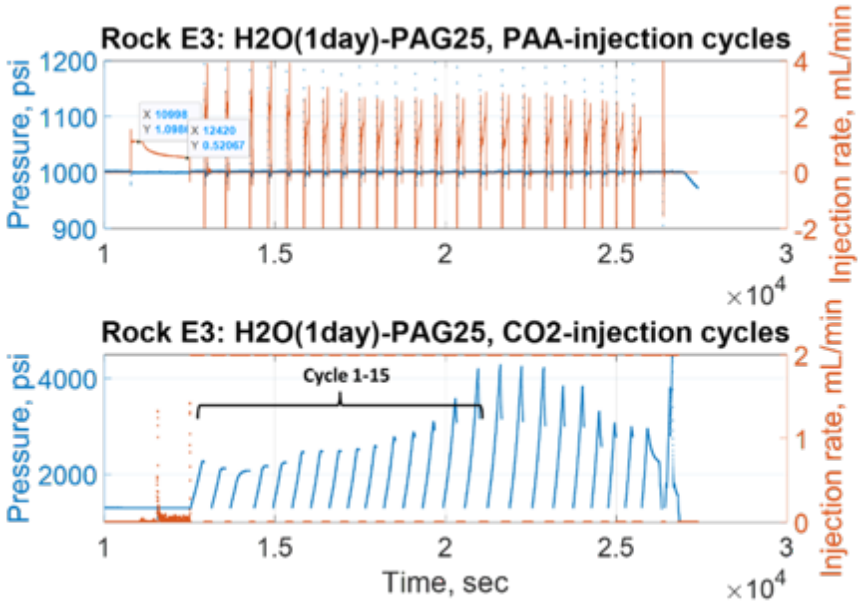

(a)

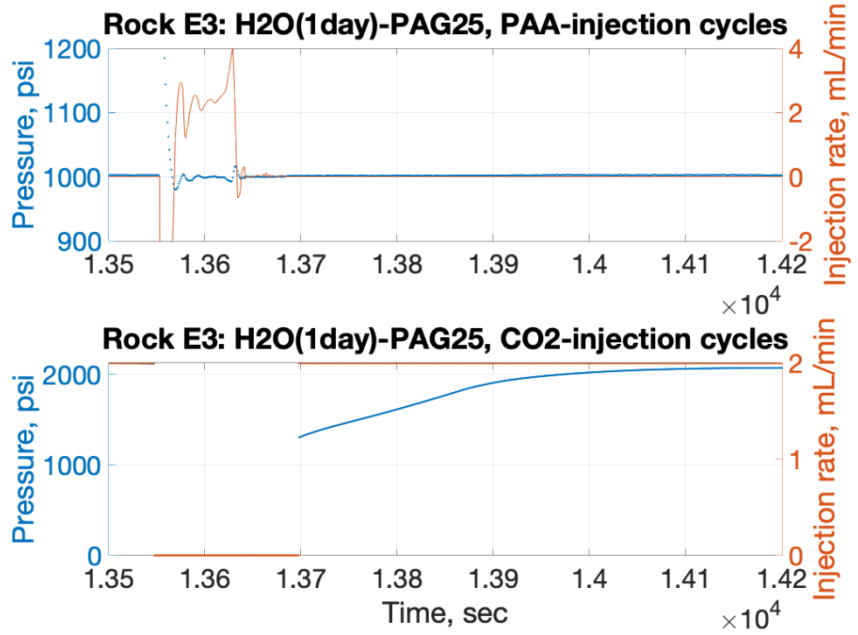

(b)

Figure 11 (a)25 cycles PAG fracturing with PAA-CO_2 in 1-day pre-waterflooded rock; (b) zoomed-in 3rd cycle for PAA and CO_2 injection

Multiple cycles of WAG and PAG were limited to low injection rates to avoid propagating the fracture too quickly due to the small size of the rock (3" from center to rock walls). However, these less-than-realistic injection rates attained fractures with very low conductivities independently of the fracturing fluid used (or the initial water saturation of the rock). Because of this, we opted for one WAG (or PAG) cycle at high (more realistic) injection rates. The results show that PAA/CO_2 outperforms water/CO_2 in terms of fracturing efficiency under dry and 1-day water-flooded rock conditions. We hypothesize that multiple injection cycles at low injection rates (2mL/min) may generate fractures with smoother surfaces and/or no fracture wall displacement. On the other hand, a single fracturing event at high injection rates (1-cycle WAG) may produce a rougher fracture surface and/or a small displacement needed for the fracture to self-prop. This is evidenced when comparing the test in Rock E3 with the test in Rock G3 where, under similar pre-water flooding initial conditions, one PAA/CO_2 cycle with CO_2 injected at 25 mL/min attains a fracture 2-3 orders of magnitude more conductive than when injecting PAA/CO_2 over multiple cycles at low injection rates (2 mL/min CO_2).

As a side note, the reader could ask why the fracturing experiments in hot dry rock were performed at 10 mL/min while the experiments on rock samples pre-flooded (1 day or 3-day) with water were performed at 25 mL/min. The reason lies in the test in rock E7 (test 14), which is the test using CO_2 as a sole fracturing fluid injected in 3-days water-saturated rock, we found that even at a high (20 mL/min) injection rate, the rock conductivity after fracturing was very low. Therefore, higher injection rates were adopted for these water-flooded rock samples.

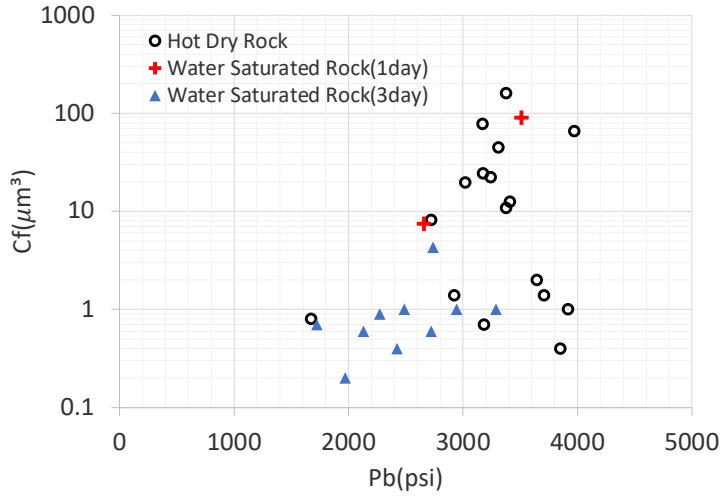

Figure 12: Results of conductivity Vs. breakdown pressure with different injection strategies in different water-saturated rocks

The fracturing results in the hot dry rock and 1-day or 3-day pre-waterflooded rock specimens are shown in **Figure 12**. The black circles are experimental results in hot dry rock. The red cross symbols are the data with 1-day pre-waterflooded rock. And the blue triangle data shows the data of fracturing in 3-days pre-waterflooded rock. Multicycle WAG and PAG data are not plotted in this figure since the fracture conductivity is low and there is no apparent fracture breakthrough to the rock surface after multiple cycles. From **Figure 12**, it is evident that for most of the tests in 3-days pre-waterflooded rock samples, the conductivity of the rock after fracturing is below 1 μm^3 except for one PAA/CO_2 test.

When performing fracturing experiments in 1-day pre-waterflooded rock, the conductivity after fracturing was as large as 90.1μm^3 only when PAA was used. Without the presence of PAA, the conductivity of the rock after fracturing using 25 mL/min CO_2 was an order of magnitude lower (7.5 μm^3). Since only one 1-day pre-waterflooded test was conducted (for each fluid), additional tests are required to better quantify potential data variability. Nevertheless, the low conductivity fractures obtained in all tests performed in 3-days pre-waterflooding rock as compared against the hot dry rock results, indicate that water saturation has a significant impact on fracturing efficiency independently of the fracturing fluid used. In hot dry rock or pre-waterflooded rock, the PAA/CO_2 system was demonstrated to outperform other fracturing fluid systems in terms of hydraulic conductivity enhancement. In 3-day pre-waterflooding rock, PAA/CO_2 still outperforms the other fracturing fluids in terms of permeability enhancement (about twice more conductive fractures) but the difference in fracture conductivity between PAA/CO_2 and the other fracturing fluids is less than in 1-day pre-waterflooded rock and hot dry rock.

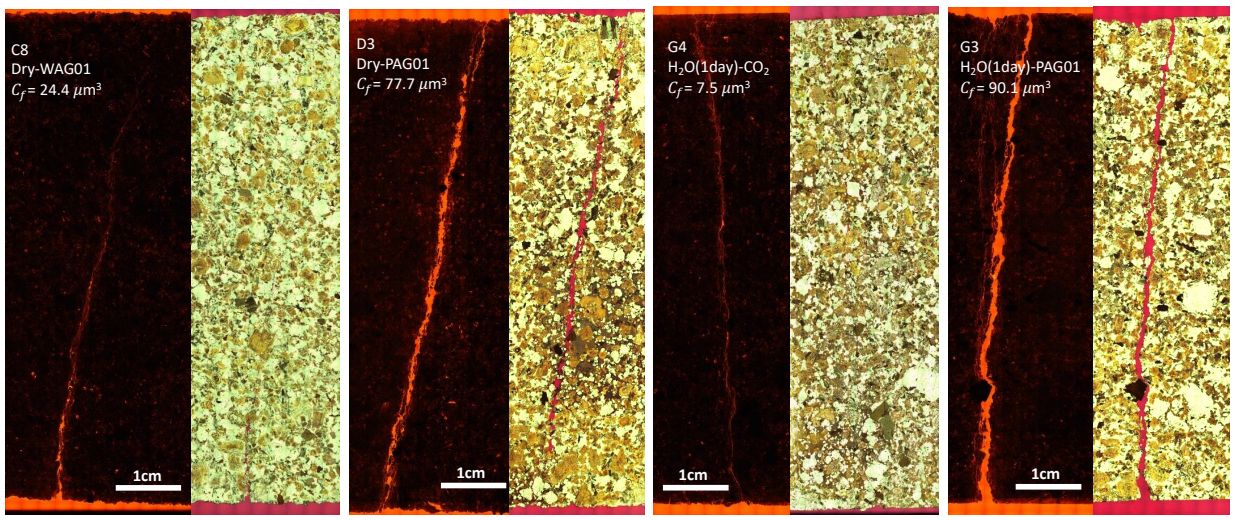

Figure 13 Fluorescence and non-fluorescence images of the thin sections with different injection strategies a) Dry-WAG01; b) Dry-PAG01; c) H_2O(1 day)-WAG01; d) H_2O(1 day)-PAG01

Figure 13 shows fracture networks attained by different fracturing fluids under two water saturation conditions. The results show that the fracture aperture is much larger for PAG injection(**Figure 13**(b) and (d)) than for WAG injection(**Figure 13**(a) and (c)) at either dry or 1-day water-saturated conditions. A clear complete fracture was generated from the injection wellbore (bottom in **Figure 13**) to the production part which is the rock surface (top in **Figure 13**) when using PAA. This indicates that the fracture is highly conductive and can propagate effectively using PAG as an injection strategy at the lab scale. There are no obvious differences in fracture path using PAA/CO_2 in dry rock(**Figure 13**(b)) or 1-day water-saturated rock (**Figure 13**(d)). Therefore, a moderate water saturation change will not change the effectiveness of the PAA/CO_2 fracturing process. If the water saturation is high (3 days water saturation), the effectiveness of PAA/CO_2 (and of any other fluid studied here) fracturing drops significantly with fracture conductivity no larger than 10 μm^3. It is important to mention, however, that PAA/CO_2 was the only fluid capable of generating a relatively higher conductive fracture (although parallel to the wellbore) in one of the tests.

The consistently large fracture apertures for PAA/CO_2 fracturing process can be explained by the formation of a viscous fluid/gel (Fernandez et al., 2019; Jian et al., 2021; Shao et al., 2015) generated during the PAA/CO_2 mixing and crosslinking reaction in the porous media. Our previous publication, where nonisothermal multiphase flow simulations using STOMP were performed(Jian et al., 2021), show that PAA/CO_2 likely create a larger volume of rock where the fluid pressure exceeds the minimum principal stress. This is attributed to the high leakoff rate of supercritical CO_2 combined with the low leakoff rate of cross-linked polymer. We then anticipate that the injected volume of CO_2 creates a large volume with high pressure fluid surrounding the fracture tip, while excess leakoff and pressure loss behind the fracture tip would be limited by the volume of cross-linked polymer. The larger pressurized volume surrounding the fracture tip is believed to contribute to a higher degree of fracture conductivity, complexity, and self-propping. Both, fracture complexity and self-propping characteristics are critical to the formation of multiple fluid flow paths that maintain hydraulic conductivity post-stimulation without the need of pumping expensive thermally-stable proppants.

Though the combo PAA/CO_2 generates the largest conductive fractures in 15-cm cubic (granitic) rock, it is important to note that field-scale is a completely different game and a pilot scale test using PAG (alternating PAA/CO_2) could be beneficial to validate the potential of this fracturing fluid technology for field deployment. From the results of this study, some of the benefits of PAA/CO_2 towards transitioning the technology to field deployment includes: (A) larger pressure drops and resulting fracture apertures than the other fluids even at significantly lower flow rates, which signifies that at the significantly higher (six orders of magnitude) flow rates that can be attained in field scale (2-10 m^3/min vs. 25 mL/min in our lab), PAG could generate very large fractures(Liu et al., n.d.; Perkins and Kern, 1961). (B) The in-situ increase in viscosity as a result of the crosslinking reaction between PAA and CO_2 is anticipated to

increase fracture width and height and favor fracture propagation away from the wellbore. (C) The anticipated larger fractures obtained by PAA/CO_2 will not only increase the probability of self-propping via shear offset but also aid to proppant transport and emplacement. For these reasons a pilot-scale test with this fracturing fluid technology is recommended.

4. CONCLUSIONS

Higher breakdown pressures are observed in this study when higher injection rates are used, particularly when fracturing with water or CO_2. Higher water saturation will lead to lower breakdown pressure when fracturing with water, CO_2, single-cycle WAG, and PAG.

The initial water saturation condition has a significant impact on the fracture conductivity post-stimulation. In hot dry rock or 1-day pre-waterflooded rock, the fracture conductivity is the highest when using PAA/CO_2 fracturing system. In the case of 3-days pre-waterflooded rock samples, the post-test conductivity is low independent of the fracturing fluid/method used. A moderate water saturation (1-day injection of water) or zero water saturation is beneficial for generating large fractures in the absence and presence of PAA. Cycling injections in the tests are less effective for generating large fractures. High water saturation (3 days injection of water) can lead to low conductive fracture regardless of the fracturing fluid is used.

A moderate water saturation (1-day injection of water) was found to be beneficial for decreasing the amount of CO_2 used for fracture initiation and propagation since the water saturation near the wellbore can significantly reduce the CO_2 relative permeability. However, at high-water saturation (3 days injection of water) it was observed a larger consumption of CO_2, particularly for WAG method, and this was described to be due to a two-phase displacement occurs along with the fracturing process. A large amount of CO_2 will be introduced to the rock during this process and more CO_2 will be required for pressurization and fracturing to compensate for the CO_2 required for displacement.

When it comes to permeability enhancement of granitic rock, single cycle PAA/CO_2 demonstrated to consistently generate the highest conductive fractures (up to two orders of magnitude respect to water) independently of injection rate in hot dry rock and 1-day water saturated rock. At high water saturation levels (3-day water flooded rock) all fluids struggle to generate high conductivity fractures. This is, to be the best of our knowledge, an important discovery, and it is hypothesized to be associated to the lowed breakdown pressure observed in all stimulation experiments with CO_2 on 3-day water pre-flooded rock as compared to dry rock or 1-day water pre-flooded rock. The low breakdown pressure could be the result of residual pore pressure from the water saturation portion of the experiment and/or the result of water weakening of the rock as reported elsewhere. Lower breakdown pressures result in small fracture apertures during fracture propagation and, since the fracture propagation pressure is proportional to the fracture toughness (which is lower under saturated conditions than under dry conditions), then the potential residual fracture aperture is reduced when the aperture during propagation is reduced.

Nevertheless, single cycle PAA/CO_2 was the only fluid that attained a relatively higher conductive fracture under these conditions. Future work will look into the why of this behavior and how to optimize SimuFrac (PAA/CO_2) performance under highly water saturated conditions.

ACKNOWLEDGEMENTS

Funding is provided by the Department of Energy's Geothermal Technology Office. PNNL is operated by Battelle for the U.S. DOE under Contract DE-AC06-76RLO 1830.

REFERENCES

Bradford, J., Ohren, M., Osborn, W.L., McLennan, J., Moore, J., Podgorney, R., 2014. Thermal stimulation and injectivity testing at Raft River, ID EGS site, in: Proceedings of 39th Workshop on Geothermal Reservoir Engineering, Stanford, CA, USA.

Chabora, E., Zemach, E., Spielman, P., Drakos, P., Hickman, S., Lutz, S., Boyle, K., Falconer, A., Robertson-Tait, A., Davatzes, N.C., 2012. Hydraulic stimulation of well 27-15, Desert Peak geothermal field, Nevada, USA, in: Proceedings of Thirty-Seventh Workshop on Geothermal Reservoir Engineering, Stanford University, Stanford.

Fernandez, C.A., Gupta, V., Dai, G.L., Kuprat, A.P., Bonneville, A., Appriou, D., Horner, J.A., Martin, P.F., Burghardt, J.A., 2019. Insights into a Greener Stimuli-Responsive Fracturing Fluid for Geothermal Energy Recovery. ACS Sustainable Chem. Eng. 7, 19660–19668. https://doi.org/10.1021/acssuschemeng.9b04802

Hu, L., Ghassemi, A., Pritchett, J., Garg, S., 2020. Characterization of laboratory-scale hydraulic fracturing for EGS. Geothermics 83, 101706. https://doi.org/10.1016/j.geothermics.2019.07.004

Isaka, B.L.A., Ranjith, P.G., Rathnaweera, T.D., Wanniarachchi, W.A.M., Kumari, W.G.P., Haque, A., 2019. Testing the frackability of granite using supercritical carbon dioxide: Insights into geothermal energy systems. Journal of CO2 Utilization 34, 180–197. https://doi.org/10.1016/j.jcou.2019.06.009

Jian, G., Sarathi, R.S., Burghardt, J., Bonneville, A., Gupta, V., Fernandez, C.A., Garrison, G., 2021. Evaluation of a Greener Fracturing Fluid for Geothermal Energy Recovery: An Experimental and Simulation Study. Geothermics 97, 102266. https://doi.org/10.1016/j.geothermics.2021.102266

Jung, H.B., Carroll, K.C., Kabilan, S., Heldebrant, D.J., Hoyt, D., Zhong, L., Varga, T., Stephens, S., Adams, L., Bonneville, A., Kuprat, A., Fernandez, C.A., 2015. Stimuli-responsive/rheoreversible hydraulic fracturing fluids as a greener alternative to support geothermal and fossil energy production. Green Chem. 17, 2799–2812. https://doi.org/10.1039/C4GC01917B

Khan, J.A., Padmanabhan, E., Haq, I.U., Yekeen, N., Mumtaz, M., Prajapati, S., 2022. Experimental Assessment of Fracture Initiation and Wettability in Low and High Brittle Shales by CO2 Foam Fracturing Fluids. Energy Fuels 36, 8288–8300. https://doi.org/10.1021/acs.energyfuels.2c00310

Lecampion, B., Desroches, J., Jeffrey, R.G., Bunger, A.P., 2017. Experiments versus theory for the initiation and propagation of radial hydraulic fractures in low-permeability materials. Journal of Geophysical Research: Solid Earth 122, 1239–1263. https://doi.org/10.1002/2016JB013183

Li, S., Zhang, S., Ma, X., Zou, Y., Li, N., Chen, M., Cao, T., Bo, Z., 2019. Hydraulic Fractures Induced by Water-/Carbon Dioxide-Based Fluids in Tight Sandstones. Rock Mech Rock Eng 52, 3323–3340. https://doi.org/10.1007/s00603-019-01777-w

Liu, X., Qu, Z., Guo, T., Wang, D., Tian, Q., Lv, W., n.d. A new chart of hydraulic fracture height prediction based on fluid–solid coupling equations and rock fracture mechanics. Royal Society Open Science 5, 180600. https://doi.org/10.1098/rsos.180600

Lund, J.W., 2011. Direct utilization of geothermal energy 2010 worldwide review. Geothermics 40, 159–180.

Lund, J.W., Boyd, T.L., 2016. Direct utilization of geothermal energy 2015 worldwide review. Geothermics 60, 66–93. https://doi.org/10.1016/j.geothermics.2015.11.004

Lund, J.W., Freeston, D.H., 2001. World-wide direct uses of geothermal energy 2000. Geothermics 30, 29–68. https://doi.org/10.1016/S0375-6505(00)00044-4

Lund, J.W., Freeston, D.H., Boyd, T.L., 2005. Direct application of geothermal energy: 2005 Worldwide review. Geothermics 34, 691–727. https://doi.org/10.1016/j.geothermics.2005.09.003

Perkins, T.K., Kern, L.R., 1961. Widths of Hydraulic Fractures. Journal of Petroleum Technology 13, 937–949. https://doi.org/10.2118/89-PA

Ranjith, P.G., Zhang, C.P., Zhang, Z.Y., 2019. Experimental study of fracturing behaviour in ultralow permeability formations: A comparison between CO2 and water fracturing. Engineering Fracture Mechanics 217, 106541. https://doi.org/10.1016/j.engfracmech.2019.106541

Shao, H., Kabilan, S., Stephens, S., Suresh, N., Beck, A.N., Varga, T., Martin, P.F., Kuprat, A., Jung, H.B., Um, W., Bonneville, A., Heldebrant, D.J., Carroll, K.C., Moore, J., Fernandez, C.A., 2015. Environmentally friendly, rheoreversible, hydraulic-fracturing fluids for enhanced geothermal systems. Geothermics 58, 22–31. https://doi.org/10.1016/j.geothermics.2015.07.010

Song, X., Guo, Y., Zhang, J., Sun, N., Shen, G., Chang, X., Yu, W., Tang, Z., Chen, W., Wei, W., Wang, L., Zhou, Jun, Li, Xiao, Li, Xiaofeng, Zhou, Jinhui, Xue, Z., 2019. Fracturing with Carbon Dioxide: From Microscopic Mechanism to Reservoir Application. Joule 3, 1913–1926. https://doi.org/10.1016/j.joule.2019.05.004

Thakore, V., Ren, F., Voytek, J., Wang, H., Wang, J.-A.J., Polsky, Y., 2021. High Temperature Stability of Aqueous Foams for Potential Application in Enhanced Geothermal System (EGS). Oak Ridge National Lab. (ORNL), Oak Ridge, TN (United States).

Withjack, E.M., Durham, J.R., 2001. Characterization and saturation determination of reservoir metagraywacke from The Geysers corehole SB-15-D (USA), using Nuclear Magnetic Resonance Spectrometry and X-ray Computed Tomography. Geothermics 30, 255–268. https://doi.org/10.1016/S0375-6505(00)00054-7

Ye, Z., Janis, M., Ghassemi, A., 2017. Injection-Driven Shear Slip and the Coupled Permeability Evolution of Granite Fractures for EGS Stimulation. Presented at the 51st U.S. Rock Mechanics/Geomechanics Symposium, OnePetro.

Zhang, C.P., Cheng, P., Ranjith, P.G., Lu, Y.Y., Zhou, J.P., 2020. A comparative study of fracture surface roughness and flow characteristics between CO2 and water fracturing. Journal of Natural Gas Science and Engineering 76, 103188. https://doi.org/10.1016/j.jngse.2020.103188

Zhuang, L., Kim, K.Y., Diaz, M., Yeom, S., 2020a. Evaluation of water saturation effect on mechanical properties and hydraulic fracturing behavior of granite. International Journal of Rock Mechanics and Mining Sciences 130, 104321. https://doi.org/10.1016/j.ijrmms.2020.104321

Zhuang, L., Kim, K.Y., Diaz, M., Yeom, S., 2020b. Evaluation of water saturation effect on mechanical properties and hydraulic fracturing behavior of granite. International Journal of Rock Mechanics and Mining Sciences 130, 104321. https://doi.org/10.1016/j.ijrmms.2020.104321

Project Take-Home Message

1. High-temperature stimulation experiments in granite using a ½-ft scale true triaxial system showed larger pressure drops and resulting larger fracture apertures for StimuFrac as comnpared to water-based and waterless fluids
2. This means that at the much higher (six orders of magnitude) flow rates in field scale (5 m^3/min vs. 25 cm^3/min in our lab), polymer-alternating-CO_2 **(PAG) could create large fractures and further away from wellbore**.
3. The **in-situ (and reversible) increase in viscosity** as a result of the PAA-CO_2 crosslinking reaction is anticipated to increase fracture width and height and **favor fracture propagation away from the wellbore** (see STOMP simulation at right).
4. The anticipated larger fractures (C*f* 100X higher than water) obtained by PAA/CO_2 will not only increase the probability of **self-propping via shear offset** but **also aid to proppant transport** and emplacement.
5. **Water saturation plays an important role in fracturing performance**: higher water saturation results in lower fracturing efficiency independently of the fracturing fluid used.
6. **PAA/CO_2 is the only fluid that generates a conductive fracture in highly (but not fully) water-saturated rock**
7. To PNNL's knowledge **there is no polyaxial loading frame** larger than a few centimeters that can do hydraulic fracturing test while maintaining the rock sample fully saturated with water at 200 C.
8. PNNL proposed a (less studied) different StimuFrac formulation to perform hydraulic fracturing tests at temperatures below the boiling point of water, i.e., 90C. However, GTO established that these alternative StimuFrac formulations show too low viscosity values to make them viable proxies for the use of PAA 17,000D (high-temperature formulation) in actual field stimulations at EGS conditions.
9. For all the above reasons, **a field demonstration with StimuFrac is recommended**.

Pacific Northwest National Laboratory

902 Battelle Boulevard
P.O. Box 999
Richland, WA 99354

1-888-375-PNNL (7665)

www.pnnl.gov